Fall 12-19-2021

Geochemical and sensor-based monitoring of fault-associated carbonic springs in Grand Canyon and northern New Mexico: identifying Hydrologic Pathways and establishing baselines

Chris McGibbon
University of New Mexico

Christopher James McGibbon

Candidate

Earth and Planetary Science

Department

This thesis is approved, and it is acceptable in quality and form for publication:
Approved by the Thesis Committee:

Dr. Laura J. Crossey, chairperson

Dr. Karl E. Karlstrom

Dr. Brandon Schmandt

Dr. Mark Person

Combining geochemistry and time series hydrology to examine fault controlled spring systems

By

CHRISTOPHER J. McGIBBON

B.S Earth Science; University of Plymouth, UK, 2004

M.S. Earth and planetary Science, University of New Mexico, 2015

DISSERTATION

Submitted in Partial Fulfillment of the
Requirements for the Degree of

Doctor of Philosophy in
Earth and Planetary Sciences

The University of New Mexico

Albuquerque, New Mexico

May 2022

Acknowledgments

I wish to thank my committee for their time and guidance over the last few years, their input has been invaluable for the success of these papers, and this dissertation. I would also like to thank Mehdi Ali for his patience and understanding whilst working in the Analytical Chemistry Lab and Viorel Atudorei and Laura Berkemper for stable isotope analyses at the CSI. I would like to thank Dr. Karl Karlstrom for his perpetual editing and input, and my advisor Dr. Laura Crossey for her guidance, support, and motivation during my time at UNM. Without the both of you on my team, the dream of achieving a Ph.D. would not have become a reality. The EPS office staff have been a constant source of support, from guidance through bureaucracy, to help with equipment, software, and excellent sustenance during exam periods. My graduate student family, too many to name, have helped with field and lab work, discussions about data, and have been an ear to bend over a beer. Lastly, my family have been everything, the start, the reason, and then end. Without them, none of this would have been possible.

Combining geochemistry and time series hydrology to examine fault controlled spring systems

By

Christopher J. McGibbon

B.S Earth Science; University of Plymouth, UK, 2004
M.S. Earth and planetary Science, University of New Mexico, 2015

Ph. D, Earth and planetary Science, University of New Mexico, 2022

Abstract

This dissertation examines the interaction of spring systems and faulting. When springs discharge within a fault zone the interaction is often complex, and multiple methods are required to understand the flow, mixing and evolution of groundwater. In karst aquifer systems fracture networks can range from sub-millimeter to meters and only adds to the complexities involved in examining spring hydrology. The Interest in springs and faulting is not only driven by science, but also has applied applications. Faulting and fluid flow are of interest to the oil and gas industry, and potential CO_2 sequestration. In the southwestern US, water quantity and quality are of more immediate concern. In these desert environments, springs are important locations that provide island habits for endemic species, are an important municipal resource, and often have local cultural significance. Decreases in spring and river discharge, and subsequent increases in salinity, threaten these habitats and create problems for water

resource managers. This work is an attempt at using multiple methods to examine fault controlled spring systems. Geochemistry of springs is examined using multiple natural tracers, which proved information about the source, evolution and mixing of different waters, and continuous monitoring sensors are used to examine the physical hydrology and investigate changes in spring parameters over time. This work is split into three chapters. Chapter 1 uses geochemistry to investigate the source and evolution of water for a series of springs that discharge along the Nacimiento fault near San Ysidro, NM. Chapter 2 uses continuous monitoring sensors to examine aquifer properties and fluid movement along the Nacimiento fault. Chapter 3 combines geochemistry and time series hydrology to investigate springs at Fence fault in Grand Canyon, examining sub-river circulation, and regional recharge and mixing.

Table of Contents

LIST OF FIGURES

CHAPTER 1

CHAPTER 2

CHAPTER 3

LIST OF TABLES

PREFACE

The following is a description of the contributions of each author:

Chris McGibbon (chapters 1 ,2 and 3): I conducted the majority of field and laboratory work. I was the principle contributor to each chapter on writing and data interpretation. I drafted all figures. Laura Crossey (Chapters 1, 2 and 3): Assisted with field word and sampling, data interpretation and gave feedback on figures and editing on the manuscript. Karl E. Karlstrom (chapters 1, 2 and 3): Assisted with field word and sampling, data interpretation and gave feedback on figures and editing on the manuscript. Tanner Grulke (chapter 1): Analyzed samples for strontium isotopes and concentration. Brandon Schmandt and Mark Person have provided feedback to chapters 2 and 3, and as the papers go under further review, may contribute ideas and manuscript editing, and may be added as paper co-authors.

CHAPTER 1: Carbonic springs as distal manifestations of geothermal systems, highlighting the importance of fault pathways and hydrochemical mixing: Example from the Jemez Mountains, New Mexico

By

Chris McGibbon[ab], Laura J. Crossey[a], Karl E. Karlstrom[a], Tanner Grulke[a]

[a] Department of Earth and Planetary Sciences, University of New Mexico, Albuquerque, NM 87131, USA

[b] Corresponding author

ABSTRACT

We examine a series of carbonic warm and hot springs in northern New Mexico, USA: 1) Tierra Amarilla springs 2) Penasco Springs and 3) Soda Dam, Jemez, and Indian hot springs. Springs are compared to waters from the Valles Caldera geothermal system and to groundwater in nearby sedimentary aquifers. Multiple hydrochemical tracers are applied to quantitatively evaluate flow paths and mixing at varying distances from the caldera. We test three hypotheses for source and transport of waters to Tierra Amarilla and Penasco Springs: San Juan basin origin, meteoric flow from the Nacimiento Mountains, and/or influence from the Valles Caldera geothermal system. Geochemically, carbonic spring groups are distinct from meteoric and sedimentary aquifer waters. Based on isotopes of He and Sr, and concentrations of Cl, SO_4, Li and B we interpret these carbonic springs to be distal manifestations of fluid circulation along faults with a mixture of Valles Caldera geothermal waters, local meteoric and Paleozoic aquifer waters, with the potential for small contributions from the San Juan Basin aquifers. Semi-confined fault conduits, the Jemez fault and

Nacimiento fault systems provide connectivity and help explain geochemical similarities and mixing trends within carbonic spring systems, and between these systems and the distal Valles Caldera. In addition, Penasco Springs are interpreted to reflect a component of outflow from the geothermal system that crosses the Nacimiento Mountain basement block along NE-trending faults. Input of deeply sourced waters can degrade water quality by contributing significant salinity and trace metals to groundwater at distances of > 50 km from geothermal systems, with faults acting as conduits for subsurface fluid flow.

Introduction

In the face of climate change, water managers in the American Southwest face increasing pressure to accurately forecast water supply (Gutzler, 2007) and water quality (Crossey et al., 2012). Understanding the source, movement, and controls on water quality is multifaceted. Additionally, hydrologic flow models show the complexities that faulting brings to fluid migration pathways (Banerjee et al., 2011). Integrated studies using a multi-parameter approach are required to identify fault pathways and their influence on springs, surface water and groundwater (Caine et al., 1996; Herczeg and Edmunds, 2000). Numerous studies combining natural tracers have shown evidence of groundwater upwelling and associated fault fluid circulation and migration (Chiodini et al., 1999; Crossey et al., 2009; Gardner et al., 2011; Phillips et al., 2003; Williams et al., 2013). In particular, the presence of mantle volatiles in carbonic

springs (Newell et al., 2005; Crossey et al., 2009, 2011, 2016) provide direct evidence of a deep connection. Deeply sourced, or endogenic, fluids obtained from below regional freshwater aquifers contribute elevated salinity, trace metals, CO_2, $^{87}Sr/^{86}Sr$ and mantle-derived He (Newell et al., 2005; Williams et al., 2013), and can effect both local and distal groundwater as determined by fault connectivity, the nature of the flow paths, mixing, and spring discharge.

Regional studies show the importance of deep groundwater inputs on surface water quality. Across the western U.S., groundwater that carries mantle volatiles (as evidenced by helium isotope values) are highly saline and poor quality with elevated trace metals, such as arsenic (Newell et al, 2005). Numerous workers (Philips et al., 2003; Hogan et al., 2007; Kirk et al., 2009; Williams et al., 2013) established salinity contributions from upwelling groundwater degrade water quality in the Rio Grande while Crossey et al., (2009) and Karlstrom et al., (2013) used helium isotope ratios and CO_2 to identify endogenic inputs to geothermal springs in Arizona and Colorado. Mantle tomography of the U.S. (Schmandt and Humphreys, 2010) shows low relative P wave velocities in northern New Mexico and below the Valles Caldera. Low velocity zones are thought to contain small but significant fractions of partial melt and volatiles (Schmandt and Humphreys, 2010), and have been associated with neotectonic mantle degassing in southern Colorado (Karlstrom et al., 2013) and across the western U.S. (Crossey et al., 2016) based on correlation of high $^{3}He/^{4}He$ ratios with low P-wave velocities. CO_2 springs and travertine deposits represent near-surface manifestations of volatile transfer from the mantle to the near-surface hydrologic system in regions

associated with domains of low mantle velocity (Karlstrom et al., 2013). Chiodini et al., (1999), Crossey et al., (2009) and Karlstrom et al., (2013) have all used carbon isotope values to identify the sources of carbon and provide evidence for the relative proportions of different carbon sources in carbonic springs.

This study focuses on carbonic warm and hot springs (20-60 ºC) in northern New Mexico that are situated at the nexus of three physiographic provinces: the Rio Grande rift, southern Rocky Mountains, and Colorado Plateau. The study area provides a unique field laboratory where the interaction of multiple hydrologic flow paths can be studied. Three groups of artesian, CO_2-rich travertine-depositing springs are examined (Figure 1 and S1): 1) Tierra Amarilla (TA) anticline spring group near San Ysidro, 2) Penasco Springs group (PS) on the west side of the Nacimiento uplift, and 3) Soda Dam springs (SDS) and Jemez Springs (JS), and Indian hot springs (IS) within the Jemez Mountains. The Tierra Amarilla group, farthest from the Valles Caldera, consists of warm springs aligned N-S in the core of the Tierra Amarilla anticline (Hart 2001; Cron 2011). The Penasco Springs, west of the Nacimiento Mountains, are also warm carbonic springs, are along strike and farther north, but also aligned on the N-S trending Nacimiento fault. The third group of springs discharge in multiple locations in the San Diego Canyon, are aligned along the NE-striking Jemez fault zone (Kelley et al., 2007), and are considered part of the outflow of the Jemez hydrothermal system (Goff et al., 1981; Trainer, 1974).

Previous workers have concluded that groundwater discharging along the Nacimiento fault (TA and PS spring groups) is sourced from the San Juan Basin (Figure 1;

White 1985; Goff et al., 1986; Dam 1995). This hypothesis was inferred from groundwater flow directions based on potentiometric contour lines (Figure 1) of aquifers in the Cretaceous and Jurassic rocks of the south eastern San Juan Basin that indicate a general southeasterly flow direction (Frenzel and Lyford 1982; White 1985). A second hypothesis (Hart, 2001) is that springs along the Nacimiento fault are derived from flow down the southern Nacimiento mountains along the dip slope of the Agua Zarca sandstone aquifer (Figure 1). In this hypothesis, the water for carbonic springs is of dominantly meteoric origin and the carbonic character is gained through water-rock interaction along the flow path. A third hypothesis (Rennick et al., 1931) is that Nacimiento fault springs are sourced, at least in part, from the Valles Caldera hydrothermal system (Figures 1 and S2). In this hypothesis, the source of the CO_2 and the elevated temperature is the magmatically driven Valles Caldera hydrothermal system and its outflow plume that flows southwest from the caldera, down the San Diego Canyon.

The goal of this paper is to assess similarities and differences between spring groups to evaluate source regions, flow paths, hydrologic mixing and importance of faults, and thereby test the three hypotheses. The broader study area has seen extensive study, in particular the proximal Valles Caldera as a potential geothermal resource, however less attention has been paid to carbonic springs that are distal to the caldera. We use a suite of natural tracers evaluate temporal and spatial variations in chemical, gas and isotopic composition to examine fault conduits as a means of fluid transport and mixing with deeply sourced fluids in the groundwater systems. This

work has implications for water quality, land use, and geothermal potential of this and other regions.

Study Area

Regional Geology and Hydrostratigraphy

The geologic map and regional stratigraphy are shown in Figures S3 and S4, with major hydrostratigraphic units highlighted. The Laramide-age Tierra Amarilla anticline is an approximately 1.6-km-long north-trending fault-cored anticline. To the north, the Nacimiento uplift, is a north-south trending 80-km-long, 10-20-km-wide east-tilted uplifted basement-cored block bounded on the western side by the Nacimiento fault system (Woodward 1987). The southern end of this uplift terminates in a large south-plunging fold beneath unconformable Tertiary rocks (Slack, 1973). To the west, the San Juan Basin forms the southeastern margin of the Colorado Plateau; its eastern boundary is marked by the Nacimiento uplift. To the southeast, the Rio Grande rift comprises a series of north-trending grabens and half grabens, which extend from Colorado to the boarder of Mexico (Kelley, 1952; Chapin et al., 1994). The Jemez Volcanic field and Valles Caldera are located along the western rift fault. On a large scale, Valles Caldera was built on the western edge of the Rio Grande rift at its intersection with Jemez lineament (Heiken et al., 1990). The Jemez volcanic field consists of basaltic to rhyolitic rocks erupted from >13 to 0.13 Ma (Zimmerer et al., 2016).

The hydrostratigraphic units include the Madera Group limestone, a fractured carbonate aquifer where groundwater flow is concentrated along discrete fractures, fracture systems, or bedding planes. Above this the Abo and Yeso formations act as a confining layer (Crouch 1994) between the Madera and the San Andres-Glorietta aquifers. This aquifer may also be important east of Nacimiento fault and at depth in the San Juan basin. The Chinle shale is the confining unit below the Nacimiento fault springs and the Aqua Zarca is an important aquifer in the southern Nacimiento Mountains as it forms a southern dip slope to the anticlinal uplift. The Jurassic Entrada Sandstone forms an isolated aquifer in the San Juan Basin that is stratigraphically separated by aquitards of mudstone, shale, and siltstone, and by lateral discontinuities produced by north-south faults. Many of the aquifers exhibit elevated temperature, up to 25^{o}C.

Geothermal setting

The Valles Caldera contains a magmatic hydrothermal system with well-characterized geothermal fluids. Numerous workers have investigated the hydrothermal aspects of the Valles Caldera (Lambert et al., 1980; Goff at al., 1981, 1986, 1988, 2002; Hulen et al, 1986; Heiken et al., 1990; Shevenell et al., 1987; Vautaz et al., 1986,), but less attention has been given to the distal effects of the hydrothermal system, particularly connected to fault-related fluid circulation and mixing (Cron, 2011). Briefly, a hydrothermal outflow plume from the Valles Caldera has been suggested

(Dondanville 1971; Trainer 1974) with geochemical evidence from springs in this location, including Soda Dam and Jemez Springs, providing support for this idea (Goff et al., 1981). The depth of hydrothermal circulation in the outflow is believed to be in excess of 2000m, with temperatures reaching 330^{o}C and a plume extending down San Diego Canyon at least as far as Jemez Springs and potentially further (Goff et al., 1988; Trainer et al., 2000). In this model, as shown in Figure S2, meteoric water recharges the geothermal system, then rises by convection to depths of 600m or less. Fluid flows out of the caldera, towards the west and southwest, under the Jemez Plateau and along the Jemez fault zone, where it mixes or discharges as hot springs in the San Diego Canyon (Dondanville, 1979; Goff et al., 1985; Goff et al., 1988; Ingebritson et al., 2006; Trainer et al., 2000). Two distinct zones are identified within the Valles Caldera, the Sulfur Springs area and Redondo Creek Baca wells, which itself is considered to consist of two subsets of hydrothermal fluids based on temperature and geochemistry. Wells drilled in the Valles Caldera show the plume to occur in the Madera limestone, while outside of the Caldera, the plume is only found in limestone rocks which are exposed in eroded folds and fault blocks (Trainer et al., 2000). Small, local, low to moderate temperature geothermal reservoirs of low volume are also found along the Jemez fault zone (Goff et al.,1981).

The extent of influence of geothermal waters in the carbonic springs within San Diego Canyon has been debated (Goff et al 1988). An interesting conundrum about the Soda Dam springs group of hot springs and wells is that, if they are manifestations of the Valles Caldera geothermal outflow plume, there are not simple NE to SW trends in

temperature and fluid chemistry along the San Diego Canyon, as Jemez Springs is further down the canyon, but warmer and less saline than Soda Dam, such that mixing of multiple fluids is required. The distal extent of this geothermal outflow plume has been debated, with some workers suggesting the Tierra Amarilla and Penasco Spring groups are unrelated to geothermal outflow (Goff et al., 1981). This is partially semantic in terms of defining mixing proportions at the distal end of a geothermal outflow plume, but evaluation of such mixing is also of practical importance in terms of geothermal exploration (for example the recent $5M DOE drill hole on Jemez Pueblo; Kaufman, (2011)) and in terms of potential degradations to surface and groundwater quality (Crossey et al., 2013). Goff et al., (1981) concluded that, based on ion ratios and Cl variation diagrams, San Ysidro mineral waters (Tierra Amarilla Springs) are not derivatives of the Valles Caldera, but originate from a separate low temperature system, discharging along the Nacimiento fault, a conclusion that we evaluate and differ from in this paper.

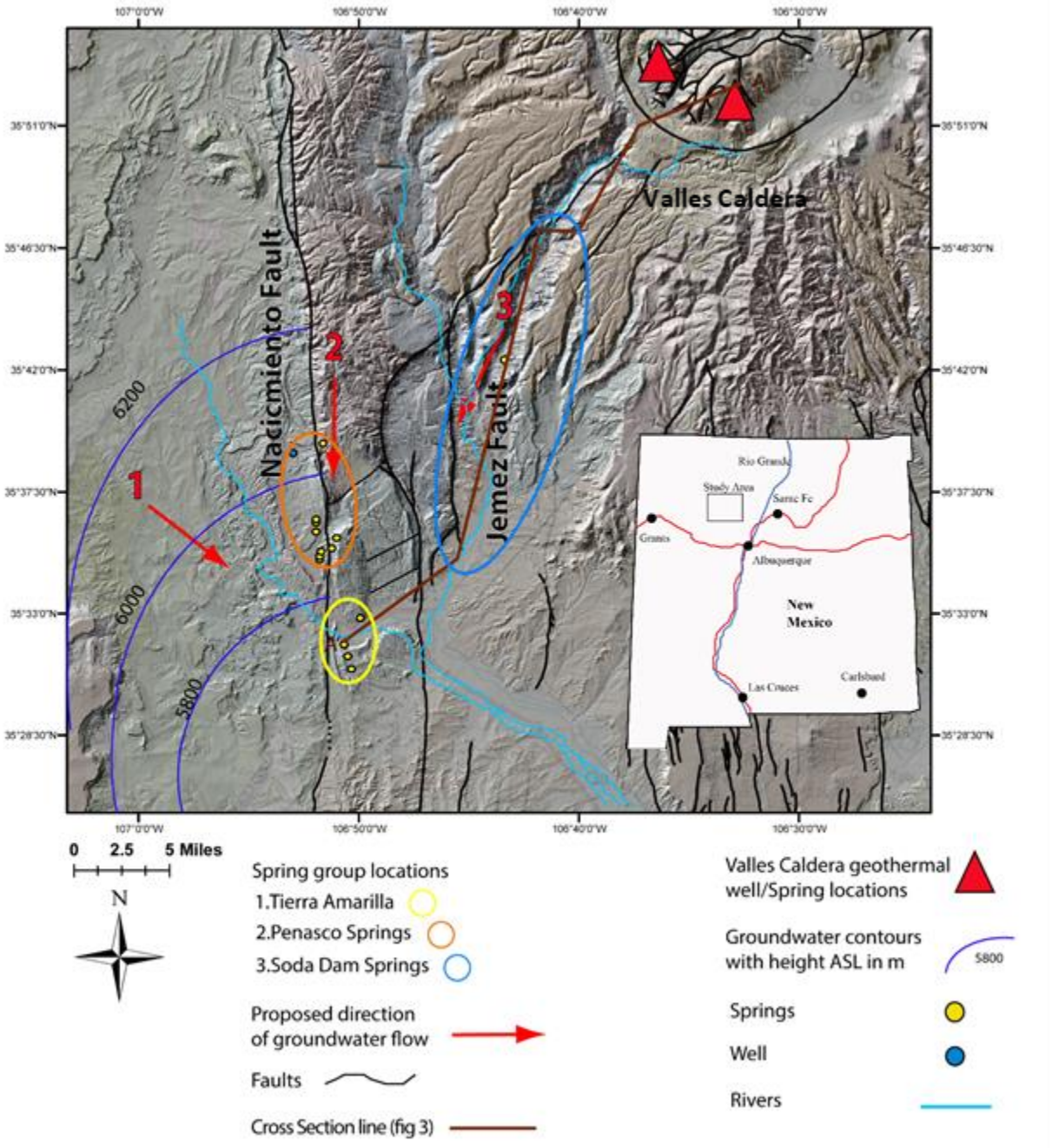

Figure 1. DEM (Earth Data Analysis Center, 1996) of study area with alternative models for groundwater flow directions to be tested: 1) San Juan basin flow path showing water table contours (Frenzel and Lyford 1982); 2) meteoric water from Nacimiento Mountains; 3) hydrothermal plume from Valles caldera. Main spring groups are shown by ovals. NE-SE line shows location of the cross section of Figure S2. Inset map shows study location in state.

Springs

The spring groups examined are near the northwestern portion of the Albuquerque Basin whose boundary with the Nacimiento uplift is a series of north- to northeast-trending faults (Woodward 1987). Details of the spring groups studied are depicted in Figure 1 (greater detail in Figure S1). Two of the spring groups occur along the Nacimiento fault zone both north and south of the Rio Salado: the northern Penasco Spring group and the southern Tierra Amarilla springs group. Within the Tierra Amarilla springs group, three springs are collinear and located along the fault that cores the Tierra Amarilla anticline, and one is off axis of the fault. The latter, North Highway spring, is also noted as being chemically distinct from the rest and with greater variation in chemistry (see below). This spring lies at the foot of the dip slope of Agua Zarca on the south-plunging fold of the southern Nacimiento uplift. Where the springs discharge, they form pools within travertine mounds and cisterns whose depth range from ~20 cm to up to ~8 m. The sizes of the spring orifices vary along their long axis from 10 cm to up to 10 m. Travertine occurs at all locations, and many inactive springs are represented by dry travertine mounds and vent orifices. Degassing of CO_2 is witnessed as bubbling at most springs. U-series age geochronology at the Tierra Amarilla anticline shows that the springs have been active intermittently from before 270 ka, at highest elevations, to modern actively forming mounds (Cron 2011). Little vegetation grows around the springs, and the pool surfaces are often found at depth below ground level, in collapsed travertine mounds, in some cases, up to 30m deep, indicating that the water elevations were higher in the past (Cron, 2011). All springs are at ~ 100 m higher

elevation than the proximal Rio Salado, indicating artisan characteristics. This elevation and the co-alignment along the fault indicate a confined or semi-confined aquifer sealed by the Triassic Chinle Formation and with fluid movement along the fault.

Methods

Water and gas sampling

We sampled a subset of the springs on multiple occasions over a one year period from November 2013 to October 2014. These raw data are synthesized with historical hydrochemical data (Supplementary material tables). Water sampling was carried out following procedures set out in USGS National Field Manual for the Collection of Water-Quality Data (2006). Water samples for cations and $^{87}Sr/^{86}Sr$ isotope ratios were collected in 60 mL High Density Polyethylene bottles (HDPE). Samples were filtered (0.45µm) and acidified using concentrated HNO_3. Samples for anion, alkalinity and $\delta^{18}O$ and δD isotope analysis were collected without headspace in 120 mL HDPE bottles. Direct gas sampling for concentration and isotope ratio (exsolved gases) for $\delta^{13}C\text{-}CO_2$ and He was carried out by submerging a plastic funnel over bubbling springs with gases then drawn into refrigeration-grade copper tubes that were flushed in-line before sealing with stainless steel clamps (Giggenbach and Goguel, 1988; Hilton et al., 2002).

Analytical methods

Water temperature, pH and specific conductance were measured using an Oakton waterproof pH/CON 300 multi-meter. Major ion chemistry was analyzed using inductively coupled plasma optical emission spectroscopy (cations) and ion chromatography (anions) using standard methods, comparable to US EPA 200.7 and EPA 300.0 respectively. Carbonate alkalinity was measured by titration using standard methods (American Public Health Association, 1995). These analyses were carried out at the Analytical Geochemistry Laboratory at the University of New Mexico (UNM). Stable isotope analysis of D and ^{18}O were carried out using cavity ring down spectroscopy (Picarro L1102-I) with methods comparable to Wassenar et al., (2012) at the Center for Stable Isotopes, UNM. $^{87}Sr/^{86}Sr$ ratios were determined on a Neptune MC-ICP-MS using methods comparable to Pin and Bassin (1992) at the Radiogenic Isotope Geochemistry Laboratory at UNM. Total CO_2 and He concentration and the isotopic ratio $^{3}He/^{4}He$ and $^{13}C/^{12}C$-CO_2 were analyzed at the Fluids and Volatiles Laboratory at Scripps Institution of Oceanography using a noble gas isotope ratio mass spectrometer and electrostatic analyzer. $^{3}He/^{4}He$ ratios (R) are normalized to the atmospheric value (R_A), and corrected for air-derived He (to R_c/R_A) using the correction factor $X = [\{(He/Ne)_{sample} / (He/Ne)_{air}\} \times (b_{Ne}/b_{He})]$, where b = Bunsen solubility coefficient (See Hilton (1996) for details of the correction protocol). Geochemical modeling for saturation indices was carried out using PhreeqC (Parkhurst 1995).

Results

Water chemistry

Sample locations, field parameters and water chemistry are listed in tables S1 and 2 and shown in Figure 2 (Figure S1) and mean values are in table 1. Tierra Amarilla springs pH ranges from 5.38 - 6.94, temperature from 16.7 - 27.7°C and conductivity from 7400 to 20000 µS. It should be noted that whilst the range of

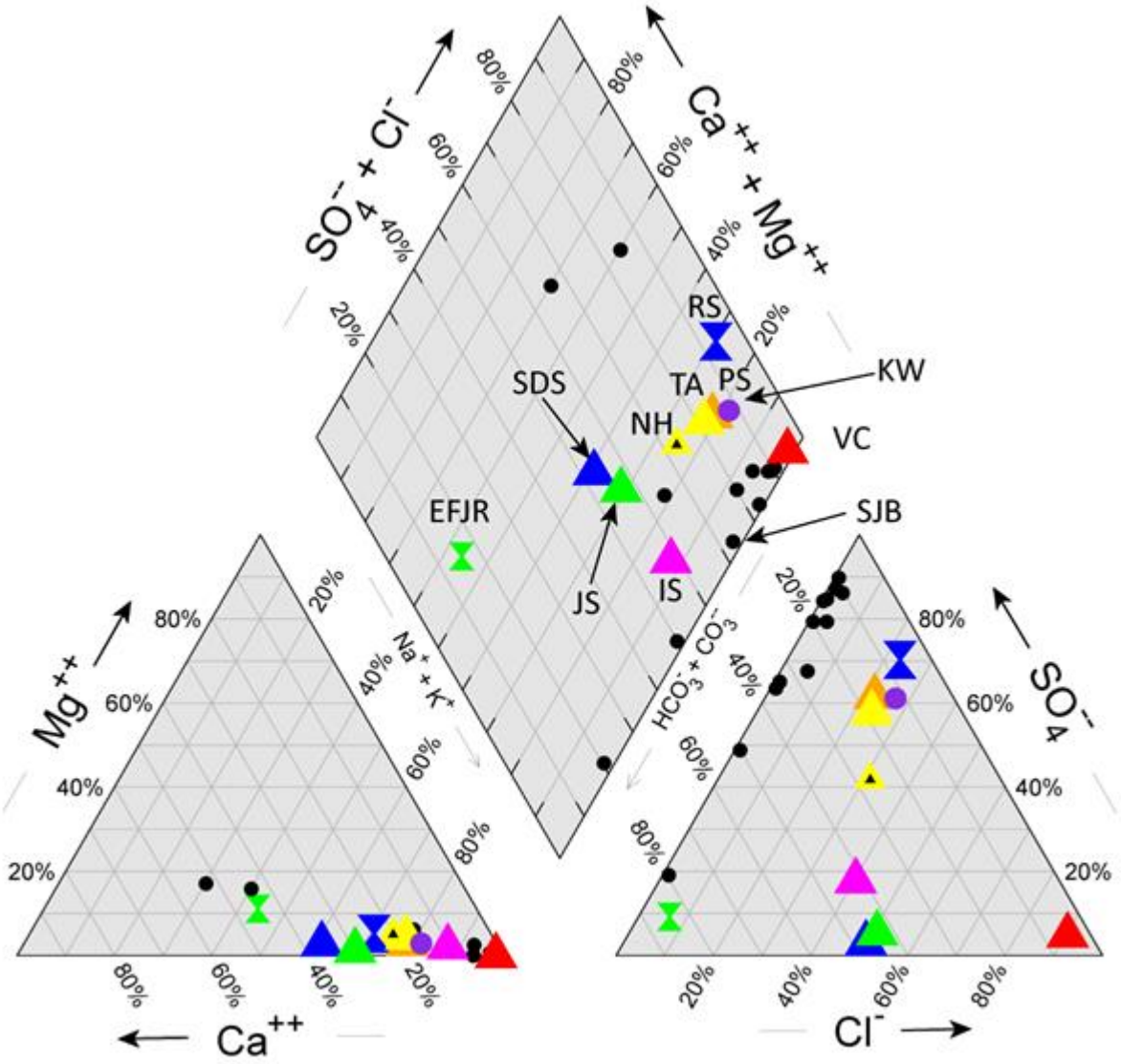

Figure 2. Piper diagram showing water samples in context of the broader study area. TA – Tierra Amarilla (large yellow triangle), NH – North Highway (smaller yellow triangle with black center), PS – Penasco Springs (orange triangle), KW – Kasemen Well (purple circle), SDS – Soda Dam spring (blue triangle), JS – Jemez Springs (green triangle), IS – Indian springs (pink triangle), VC – Valles Caldera (red triangle), RS – Rio Salado (blue X), EFJR – East Fork Jemez River (green X), SJB – San Juan Basin (black dots). Mean sample data are used for TA, PS, SDS, JS, IS and VC.

TA and PS springs samples cluster together alongside samples from SDS and JS. San Juan Basin waters plot in variable locations suggesting variable aquifer sources. Kasemen Well (KW) shows similar chemistry to TA/PS (individual spring Piper diagrams are in fig DR-2).

temperatures and conductivities between springs is quite large, variation within each spring is relatively small. Temperature variations track seasonal change, and at Twin Mound East are less than 1^{o}C over the course of the year, while conductivity variations within each spring are on the order of ~3000-4000 µS. Penasco Springs are similar to Tierra Amarilla springs; pH 6.02 - 6.63; temperature 19.1 - 34^{o}C and conductivity 5800 - 7420 µS. The carbonic springs are consistent through time in temperature, pH, and conductivity such that variations between springs and spring groups are interpreted to reflect different flow paths and mixing histories. Tierra Amarilla and Penasco Spring have overlapping major ion chemistry and are Na+K – SO_4/Cl dominated (Figure 2). At Tierra Amarilla, North Highway shows a different chemistry, having 15% less SO_4 relative to the rest of the springs. Soda Dam and Jemez Springs have higher Ca and HCO_3 in comparison to Tierra Amarilla and Penasco Springs, but are Na+K – SO_4+Cl dominated. Indian springs samples have relatively higher Na+K with SO_4 values that fall in between Tierra Amarilla/Penasco Springs and Soda Dam/Jemez Springs. Valles Caldera waters are Na+K – Cl dominated, typical of geothermal brines. San Juan Basin waters are dominantly Na+K – SO_4, but have a range of different chemistry, depending on the aquifer. The spring groups form distinct clusters (Figure S5 a-g and S6 a-g), different from surface and sedimentary aquifer waters, which indicate significant groundwater geochemical variability.

Conservative Tracers

Conservative tracers used to characterize geothermal systems include Li, B and Br, (table S4, mean values in table 2) and cross plots of these elements (vs Cl) are shown in Figures 3 a-c (and Figure S7 a-c). Previous studies (Goff et al., p241, 1981; Trainer et al, p88. 2000) used these conservative tracers (lower Li and Li/Na ratio) and Cl concentrations (Tierra Amarilla/Penasco Springs, 1500 - 3800mg/L, compared to Soda Dam springs/Jemez Springs, 200 - 1800mg/L) to suggest Tierra Amarilla/Penasco Springs are not sourced from the Valles Caldera. Our new data show a more overlapping range and although these plots highlight higher Cl concentration, they also show co-variation between elements, as well as mixing of different geothermal end-members. Cl is easily modified by dissolution of salts present in Paleozoic and Mesozoic strata (Trainer et al., 2000), so plots of Li vs B, Br vs Li and Br vs B were created, discussed below.

Stable Isotopes of D, ^{18}O and ^{13}C

Stable isotopes of D and ^{18}O from all spring locations as well as selected surface waters and aquifers in the study area are plotted in Figure 4 (table S3, individual springs plotted in Figure S8 a-g). Samples that plot close to the Global Meteoric Water Line (GMWL) include the East Fork Jemez River, representative of local meteoric water runoff, as well as regional aquifer waters from the San Juan basin. Samples from the San Juan Basin are lower than any observed spring values by up to δD 20‰

and $\delta^{18}O$ 3‰. Carbonic springs fall to the right of the GMWL and show a range of δD: -110.5‰ to -47.1‰ and $\delta^{18}O$ -14.5‰ to -3.65‰. Samples from Tierra Amarilla have the

Spring Name		Temp	pH	SpCond	Ca	Mg	Na	K	HCO_3	Cl	SO_4
Tierra Amarilla	Mean	21.4	6.0	12741	383	90	3010	111	2083	2395	2940
	Std. Dev.	2.7	0.1	2949	92	49	822	42	365	515	1198
Penasco Springs	Mean	24.9	6.3	13434	335	56	2705	84	1477	2288	2963
	Std. Dev.	4.1	0.2	1252	96	14	892	27	402	682	966
Valles Caldera	Mean	203.4	7.3	19707	21	0	1893	334	174	3169	43
	Std. Dev.	99.9	1.0	34363	27	1	353	127	86	561	12
Soda Dam Springs	Mean	43.4	6.4	6574	321	25	926	166	1390	1460	42
	Std. Dev.	6.4	0.3	572	44	8	97	23	225	118	9
Jemez Springs	Mean	65.9	6.6	3857	134	6	557	63	685	812	71
	Std. Dev.	10.6	0.3	763	20	2	135	13	93	210	135
Indian Springs	Mean	31.3	6.8	5086	75	15	1204	58	1285	1239	273
	Std. Dev.	13.0	0.4	3716	13	8	811	36	531	772	166
San Juan Basin	Mean	25.5	8.5	nr	54	15	251	2	296	59	437
	Std. Dev.	7.7	0.4	nr	53	15	251	1	65	98	375

Table 1. Mean and standard deviation for spring parameters and major ion chemistry.

Spring Name		Li	B	Br	Si	Sr
Tierra Amarilla	Mean	5.7	7.5	4.5	6.4	6.7
	Std. Dev.	2.3	2.7	2.3	2.3	4.6
Penasco Springs	Mean	8.2	10.5	4.2	11.4	8.8
	Std. Dev.	1.6	1.6	0.2	3.7	1.8
Valles Caldera	Mean	24.3	25.1	8.3	661.6	0.2
	Std. Dev.	4.7	6.0	1.9	57.6	0.1
Soda Dam Springs	Mean	13.2	12.8	5.5	42.5	1.6
	Std. Dev.	1.4	1.7	2.5	8.1	0.6
Jemez Springs	Mean	7.6	6.5	2.9	78.8	0.7
	Std. Dev.	1.9	1.5	0.7	20.8	0.3
Indian Springs	Mean	5.2	7.7	4.2	17.8	2.5
	Std. Dev.	1.5	0.0	0.0	0.0	0.1

Table 2. Mean and standard deviation for trace element chemistry. No data for San Juan Basin springs.

greatest range ~ δD 10‰ and $\delta^{18}O$ 4‰, while samples from Jemez Springs have similar δD, but lower $\delta^{18}O$ ~1-2‰.

The high and variable CO_2 content of these springs is used to understand their origin, mixing, and connection to geothermal fluids. The different carbon reservoirs considered as the source of CO_2 are: carbonates, organic (e.g. soil gas and carbon released from organic-rich sedimentary rocks), and endogenic (deep tectonic origin) carbon derived from fluids that have interacted and mixed with crust and mantle sources and circulation below the aquifer, including geothermal waters. These are represented by $\delta^{13}C$ values of ~ 0, ~ -28 and ~ -6 respectively (Sharp, 2007). Results are shown in table S6 and Figure 5a. $\delta^{13}C$ values range from $\delta^{13}C$ = -2.47 in the Valles Caldera to -8.71 at Tierra Amarilla, and show a decrease with distance from the Valles Caldera.

Strontium isotopes

$^{87}Sr/^{86}Sr$ can indicate if groundwater has been in contact with Precambrian basement granitic rocks where $^{87}Sr/^{86}Sr$ ranges from 0.7249 to 0.8160 (Banner, 1995; Brookins and Laughlin, 1983). In contrast, $^{87}Sr/^{86}Sr$ from marine carbonates have $^{87}Sr/^{86}Sr$ closer to 0.709 (Crossey et al., 2006). Mixing between these end-members has been quantified in past studies (Crossey et al., 2006).

The $^{87}Sr/^{86}Sr$ and Sr concentration data are reported in table S5. At Tierra Amarilla and Penasco Springs, $^{87}Sr/^{86}Sr$ range from 0.716932 to 0.720044 and Sr concentration from 5.910 to 19.3974 ppm. At Soda Dam and Jemez

Springs $^{87}Sr/^{86}Sr$ range from 0.709710 to 0.723217 with Sr concentration from 0.5689 to 1.634 ppm. In the Valles Caldera samples range from $^{87}Sr/^{86}Sr$ = 0.708069 to 0.708828 with Sr concentration from 0.0928 to 0.2598 ppm.

Gas chemistry

Using helium gas data from springs in the study area can help provide evidence of a deeply sourced connection, and further help delineate water source and amount of mixing. Mantle-derived fluids from hydrothermal activity at oceanic spreading centers characterize mid-oceanic ridge basalt (MORB) asthenosphere at 8 ± 1 R_A (Graham, 2002). Stable shield areas have much lower values of ~0.02 R_A (Andrews, 1985). $^3He/^4He$ ratio >0.1 R_A in non-air-like waters (>1.3% of MORB), are taken as evidence for the presence of mantle-derived fluids entrained by the hydrologic system (Ballentine et al., 2002). $^3He/^4He$ values measured from springs and wells in the study area are shown in Figure 5b, (table S6). Springs approach MORB values in the Valles caldera, reaching 6.3 R_A (79% MORB; Goff and Janik, 2002), 0.8-1.3 R_A at Soda Dam and Jemez Springs, 0.1-0.4 R_A at Indian springs and 0.2-0.3 R_A for Tierra Amarilla and Penasco Springs.

Figure 3a. Li vs Cl. Tierra Amarilla (yellow triangles), Penasco Springs (orange triangles), Kasemen Well (purple circles), Soda Dam spring (blue triangles), Jemez Springs (green triangles), Indian springs (pink triangle), Valles Caldera (red triangles). **3b**. B vs Cl shows a pattern similar to 3a. **3c**. Li vs B highlights
the close covariance for these two trace elements between Valles Caldera springs and those more distal from the caldera.

a

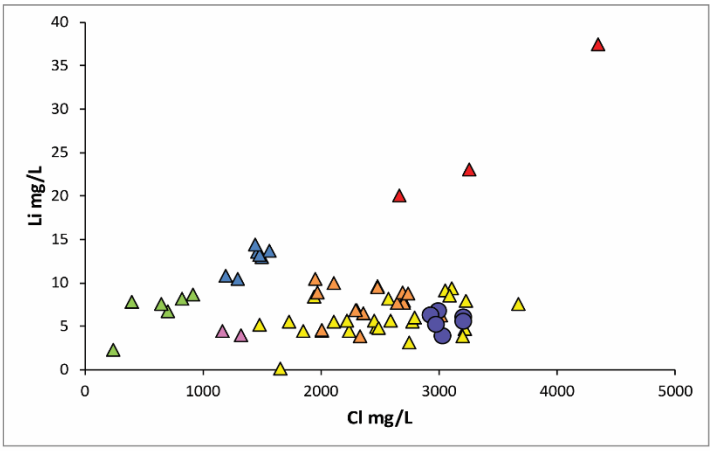

b

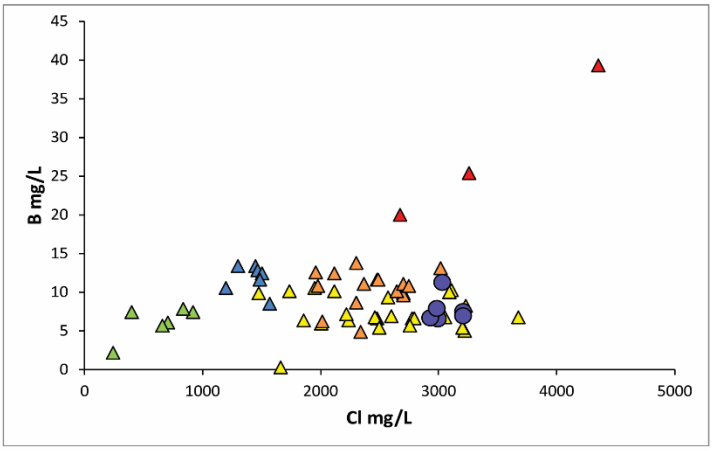

c

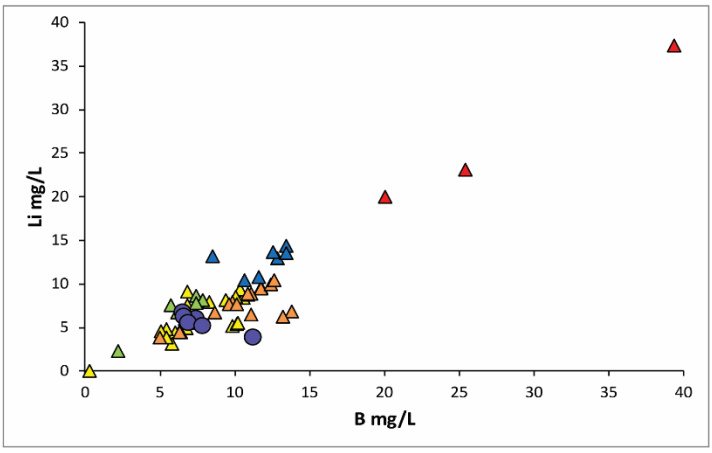

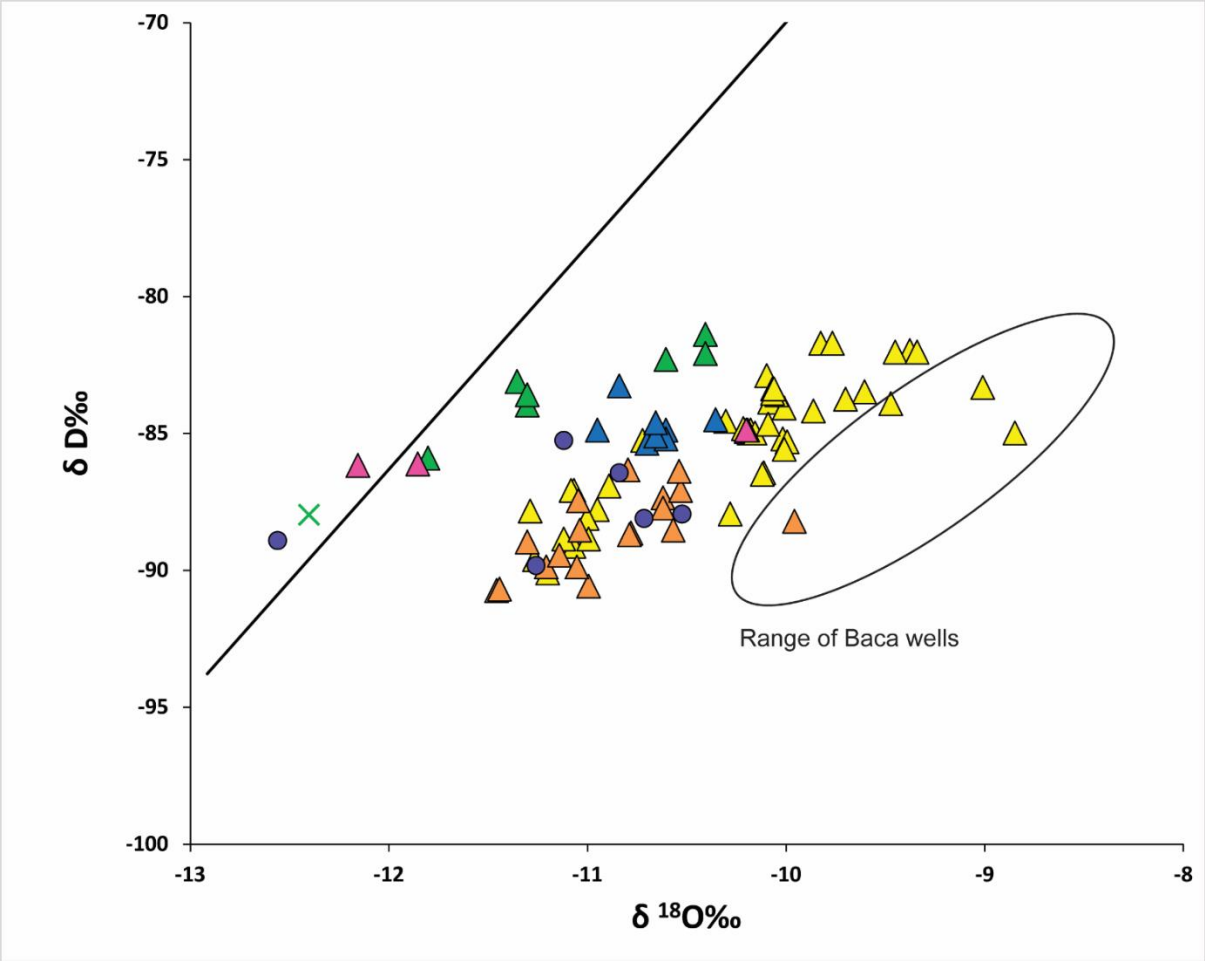

Figure 4. Stable isotopes of deuterium and oxygen. Tierra Amarilla (yellow triangles), Penasco Springs (orange triangles), Kasemen Well (purple circles), Soda Dam spring (blue triangles), Jemez Springs (green triangles), East Fork Jemez River (green X) and compositional range of Valles Caldera Baca wells (black oval; see Fig. DR4g for wider range of Valles Caldera geothermal waters). Samples from the Kasemen (purple circle) well show a range of values similar to Tierra Amarilla/Penasco springs (Individual spring samples are in figure DR-3).

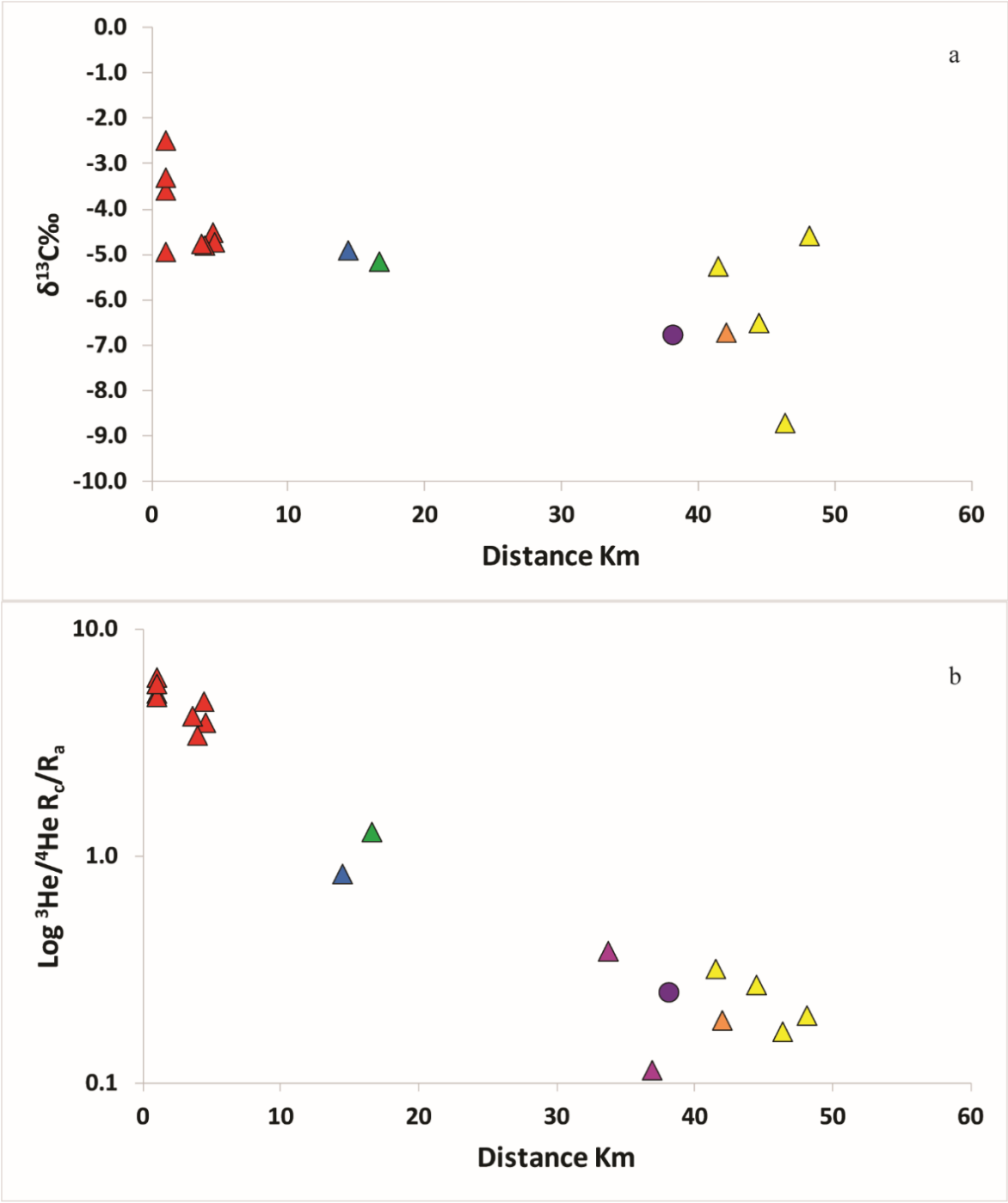

Figure 5a. $\delta^{13}C$ vs distance from the Valles Caldera. Tierra Amarilla (yellow triangles), Penasco Springs (orange triangles), Jemez Springs (green triangles), Soda Dam Springs (blue triangles), Valles Caldera (red triangles). Carbon isotope values decrease progressively with distance from the Valles Caldera due to mixing of endogenic and epigenic carbon sources. **5b**. Log $^{3}He/^{4}He$ vs distance from the Valles Caldera. With distance from the caldera, R_C/R_A values decrease. All values are above 0.1 R_C/R_A which suggests a significant mantle helium component.

Discussion

By identifying the chemical characteristics of end member waters, it is possible to establish potential water sources for springs at Tierra Amarilla/Penasco Springs. From here, we can assess the three hypotheses proposed, water origins from: 1) San Juan Basin aquifers, 2) young meteoric recharge from the Nacimiento Mountains, and 3) geothermal inputs.

Sedimentary aquifer end-member - San Juan Basin

Samples from groundwater wells of the San Juan Basin have varying characteristics depending on which aquifers are considered, Morrison, Dakota or Gallup Aquifers. Samples from the east side of the basin show primarily Na+K / SO_4 type waters, with temperatures ranging from 18 – 42 ^{o}C and pH ≈ 8.2. Stable isotopes of D and ^{18}O range from δD -87.0‰ to -110‰ and δ^{18}O-11.8‰ to -14.5‰. These aquifers are not present in the study area, but are considered representative of groundwater moving east, from the San Juan Basin towards the study area. These aquifer waters display a unique range of chemistry, which distinguishes them from both meteoric and geothermal/carbonic water (see Figures S6g and S8g). Gas samples from the north of the basin have He isotopes (0.08 – 0.17 R/Ra) and are dominated by methane (Zhou et al., 2005).

Meteoric water end-member – Nacimiento Mountain recharge

The Jemez River from above Soda Dam is considered a proxy for a local meteoric water end-member for mixing purposes. Temperature range track atmospheric

temperature, pH is ~ 7, salinity is low, major ion chemistry is dominated by Ca+Na / HCO_3, and from the Piper diagram (Piper, 1994) (EFJR - Figure 2) meteoric water is distinct from spring water samples. Stable isotopes of D and ^{18}O are δD -88.0‰ and $\delta^{18}O$ -12.40‰ that plot close to the GMWL. $^{87}Sr/^{86}Sr$ ratio is non-radiogenic ~0.709710 and Sr concentration is low ~0.09 ppm

Geothermal end-member - Valles Caldera

These waters are characterized by highest $^3He/^4He$ ratio, and ^{13}C with near-mantle signatures. Sulphur Springs and the Baca Wells in the Valles Caldera (T ~ 214, R_A/R_C ~ 6, $\delta^{13}C$ ~ -3.8‰) appears to represent the Valles Caldera end-member. They anchor linear trends in water chemistry as a sodium chloride dominated water (Figure 2), have the B, Br, Li signature of a geothermal water (Figures 3 a-c), and the most significant $\delta^{18}O$ enrichment of all samples (Figure 4). In this case, the near-MORB $^3He/^4He$ ratios from 3.39 to 6.16 R/Ra (Goff and Janik, 2002), and the near- MORB $CO_2/^3He$ ratio of 1 to 7 x 10^9 (Newell et al., 2005; compared to 2x 10^9 for MORB; Graham et al., 2002), and the $\delta^{13}C$ value of ~ -4‰ all suggest a magmatic origin for the CO_2. A magma chamber is suggested in the western portions of the Valles caldera (Trainer et al, 2000), and numerous recent eruptions over the last 1.6 Ma make it clear that high CO_2 is an ongoing expression of the Quaternary caldera magmatism and geothermal activity.

Soda Dam, Jemez Springs and Indian Springs are discussed here as they are considered to reflect an evolved water from the Valles Caldera (Goff et al., 1981),

mixing with meteoric water, and as such provide information about water which is both, chemically and geographically, closer to Tierra Amarilla and Penasco Springs. Jemez Springs show a similar chemistry to Soda Dam springs, but with greater variation and less salinity. These waters have very similar (overlapping) major and trace elements (Figures 2 and 3), stable isotopes of ^{18}O and D (Figure 4), helium isotopes, and $^{87}Sr/^{86}Sr$ (Figure 6). The enrichment in $\delta^{18}O$ and Cl, Li, B and Br, along with ^{3}He, are typical of the geothermal end-member, and together suggest a geothermal origin.

Tierra Amarilla and Penasco Springs

Having defined these possible end-members, the following sections describes mixing models for the spring groups. $^{3}He/^{4}He$ provides strong evidence of a mantle connection from samples within the Vallera Caldera. As distance increases from the caldera, $^{3}He/^{4}He$ values decrease (Figure 5b), but still suggest a mantle connection. As ^{3}He is derived from the mantle, a connection to the Valles Caldera would provide a source of ^{3}He, and subsequent mixing with meteoric water along the flow path and addition of ^{4}He from the crust, would cause dilution lowering the $^{3}He/^{4}He$ ratio. The geothermal input hypothesis is the only option which is able to provide a source for the observed ^{3}He and the high $^{3}He/^{4}He$ ratio. This conclusion does not preclude some mixing with other fluid end members examined. This discussion will now focus on explaining the water chemistry in terms of water sourced from the Valles Caldera, consider previous arguments against this hypothesis, and judge other potential end-members to explain the chemistry found at Tierra Amarilla and Penasco Springs. The Kasemen well is the furthest west of the samples taken (Figure 1 and S1), is

the only well sampled at Tierra Amarilla and Penasco Springs, and is known to penetrate the Madera aquifer. As such it has a symbol unique from other Penasco Springs samples for evaluation purposes.

Valles Caldera Hydrothermal Connection

The Valles Caldera hypothesis had been dismissed in the past (Goff et al., 1981), with the similarity in geochemistry being due to deep circulation of fluids and dissolution of evaporates along the Nacimiento fault in the Mesozoic to Paleozoic rocks, a geothermal system considered unique from the Valles Caldera. In particular, higher Na/Cl ratio, and lower B/Cl and Li/Na ratios in the springs at Tierra Amarilla and Penasco Springs in comparison to Jemez Springs were used to draw this conclusion. The new data with more springs sampled have trace element concentration ranges of Li, B and Ba comparable to Soda Dam and Jemez Spring (Figures 3a-c). The difference in ratios previously considered, is essentially a difference in major ion concentrations of Na and Cl (Figure S5a). These increased concentrations can be accounted for through water-rock interaction: dissolution of marine evaporites along the Nacimiento fault, a process suggested by multiple authors in the past (Goff et al., 1981; Trainer et al, 2000). Furthermore, co-variation in Li/B (Figure 3c) also provides evidence for a mixing continuum.

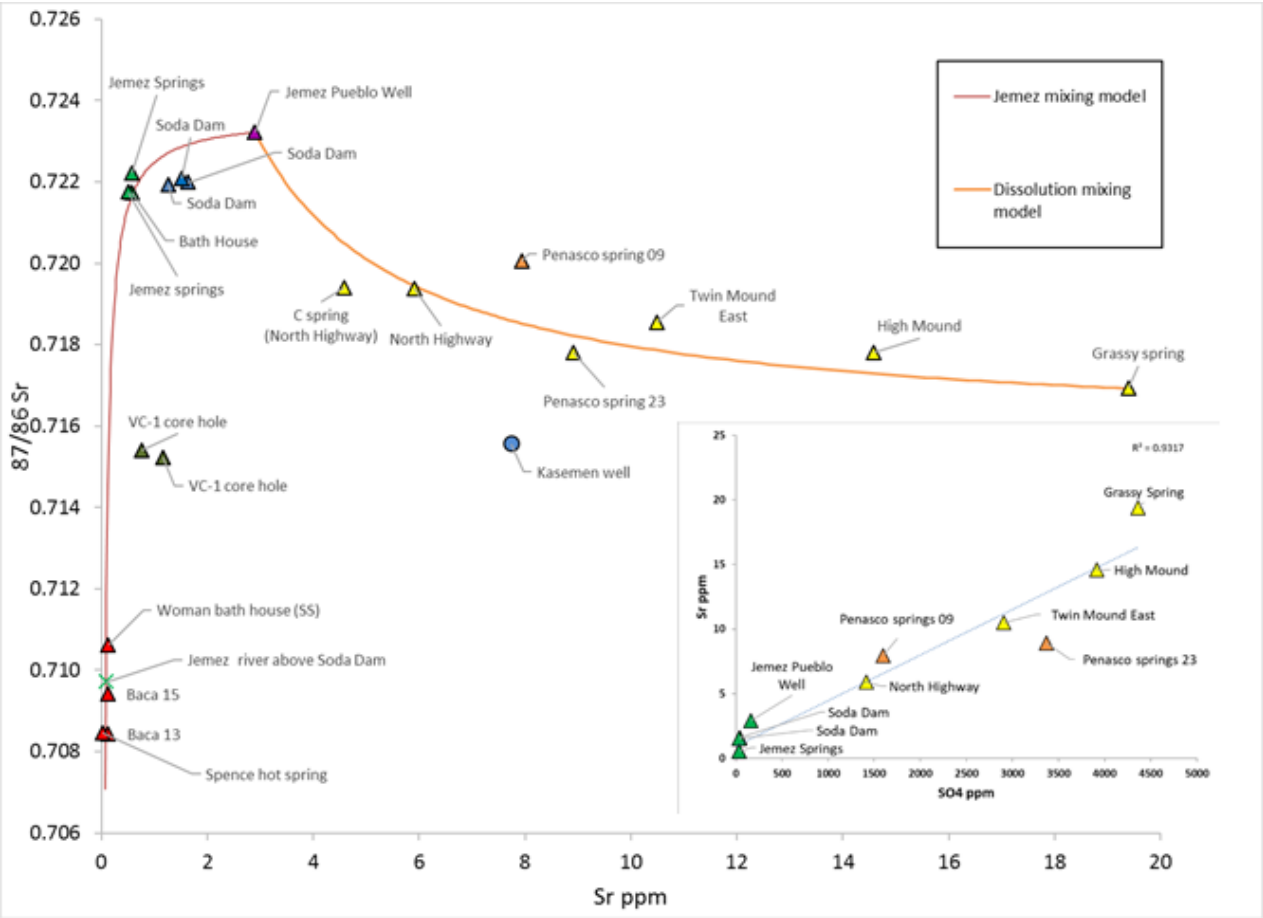

Figure 6. [Sr] in ppm vs $^{87}Sr/^{86}Sr$. Low concentration and non-radiogenic (low) $^{87}Sr/^{86}Sr$ are seen in samples from the Valles Caldera and Jemez River (meteoric water). Soda Dam and Jemez Springs, concentration increases and $^{87}Sr/^{86}Sr$ becomes more radiogenic (higher). Tierra Amarilla and Penasco springs have higher [Sr] and $^{87}Sr/^{86}Sr$ values decrease with increasing distance from the Valles Caldera reflecting mixing of geothermal (Valles) waters, first mixed with Jemez Springs waters (brown curve) then with more distal groundwater at Grassy Spring (orange curve). Binary mixing models (brown and orange curves) are described in text. Note that Grassy Spring is the southwestern most of the Tierra Amarilla springs (and furthest from the Valles Caldera) and is ~50 km SW of the Valles Caldera (see Fig. DR-1 for detailed location of Tierra Amarilla springs). Inset - SO_4 vs Sr (ppm). Samples show increasing Sr concentration with increasing SO_4 concentration reflecting mixing of geothermal waters with increased volume of waters influenced by water-rock interaction with Yeso Formation salts.

The majority of samples sit close to the 1:1 line, suggesting comparable processes occur. Comparing Li with distance from the Valles Caldera (Figure 7) shows a decrease in Li with increase in distance. This is attributed to mixing with meteoric water along the flow path, diluting Li concentrations, a phenomenon witnessed in multiple tracers, discussed below. Figure 3c suggests Tierra Amarilla and Penasco Springs plot along the mixing curve of geothermal conservative tracers that connects Valles Caldera springs/wells as one end-member, with Soda Dam and Jemez Springs as intermediate points, with meteoric and potentially sedimentary aquifer units as the other end-members. Figures 3 a-b show that fluid mixing and water rock interaction in the areas distal to the caldera are needed to explain non-linear relationships.

The isotopic enrichment of ^{18}O of water at Tierra Amarilla and Penasco Springs was suggested to follow a different trend to the geothermal waters sourced from the Valles Caldera (Goff et al., 1981). While the sample range appears to have an offset slope, as with the trace elements, the newly sampled data have an overlapping range, clearly different from the distinct spring clusters reported previously (Goff et al., 1981; Trainer et al., 2000) Similarities in stable isotope data of deuterium and oxygen (Figure 4) suggest a connection to Soda Dam and Jemez Springs if not the Valles Caldera, and potentially, the smaller geothermal reservoirs along the Jemez Fault, proposed by Goff et al., (1981), could be a source of mixing water for the study area, and be considered as being represented by water at Soda Dam springs or Jemez

Springs. This is a somewhat semantic argument as Soda Dam and Jemez Springs are considered to be sourced from the Valles Caldera.

Samples from all spring groups fall away and to the right of the GMWL. Spring groups' samples are considered to be formed through mixing between a geothermally evolved end member represented, by the Baca wells and meteoric waters, similar to the East Fork Jemez River. The overall array (all triangles) has a lower slope than evaporation and hence is interpreted to reflect variable water-rock interaction characteristic of geothermal fluids.

The hydrothermal outflow plume from the Valles Caldera provides an end-member source for mixing of water at Tierra Amarilla and Penasco Springs, utilizing the fault network which connects the two areas. This is highlighted through the application of strontium isotopes, and will be evidenced by radiogenic $^{87}Sr/^{86}Sr$ values and increased strontium concentration ([Sr]). Strontium isotope ratios show an initial increase and then decrease with distance from the Valles Caldera, while strontium concentrations display a continuous increase. Samples form distinct groups based on spatial variation (Figure 6). The Jemez River sample from above Soda Dam (local meteoric water) and the Valles Caldera have low [Sr], < 1ppm, and non-radiogenic $^{87}Sr/^{86}Sr$ values < 0.710. Meteoric water is low in all dissolved solids and the $^{87}Sr/^{86}Sr$ values for the Valles Caldera are due to the host rocks, Bandelier Tuff, andesite and rhyolite (Vuataz et al., 1988).

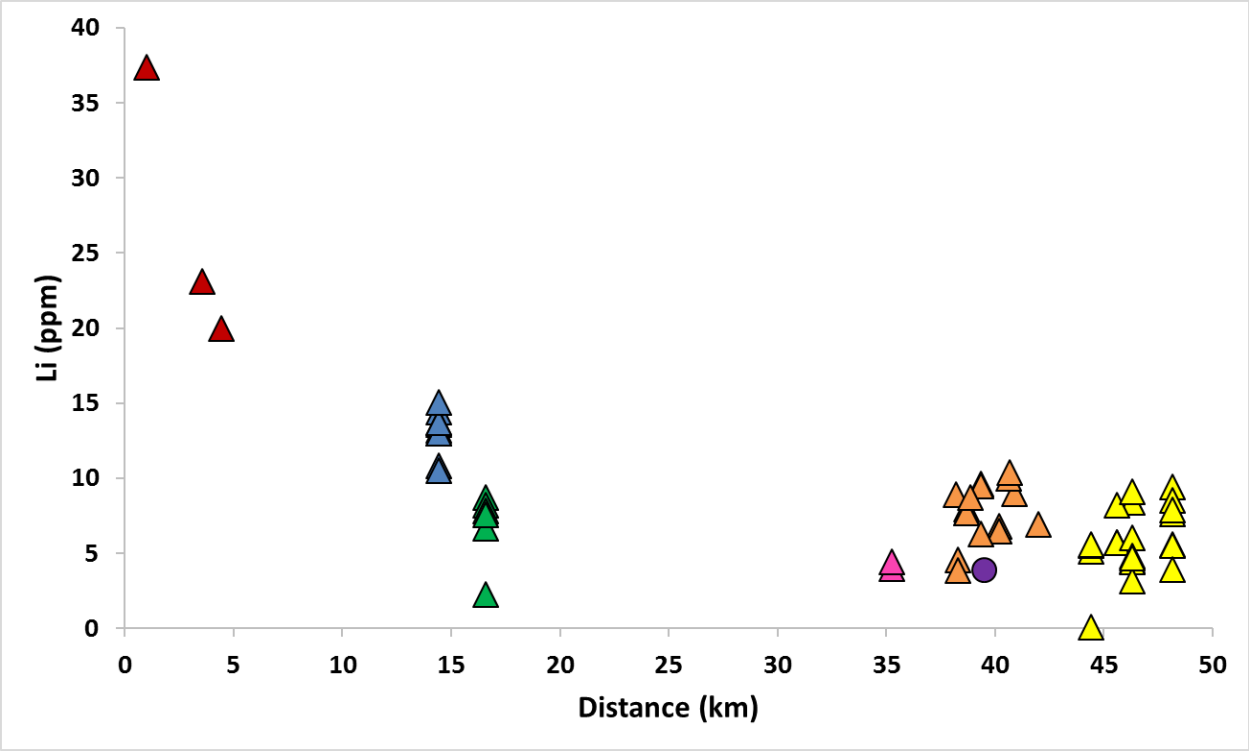

Figure 7. Li vs distance from the Valles Caldera. Values decrease with increased distance. Tierra Amarilla (yellow triangles), Penasco Springs (orange triangles), Indian Springs (pink triangles), Jemez Springs (green triangles), Soda Dam Springs (blue triangles), Valles Caldera (red triangles).

Samples from Soda Dam and Jemez Springs have [Sr] up to 4 ppm and more radiogenic $^{87}Sr/^{86}Sr$ values ~0.723. The increased [Sr] is due to water rock interaction along the flow path with the higher $^{87}Sr/^{86}Sr$ values indicating the water has been in contact with Precambrian basement granites ($^{87}Sr/^{86}Sr$ 0.7249 – 0.8163; Brookins and Laughlin, 1983) through deep circulation or has mixed with fluids that have risen from depth. Samples from Tierra Amarilla and Penasco Springs have the highest [Sr], from 5 to 20 ppm, but $^{87}Sr/^{86}Sr$ values lower than at Soda Dam, between 0.715 and 0.720. The increases in [Sr] with distance from the Valles Caldera are

explained by dissolution of relatively soluble sedimentary components (calcite, dolomite and gypsum) along the flow path. However, decrease in $^{87}Sr/^{86}Sr$ values indicate the addition of Sr with lower $^{87}Sr/^{86}Sr$ is occurring; we interpret this as reflecting dissolution of marine carbonates and evaporates ($^{87}Sr/^{86}Sr$ 0.7088 for Madera limestone, Vuataz et al., 1988). Simple binary mixing models for different end-members can be used to model the mixing process (Figure 6). Using equations from Faure (1977), the $^{87}Sr/^{86}Sr$ value of a fluid with 2 components (A and B) can be calculated using:

$$(^{87}Sr/^{86}Sr)_M = A/Sr_M + B ,$$

where $(^{87}Sr/^{86}Sr)_M$ is the Sr isotopic ratio in the mixture, Sr_M is the [Sr] in the mixture (found using, $Sr_M = Sr_A f_A + Sr_B (1-f_A)$ where Sr_A and Sr_B are [Sr] in the mixing components A and B respectively, and f_A is the mixing fraction of A, from 1 to 0.), and

$$a = Sr_A * Sr_B \; [(^{87}Sr / ^{86}Sr)_B - (^{87}Sr / ^{86}Sr)_A)] / Sr_A - Sr_B$$

$$b = Sr_A(^{87}Sr / ^{86}Sr)_A - Sr_B(^{87}Sr / ^{86}Sr)_B / Sr_A - Sr_B.$$

Two different models are presented. The Jemez Mixing model (solid brown line) uses an initial non-radiogenic end-member from the Valles Caldera ($^{87}Sr/^{86}Sr$ 0.70784), and Jemez Pueblo well end-member ($^{87}Sr/^{86}Sr$ 0.723216). The dissolution model (solid orange line) uses the Jemez Pueblo well as its initial end-member and Grassy Springs ($^{87}Sr/^{86}Sr$ 0.716926). Samples from the Valles Caldera, Soda Dam springs and Jemez Springs fall along the Jemez mixing model. This model explains the [Sr] and $^{87}Sr/^{86}Sr$ evolution of water from the Valles Caldera to the Jemez Pueblo well. Initially, water has low [Sr] and non-radiogenic $^{87}Sr/^{86}Sr$, it comes into contact

with basement granites in the fault zone, where dissolution of Sr occurs, increasing [Sr] with radiogenic $^{87}Sr/^{86}Sr$ values. If springs in the Tierra Amarilla/Penasco Springs region are sourced in part from the Valles Caldera, then similar, or higher $^{87}Sr/^{86}Sr$ values would be expected, however this is not the case. As discussed above, dissolution of Paleozoic rocks was suggested as an explanation for the high Cl values found in these springs. This process can also explain the higher [Sr], and associated lower $^{87}Sr/^{86}Sr$ values. The dissolution of marine carbonates and evaporates can increase [Sr], while lowering $^{87}Sr/^{86}Sr$ values due to the non-radiogenic nature of the Sr, $^{87}Sr/^{86}Sr \sim 0.709$. This is highlighted in Figure 6 inset, [Sr] vs [SO_4], where co-variation occurs. Further evidence of gypsum dissolution is found in the major ion chemistry. Water from Soda Dam springs and Jemez Springs plot along a mixing line with end-members from the Valles Caldera and East Fork Jemez River with the springs being the product of mixing between geothermal and meteoric water (Figure 2). If this approach is attempted for samples from Tierra Amarilla and Penasco Springs, the potential end-members are less clear. Focusing on the anion triangle, the Valles Caldera/Jemez River mixing line is apparent, but a secondary mixing line, increasing relative sulfate, is needed to move from Soda Dam/Jemez Springs, passing through Indian springs, to Tierra Amarilla/Penasco Springs. A possible way to achieve this is through the dissolution of gypsum, a rock present locally at Tierra Amarilla/Penasco Springs, but less so at Soda Dam and Jemez Springs.

Figure 5a shows how $\delta^{13}C$ varies with distance from the Valles Caldera. Values decrease with increasing distance. Values fall within the range of a mantle signature (-4

to -8‰), and the steady decrease away from the Valles Caldera can be attributed to addition of an organic carbon end-member (~28‰), which is added along the flow path due to mixing with meteoric water which will have percolated through soil layers. This is reflected in modeled percent organic carbon contribution, which shows an increase in the organically-derived component of dissolved inorganic carbon with distance from the Valles Caldera, up to 24% at Tierra Amarilla (McGibbon, 2015).

San Juan Basin connection

Water from the eastern San Juan Basin is hypothesized to be moving east (Frenzel and Lyford 1982, Figure 1); and, as such could be a source of water for the springs at Tierra Amarilla and Penasco Springs. Lack of water and gas data from the eastern side of the basin, particularly from deeper aquifers, ie the Madera, makes this difficult to establish. The differences in Cl concentrations that are used to suggest different water sources could be altered through the addition of a high Cl end-member water, the source of which would be the sedimentary aquifer waters of the San Juan Basin, with the high Cl being attributed to water-rock interaction, particularly the dissolution of evaporites. Samples from the eastern San Juan Basin are considered aquifer waters, and are interpreted to be dominated by meteoric water, which have evolved chemically, from a major ion point of view, with stable isotopes suggesting no mixing with endogenic water. The aquifer waters are expected to have low $^{3}He/^{4}He$, $\delta^{13}C\text{-}CO_2$ close to zero, from carbonates, with gases dominated by methane (Zhou et al., 2005). There is no manifestation of this in the waters at Tierra Amarilla or Penasco Springs. Gas samples show no evidence of detectable methane,

which is associated in dissolved gases from the San Juan basin. As such, we interpret San Juan basin aquifer waters to contribute negligibly to springs venting along the Nacimiento fault.

Nacimiento Mountains meteoric water connection

The springs at Tierra Amarilla and Penasco Springs clearly mix with meteoric water, but the $^{3}He/^{4}He$, $^{87}Sr/^{86}Sr$ and $^{13}C\text{-}CO_2$ values all indicate there has to be the addition of a deeper water component. The artesian properties of the springs is related to the upland recharge source, in that it provides the head for the ~100m elevation of the springs above the local base level (the Salado Arroyo). In the Tierra Amarilla spring group, variation in water chemistry occurs only at North Highway, a shift in anions, decrease in SO_4, increase in HCO_3, and greater temperature and geochemical variation than the southern springs along the Nacimiento fault. The greater range in North Highway is attributed to the location being slightly aside the fault and/or could be due to recharge which is not seen south of the river. The location away from the fault could potentially contribute less of a deep component, but with mixing of meteoric water from the Agua Zarca dip slope, suggested by the increased HCO_3. This spring is closest to the hypothesis of Hart (2001) for groundwater recharge from the Agua Zarca.

Conclusion

We investigated three hypotheses to identify the source of water for a series of springs discharging along the Nacimiento fault. Based on the trace elements, isotopes of

D, 18O, 3He/4He, 87Sr/86Sr and 13CeCO2, and groundwater contour flow lines, Tierra Amarilla and Penasco Springs are interpreted here to be a combination of geothermal water sourced from the Jemez Geothermal system, meteoric recharge-predominantly from along the flow path, with a small component of dip slope recharge for North Highway spring but negligible contribution from the San Juan Basin based on the absence of methane (Fig. 8). The meteoric component may differ subtly between spring groups, but it is the percentage geothermal (endogenic) end member plus the nature of water-rock interaction that dictates the observed water chemistry variability. Tierra Amarilla and Penasco Spring waters are distal parts of the Valles Caldera geothermal system in terms of CO2, helium, and geothermal tracers. Gas analysis shows that the endogenic volatiles include a component from the Earth's mantle and that excess CO2 is likely the carrier gas for deeply sourced crust and mantle volatiles that are geochemically potent and that degrade water quality in these springs. Helium isotopes also suggests a deeply sourced component to the springs with the observation of elevated 3He/4He, which decreases with distance from the Valles Caldera. Strontium isotopes indicate that spring water has been in contact with basement granites; however dissolution of SO4 increases Sr concentration and decreases 87Sr/86Sr values at Tierra Amarilla and Penasco Springs which is explained by water-rock interaction with Yeso and Todilto formations. Geochemistry of spring water, and map geometries suggests a fault connection between springs sampled at Soda Dam and Jemez Springs and spring groups at both Tierra Amarilla and Penasco Springs. Based on trace element ratios, and isotopes of carbon, helium and strontium, the latter of which suggest that

geothermal fluids move along NW-trending fault pathways across the Nacimiento Mountain block, faults demonstrably connect spring groups and allow mixing in complex proportions. The confined or semi-confined fault conduits provide connectivity within and between springs and spring systems and help explain geochemical similarities between Tierra Amarilla and Penasco Springs.

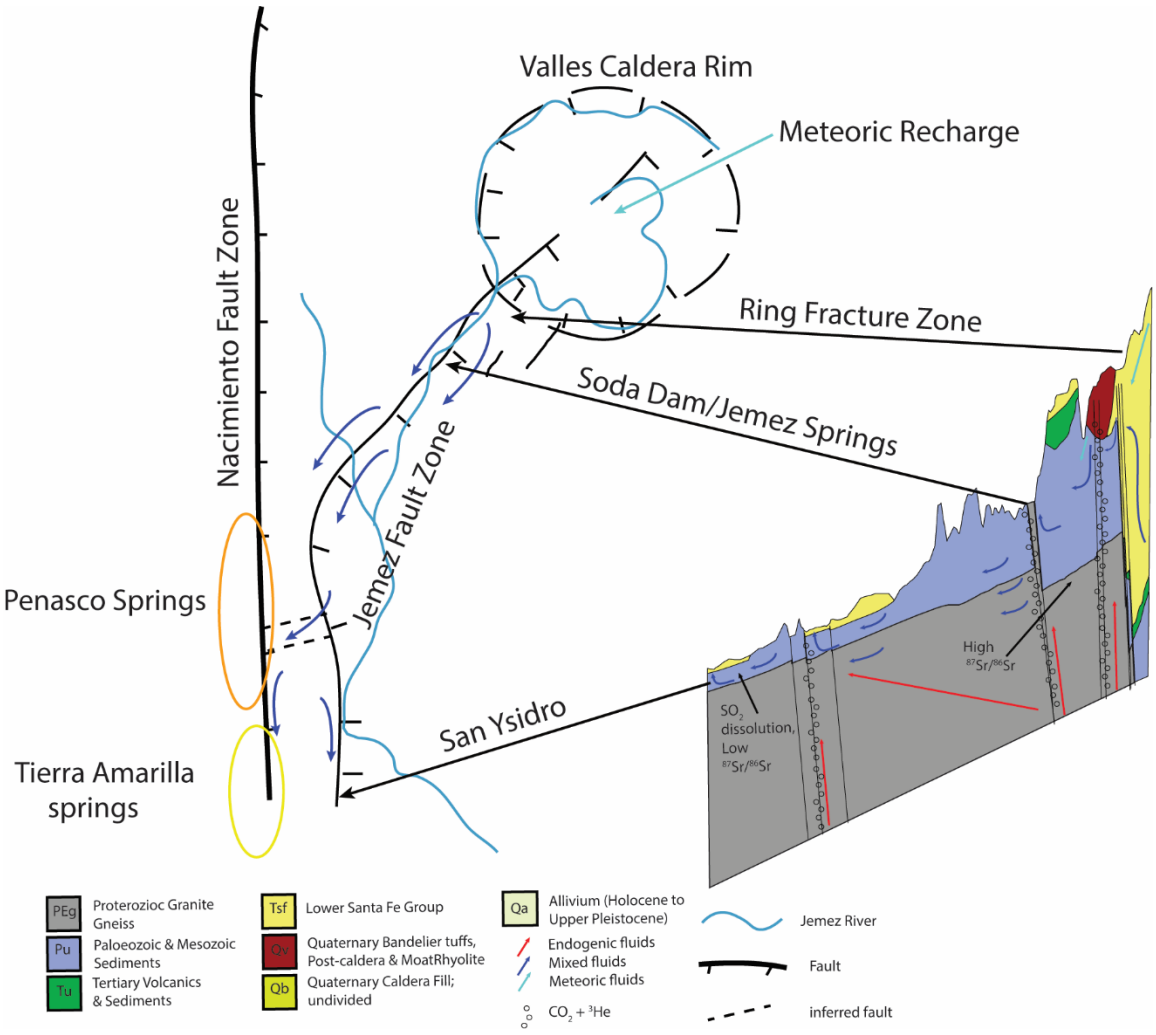

Figure 8. Schematic model of fluid movement and evolution, plan view and cross-section (modified from Goff 2009) from the Valles Caldera to Tierra Amarilla springs. Meteoric water (light blue arrow) in the Valles Caldera recharges the geothermal system where water circulates at depth before rising (red arrows), and discharging from the southeast of the caldera, along the Jemez fault zone. As water flows along the fault zone, it evolves due to water rock

interaction (dark blue arrows), mixing with other waters before discharging at multiple locations, Soda Dam and Jemez Springs. These waters are distinct due to low [Sr], [SO_4], and high $^{87}Sr/^{86}Sr$. At Tierra Amarilla and Penasco springs, dissolution of SO_4 increases [SO_4], with associated increases in [Sr] and decrease in $^{87}Sr/^{86}Sr$, explaining the distinct chemistry found at these springs.

Acknowledgements

We thank AbdulMedhi Ali, Viorel Atudorei, Yemane Asmerom, and Victor Polyak for laboratory assistance (the Analytical Laboratory, Center for Stable Isotopes, and Radiogenic Isotope Lab, respectively). We thank the BLM, the Zia Pueblo Kevin Madalena of the Pueblo of Jemez, and Robert Parmenter of the Valles Caldera National Park for allowing access to the field area. We would also like to thank the editors and reviewers for the time and assistance. This work was supported in part from NSF EPSCoR, Geothermal (Award #IIA-1301346; to Laura Crossey) and student awards (to C. McGibbon) from New Mexico Geological Society (NMGS), the Award for Excellence in Field Work in New Mexico 2014, the Wanek Scholarship 2014, NMGS Grants-in-aid 2014, Caswell Silver fellowship 2014, Caswell Silver Scholarship international 2013. Access to Valles Caldera was from the NPS, VALL-2017-SCI-0014.

References

American Public Health Association, 1995. Standard Methods for the Examination of Water and Wastewater, 19th ed. Eaton, A.D., Clesceri, L.S., and Greenberg

Andrews, J.N., 1985. The isotopic composition of radiogenic helium and its use to study groundwater movement in confined aquifers. Chemical Geology 49, 339–351. https://doi.org/10.1016/0009-2541(85)90166-4

Ballentine, C.J., Burnard, P.G., 2002. Production, Release and Transport of Noble Gases in the Continental Crust. Reviews in Mineralogy and Geochemistry 47, 481–538. https://doi.org/10.2138/rmg.2002.47.12

Banerjee, A., Person, M., Hofstra, A., Sweetkind, D., Cohen, D., Sabin, A., Unruh, J., Zyvoloski, G., Gable, C.W., Crossey, L., 2011. Deep permeable fault–controlled helium

transport and limited mantle flux in two extensional geothermal systems in the Great Basin, United States. Geology 39, 195–198.

Banner, J.L., 1995. Application of the trace element and isotope geochemistry of strontium to studies of carbonate diagenesis. Sedimentology 42, 805–824. https://doi.org/10.1111/j.1365-3091.1995.tb00410.x

Brookins, D.G., Laughlin, A.W., 1983. Rb-Sr geochronologic investigation of precambrian samples from deep geothermal drill holes, Fenton Hill, New Mexico. Journal of Volcanology and Geothermal Research, Geothermal Energy of Hot Dry Rock 15, 43–58. https://doi.org/10.1016/0377-0273(83)90095-1

Caine, J.S., Evans, J.P., Forster, C.B., 1996. Fault zone architecture and permeability structure. Geology 24, 1025–1028.

Chapin, C.E., Cather, S.M., 1994. Tectonic setting of the axial basins of the northern and central Rio Grande rift. Geological Society of America Special Papers 291, 5–26. https://doi.org/10.1130/SPE291-p5

Chiodini, G., Frondini, F., Kerrick, D.M., Rogie, J., Parello, F., Peruzzi, L., Zanzari, A.R., 1999. Quantification of deep CO2 fluxes from Central Italy. Examples of carbon balance for regional aquifers and of soil diffuse degassing. Chemical Geology 159, 205–222. https://doi.org/10.1016/S0009-2541(99)00030-3

Cron, B., 2011. Geochemical characteristics and microbial diversity of CO2-rich mound springs of the Tierra Amarilla anticline, New Mexico. M.S. Thesis, University of New Mexico.

Crossey, L.J., Fischer, T.P., Patchett, P.J., Karlstrom, K.E., Hilton, D.R., Newell, D.L., Huntoon, P., Reynolds, A.C., Leeuw, G.A.M. de, 2006. Dissected hydrologic system at the Grand Canyon: Interaction between deeply derived fluids and plateau aquifer waters in modern springs and travertine. Geology 34, 25–28. https://doi.org/10.1130/G22057.1

Crossey, L.J., Karlstrom, K.E., Springer, A.E., Newell, D., Hilton, D.R., Fischer, T., 2009. Degassing of mantle-derived CO2 and He from springs in the southern Colorado Plateau region--Neotectonic connections and implications for groundwater systems. Geological Society of America Bulletin 121, 1034–1053. https://doi.org/10.1130/B26394.1

Crossey, L.J., Karlstrom, K.E., Newell, D.L., Kooser, A., Tafoya, A., 2011. The La Madera travertines, Rio Ojo Caliente, northern New Mexico: investigating the linked system of CO_2-rich springs and travertines as neotectonic and paleoclimate indicators. Geology of the Tusas Mountains and Ojo Caliente Area, New Mexico Geological Society, Guidebook 62, 301–316.

Crossey, L.J., Sherson, L., Karlstrom, K.E., McGibbon, C., Jochems, A., Ali, A., Person, M., Dahm, D., Parmenter, R., 2012. The water quality challange: Using new technology to track tectonic salinity contributions that impair surface and groundwater. GSA Abstract.

Crossey, L.J., Karlstrom, K.E., Schmandt, B., Crow, R.R., Colman, D.R., Cron, B., Takacs-Vesbach, C.D., Dahm, C.N., Northup, D.E., Hilton, D.R., Ricketts, J.W., Lowry, A.R., 2016. Continental smokers couple mantle degassing and distinctive microbiology within continents. Earth and Planetary Science Letters 435, 22–30. https://doi.org/10.1016/j.epsl.2015.11.039

Crouch, T.M., 1994. Hydrogeology and aquifer test on the San Andres-Glorieta Aquifer on the southwest part of the Zuni Indian Reservation, Cibola County, New Mexico (USGS Numbered Series No. 94–4033), Water-Resources Investigations Report. U.S. Dept. of the Interior, U.S. Geological Survey ; Earth Science Information Center, Open-File Reports Section [distributor],.

Dam, W.L., 1995. Geochemistry of ground water in the Gallup, Dakota, and Morrison aquifers, San Juan Basin, New Mexico (USGS Numbered Series No. 94–4253), Water-Resources Investigations Report. U.S. Geological Survey, [Water Resources Division, New Mexico District] ; Can be purchased from U.S.G.S. Earth Science Information Center, Open-File Reports Section.

Dondanville, R.F., 1971. The Hydrothermal Geology of the Valles Caldera, Jemez Mountains, New Mexico. Union Oil Co.

Dondanville, R.F., 1979. Geologic Characteristics of Valles Caldera Geothermal System in New Mexico. AAPG Bulletin 63, 825–826.

Faure, G., 1986. Principles of Isotope Geology, 2nd Edition, 2 edition. ed. Wiley, New York

Frenzel, P.F., Lyford, F.P., 1982. Estimates of Vertical Hydraulic Conductivity and Regional Ground Water Flow Rates in Rocks of Jurrasic and Cretaceous Ahe, San Juan Basin, New Mexico and Colorado. USGS water-Resources Investigation 82-4015.

Gardner, W.P., Susong, D.D., Solomon, D.K., Heasler, H.P., 2011. A multitracer approach for characterizing interactions between shallow groundwater and the hydrothermal system in the Norris Geyser Basin area, Yellowstone National Park. Geochemistry Geophysics Geosystems 12. https://doi.org/10.1029/2010GC003353

Giggenbach, W.F., Gouguel, R.., 1988. Methods for the Collection and Analysis of Geothermal and Volcanic Water and Gas Samples. Chemistry Division, Department of Scientific and Industrial Research.

Goff, F.E., Grigsby, C.O., Trujillo Jr., P.E., Counce, D., Kron, A., 1981. Geology, water geochemistry and geothermal potential of the jemez springs area, Canon de San Diego, new Mexico. Journal of Volcanology and Geothermal Research 10, 227–244. https://doi.org/10.1016/0377-0273(81)90064-0

Goff, F., Gardner, J., Vidale, R., Charles, R., 1985. Geochemistry and isotopes of fluids from sulphur springs, Valles Caldera, New Mexico. Journal of Volcanology and Geothermal Research 23, 273–297. https://doi.org/10.1016/0377-0273(85)90038-1

Goff, F., Rowley, J., Gardner, J.N., Hawkins, W., Goff, S., Charles, R., Wachs, D., Maassen, L., Heiken, G., 1986. Initial results from VC-1, First Continental Scientific Drilling Program Core Hole in Valles Caldera, New Mexico. J. Geophys. Res. 91, 1742–1752. https://doi.org/10.1029/JB091iB02p01742

Goff, F., Shevenell, L., Gardner, J.N., Vuataz, F.-D., Grigsby, C.O., 1988. The hydrothermal outflow plume of Valles Caldera, New Mexico, and a comparison with other outflow plumes. J. Geophys. Res. 93, 6041–6058. https://doi.org/10.1029/JB093iB06p06041

Goff, F., Janik, C.J., 2002. Gas geochemistry of the Valles caldera region, New Mexico and comparisons with gases at Yellowstone, Long Valley and other geothermal systems. Journal of Volcanology and Geothermal Research 116, 299–323. https://doi.org/10.1016/S0377-0273(02)00222-6

Gutzler, D., 2007. Climate change and water resources. New Mexico Earth Matters 7.

Hart, D.V., 2001. Tierra Amarilla Anticline and its Travertine Springs, New Mexico.

Heiken, G., Goff, F., Gardner, J.N., Baldridge, W.S., Hulen, J.B., Nielson, D.L., Vaniman, D., 1990. The Valles/Toledo Caldera Complex, Jemez Volcanic Field, New Mexico. Annual Review of Earth and Planetary Sciences 18, 27.

Cook, P.P.G., Herczeg, A.L., 2000. Environmental Tracers in Subsurface Hydrology. Kluwer Academic Pub.

Herczeg, A., Edmunds, M., 2000. Inorganic Environmental tracers; in Environmental Tracers in Subsurface Hydrology. Kluwer Academic Pub.

Hilton, D.R., 1996. The helium and carbon isotope systematics of a continental geothermal system: results from monitoring studies at Long Valley caldera (California, U.S.A.). Chemical Geology 127, 269–295. https://doi.org/10.1016/0009-2541(95)00134-4

Hilton, D.R., Fischer, T.P., Marty, B., 2002. Noble Gases and Volatile Recycling at Subduction Zones. Reviews in Mineralogy and Geochemistry 47, 319–370. https://doi.org/10.2138/rmg.2002.47.9

Hogan, J.F., Phillips, F.M., Mills, S.K., Hendrickx, J.M., Ruiz, J., Chesley, J.T., Asmerom, Y., 2007. Geologic origins of salinization in a semi-arid river: The role of sedimentary basin brines. Geology 35, 1063–1066.

Hulen, J.B., Nielson, D.L., 1986. Hydrothermal alteration in the Baca Geothermal System, Redondo Dome, Valles Caldera, New Mexico. Journal of Geophysical Research: Solid Earth 91, 1867–1886. https://doi.org/10.1029/JB091iB02p01867

Ingebritsen, S.E., Sanford, W.E., Neuzil, C.E., 2006. Groundwater in Geologic Processes, 2 edition. ed. Cambridge University Press, Cambridge ; New York.

Karlstrom, K.E., Crossey, L.J., Hilton, D.R., Barry, P.H., 2013. Mantle 3He and CO2 degassing in carbonic and geothermal springs of Colorado and implications for neotectonics of the Rocky Mountains. Geology. https://doi.org/10.1130/G34007.1

Kaufman, G., 2011. Innovative Exploration Techniques for Geothermal Assessment at Jemez Pueblo, New Mexico.

Kelley, S., Osburn, G., Kempter, K., 2007. Geology of Canyon de San Diego, Southwestern Jemez Mountains, North-Central New Mexico. New Mexico Geol. Soc. Guidebook, 28th Field Conf., Jemez Mountains II.

Kelley, V.C., 1952. Tectonics of the Rio Grande depression of central New Mexico, in: Guidebook of the Rio Grande Country, Central New Mexico, Third Field Conference. p. 97.

Kirk, M.F., Crossey, L.J., Takacs-Vesbach, C., Newell, D.L., Bowman, R.S., 2009. Influence of upwelling saline groundwater on iron and manganese cycling in the Rio Grande floodplain aquifer. Applied Geochemistry 24, 426–437.

Lambert, S.J., Epstein, S., 1980. Stable isotope investigations of an active geothermal system in Valles Caldera, Jemez Mountains, New Mexico. Journal of Volcanology and Geothermal Research 8, 111–129. https://doi.org/10.1016/0377-0273(80)90010-4

McGibbon, C., 2015. Carbonic springs as distal manifestations of the Jemez geothermal system, San Yisodro, New Mexico, highlighting the importance of fault pathways and hydrochemical fluid mixing. M.S. Thesis, University of New Mexico.

New Mexico Bureau of Geology and Mineral Resources, 2003. Geologic Map of New Mexico, 1:500,000: New Mexico Bureau of Geology and Mineral Resources

Newell, D.L., Crossey, L.J., Karlstrom, K.E., Fischer, T.P., Hilton, D.R., 2005. Continental-scale links between the mantle and groundwater systems of the western United States: Evidence from travertine springs and regional He Isotope data. GSA Today 15, 5.

Parkhurst, D., 1995. Users guide to PHREEQC-A computer program for speciation, reaction-path, advective-transport, and onverse geochemical calculations.

Phillips, F.M., Mills, S., Hendrickx, M.H., Hogan, J., 2003. Environmental tracers applied to quantifying causes of salinity in arid-region rivers: Results from the Rio Grande Basin, Southwestern USA, in: Abdulrahman S. Alsharhan and Warren W. Wood (Ed.), Developments in Water Science. Elsevier, pp. 327–334.

Pin, C., Bassin, C., 1992. Evaluation of a strontium-specific extraction chromatographic method for isotopic analysis in geological materials. Analytica Chimica Acta 269, 249–255. https://doi.org/10.1016/0003-2670(92)85409-Y

Piper, A.M., 1944. A graphic procedure in the geochemical interpretation of water-analyses. Eos Trans. AGU 25, 914–928. https://doi.org/10.1029/TR025i006p00914

Renick, B.C., 1931. Geology and ground-water resources of western Sandoval County, New Mexico (USGS Numbered Series No. 620), Water Supply Paper. U.S. Govt. Print. Off.,.

Schmandt, B., Humphreys, E., 2010. Complex subduction and small-scale convection revealed by body-wave tomography of the western United States upper mantle. Earth and Planetary Science Letters 297, 435–445.

Sharp, Z., 2007. Principles of stable isotope geochemistry. Upper Saddle River, N.J. : Pearson/Prentice Hall, c2007.

Shevenell L., G.F., 1987. Hydrochemical data for thermal and non-thermal waters and gases of Valles caldera-southern Jemez Mountains region, New Mexico. Los Alamos National Laboratory Report LA-10923-OBES, 60 pp.

Slack, P.B., 1973. Structural Geology of the Northeast Part of the Rio Puerco Fault Zone, Sandoval County, New Mexico. University of New Mexico.

Trainer, F.W., 1974. Ground water in the southwestern part of the Jemez Mountains volcanic region, New Mexico. New Mexico Geol. Soc. Guidebook, 25th Field Conf., Ghost Ranch 1974.

Trainer, F.W., Rogers, R.J., Sorey, M.L., 2000. Geothermal hydrology of Valles Caldera and the southwestern Jemez Mountains, New Mexico (No. WRI-2000-4067). United States Geological Survey.

Vautaz, F., Goff, F., 1986. Isotope geochemistry of Thermal and Nonthermal Waters in the Valles Caldera, Jemez Mountains, Northern New Mexico. Journal of Geophysical Research 91, 1835–1853.

Vuataz, F.-D., Goff, F., Fouillac, C., Calvez, J.-Y., 1988. A strontium isotope study of the VC-1 core hole and associated hydrothermal fluids and rocks from Valles Caldera, Jemez Mountains, New Mexico. Journal of Geophysical Research: Solid Earth 93, 6059–6067. https://doi.org/10.1029/JB093iB06p06059

Wassenaar, L.I., Ahmad, M., Aggarwal, P., van Duren, M., Pöltenstein, L., Araguas, L., Kurttas, T., 2012. Worldwide proficiency test for routine analysis of δ^2H and $\delta^{18}O$ in water by isotope-ratio mass spectrometry and laser absorption spectroscopy. Rapid Commun. Mass Spectrom. 26, 1641–1648. https://doi.org/10.1002/rcm.6270

White, W., 1985. A new look at the salt load of the Rio Salado, New Mexico. Bureau of Indian Affairs, New Mexico.

Williams, A.J., Crossey, L.J., Karlstrom, K.E., Newell, D., Person, M., Woolsey, E., 2013. Hydrogeochemistry of the Middle Rio Grande aquifer system — Fluid mixing and salinization of the Rio Grande due to fault inputs. Chemical Geology 351, 281–298. https://doi.org/10.1016/j.chemgeo.2013.05.029

Woodward, L.A., 1987. Geology and mineral resources of Sierra Nacimiento and vicinity, New Mexico New Mexico Bureau of Mines & Mineral Resources: 42. Socorro, NM : New Mexico Bureau of Mines & Mineral Resources, 1987.

Zhou, Z., Ballentine, C. J., Kipfer, R., Schoell, M., & Thibodeaux, S., 2005. Noble gas tracing of groundwater/coalbed methane interaction in the San Juan Basin, USA. Geochimica et Cosmochimica Acta, 69(23), 5413–5428. https://doi.org/10.1016/J.GCA.2005.06.027

Zimmerer, M.J., Lafferty, J., Coble, M.A., 2016. The eruptive and magmatic history of the youngest pulse of volcanism at the Valles caldera: Implications for successfully dating late Quaternary eruptions. Journal of Volcanology and Geothermal Research 310, 50–57. https://doi.org/10.1016/j.jvolgeores.2015.11.021

SUPPLIMENTARY MATERIAL

Supplementary Figures and Tables

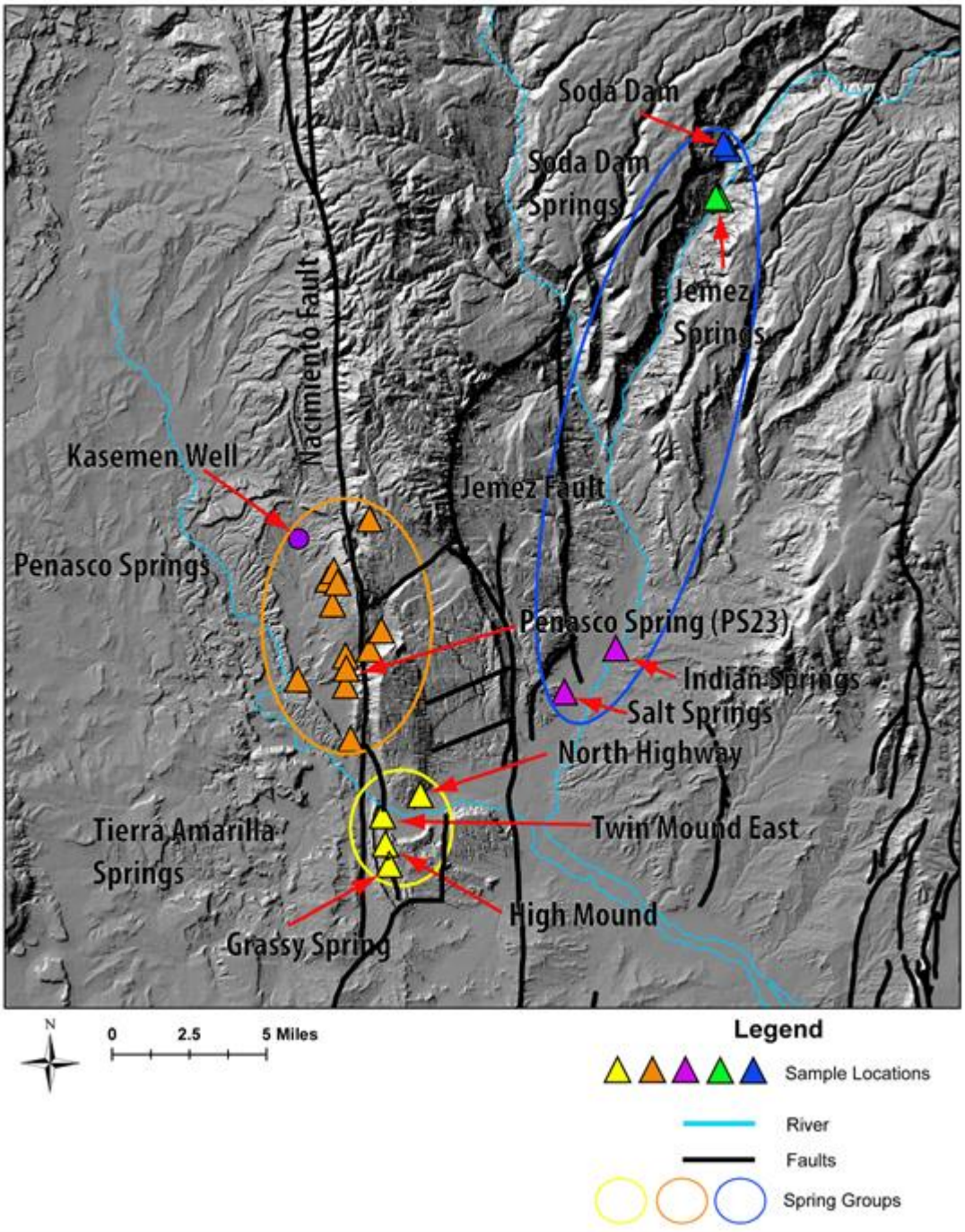

Figure S1. DEM (Earth Data Analysis Center, 1996) map of the three spring groups of this study, showing individual spring sampling sites, and naming of grouped springs.

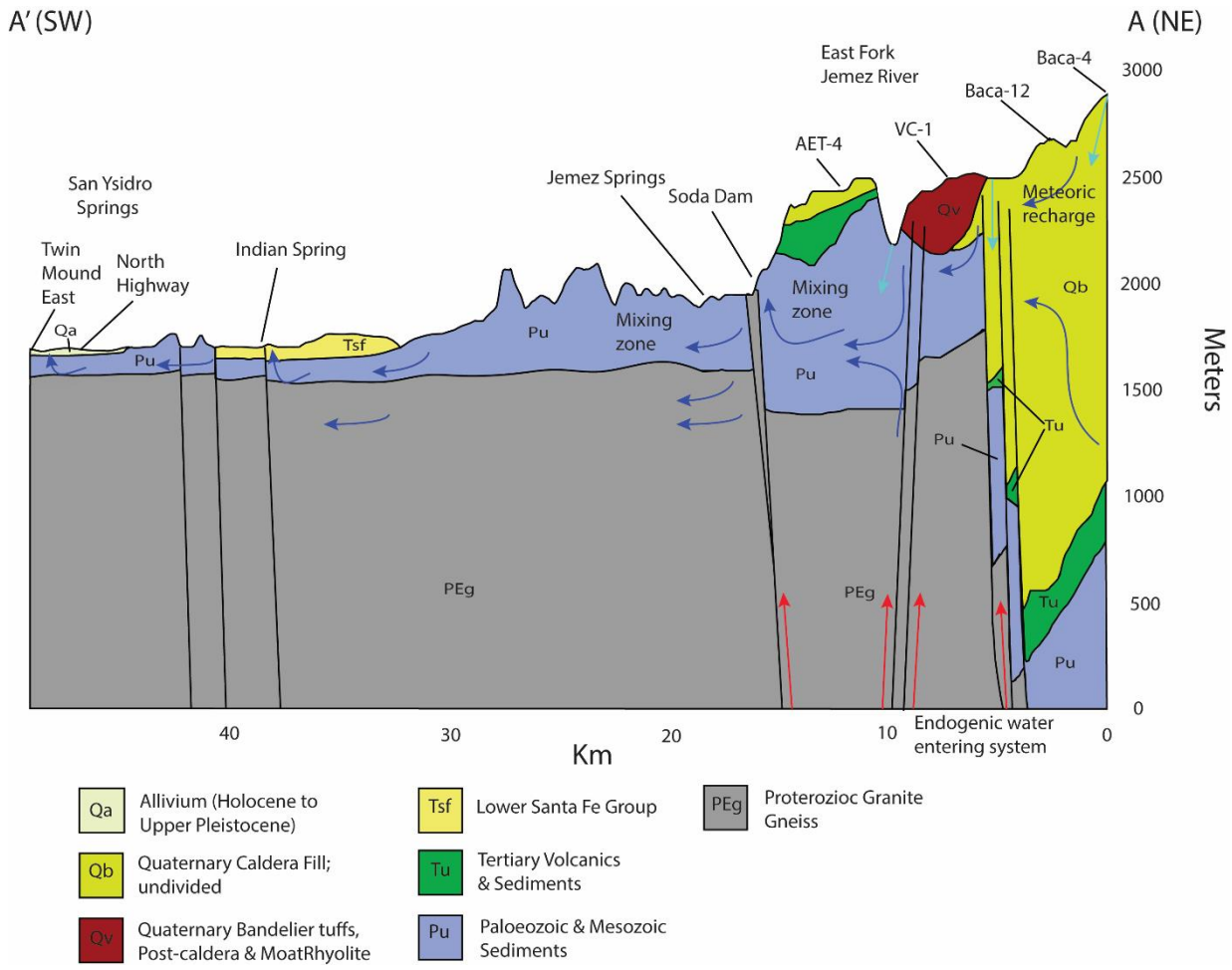

Figure S2. Cross section modified from Goff (2009) from the Valles Caldera to Tierra Amarilla springs, drawn subparallel to the plane of the Jemez fault system, cross section line on figure 2. Flow arrows are modified from Goff (2009) by adding red arrows that depict deeply sourced upward flow; light blue arrows depict meteoric recharge, dark blue arrows depict shallower fault-influenced flow volumetrically dominated by meteoric water but geochemically influenced by mixing of shallowly and deeply sourced groundwater. Line of cross section shown in Figs. 2 and 4.

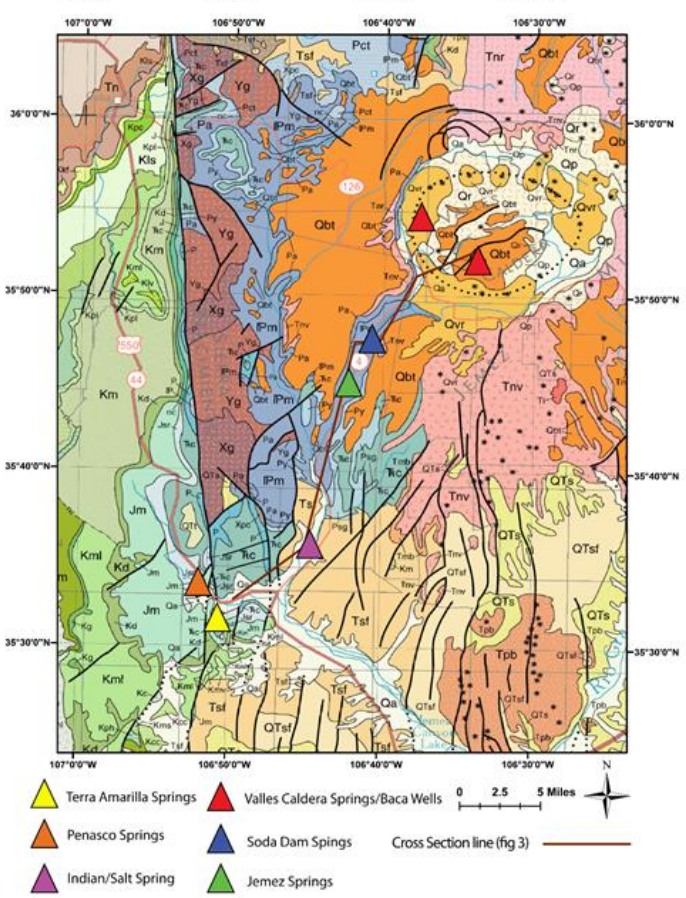

Figure S3.**3.** Geologic map encompassing the broader study area and showing spring group locations (New Mexico Bureau of Mineral Resources, 2003). Prevolcanic units in the study area include: Precambrian basement rocks dominated by granites (Xg and Yg), Pennsylvanian Madera Group (IPm), Permian Abo (Pa) and Yeso (Py) formations, Glorieta Sandstone and San Andres Limestone (Psg), Triassic Petrified Forest and Agua Zarca Sandstone Members of the Chile Group (Tc), Jurassic Entrada and Todilto formations (Jsr), Jurassic Morrison Formation (Jr), and Cretaceous units of the San Juan Basin (K). Rio Grande rift fill is the Santa Fe Group (Tsf and QTsf). Volcanic units are basalt (Tpb), Tertiary Jemez Mountain volcanics (Tnv), Quaternary Bandelier tuff (Qbt) and post-caldera flows (Qvr). Location of cross section for figure 3 is shown.

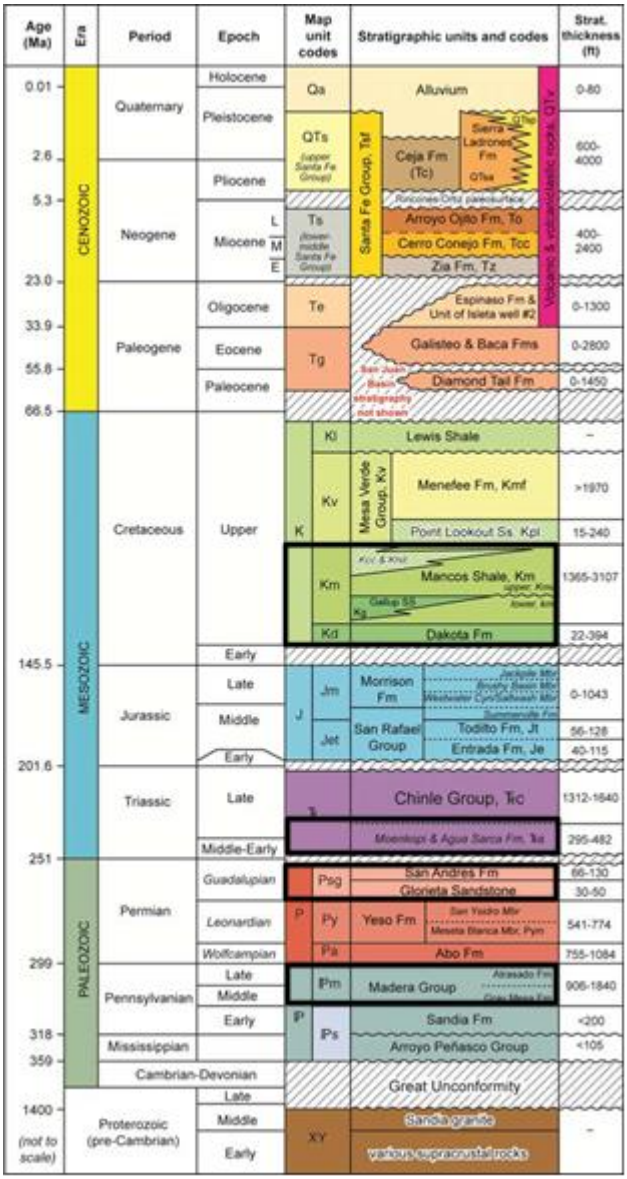

Figure S4. Regional stratigraphy (Connell, 2011); major aquifers in the area are highlighted in black.

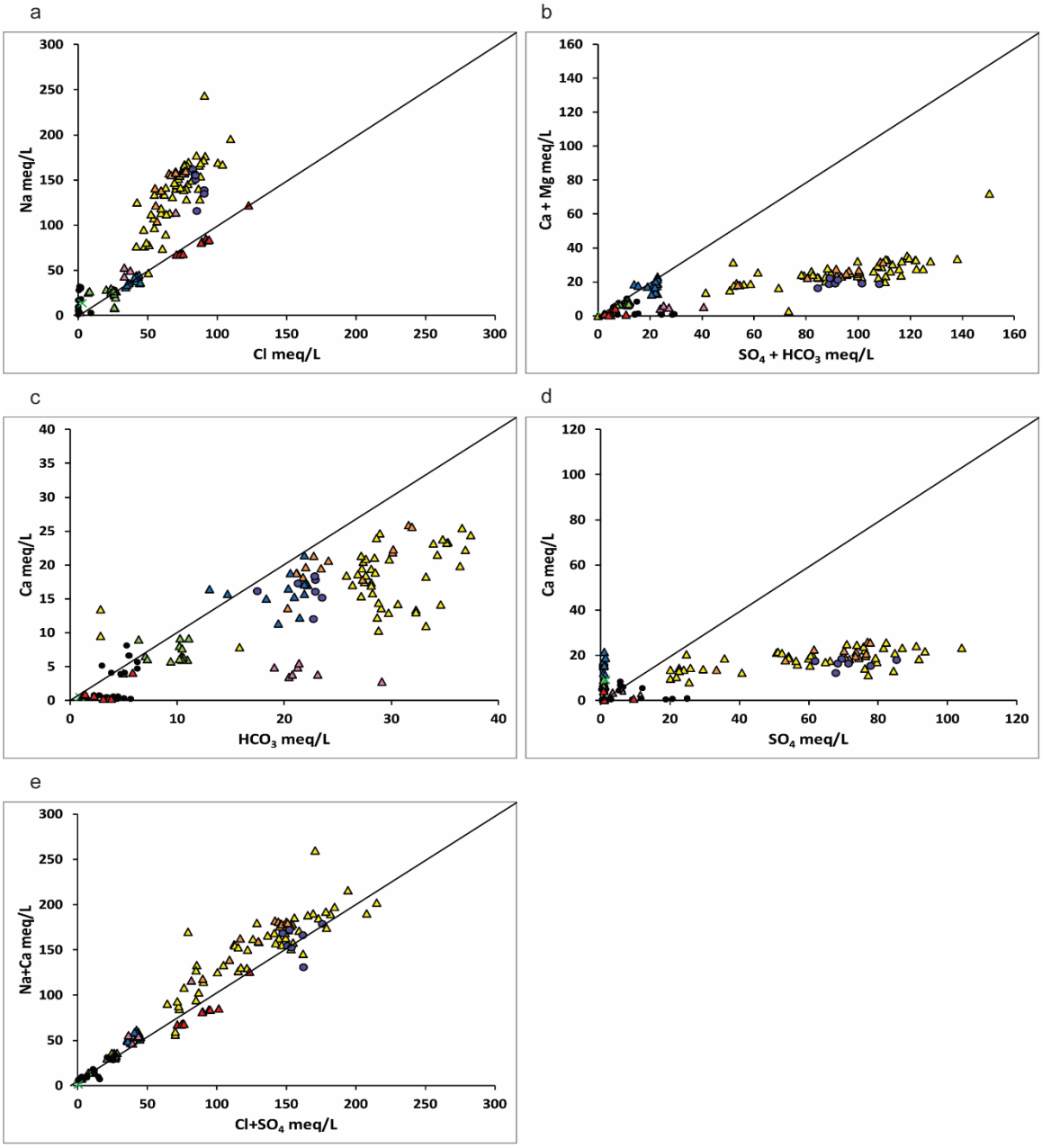

Figure S5. Chemical variation diagrams (1 to 1 line show for reference in each plot). a) Na vs Cl. For the majority of samples groundwater is enriched in Na with respect to Cl, suggesting other processes besides the dissolution of halite. b) Ca+Mg vs SO_4+HCO. Samples are enriched in SO_4 + HCO_3 in relation to Ca + Mg; along with the enrichment of Na, this could suggest cation exchange removing Na from solution and result enrichment of Ca or Mg. c) Ca vs HCO_3 showing enrichment in HCO_3 for spring samples; Psg Aquifer sitting on the 1:1 ratio line and enrichment in Ca for the Rio Salado, d) Ca vs SO_4 showing enrichment in sulfate. e) Ca+Na vs Cl+SO_4, highlighting relative increase in Ca+Na in relation Cl+SO_4.

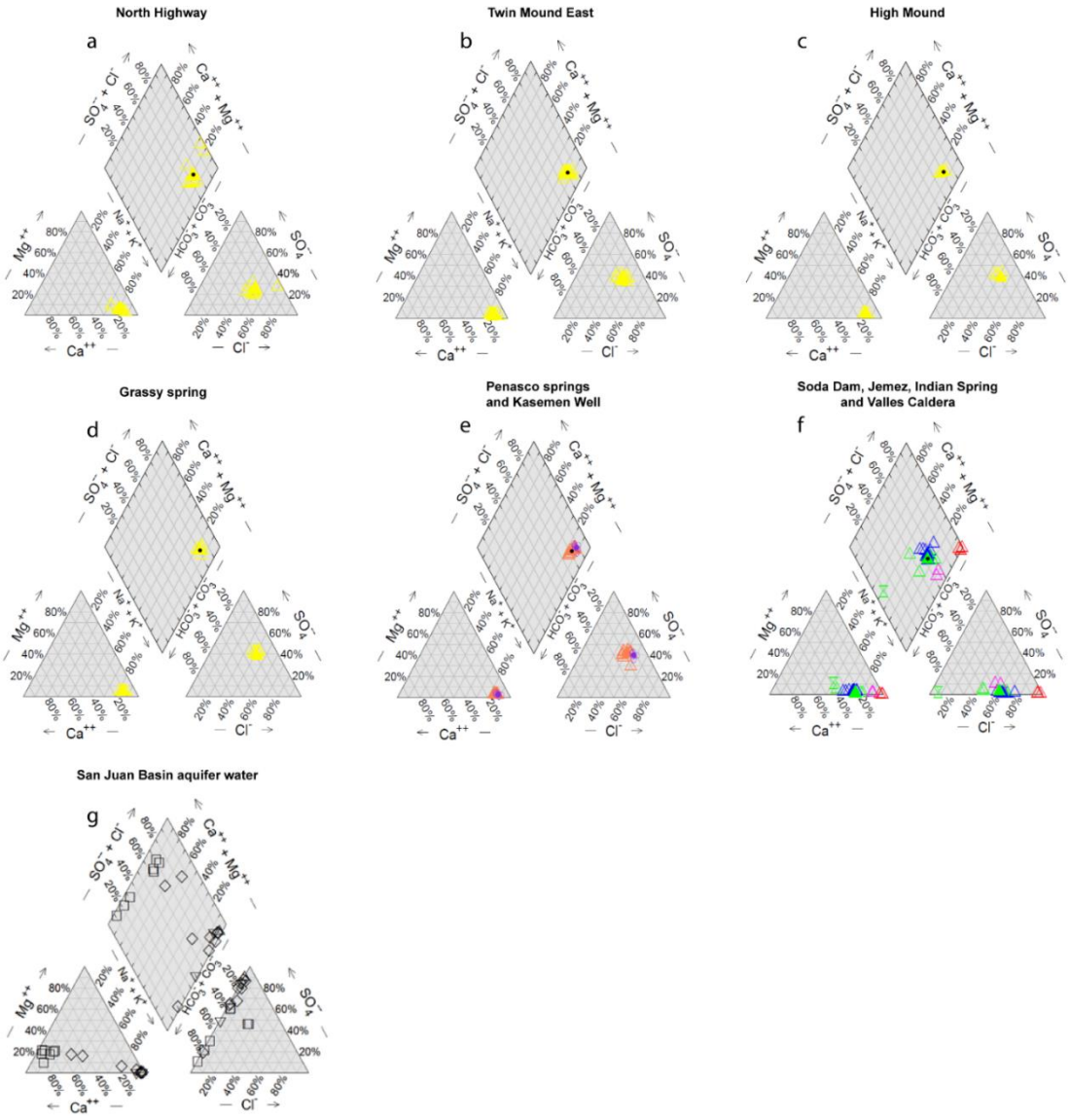

Figure S6. Piper diagrams showing individual spring chemistry for a) North Highway, b) Twin Mound East, c) High mound, d) Grassy spring, e) Penasco springs (orange triangles) and Kasemen well (purple circle), f) Soda Dam (blue triangles), Jemez Springs (green triangles), Indian springs (purple pink triangles), East fork Jemez River (green X) and Valles Caldera (red triangles) and g) San Juan Basin aquifers (San Andreas/Glorieta aquifer – squares, Dakota aquifer – triangles, Gallup aquifer – diamond, Morrison aquifer – inverted triangles).

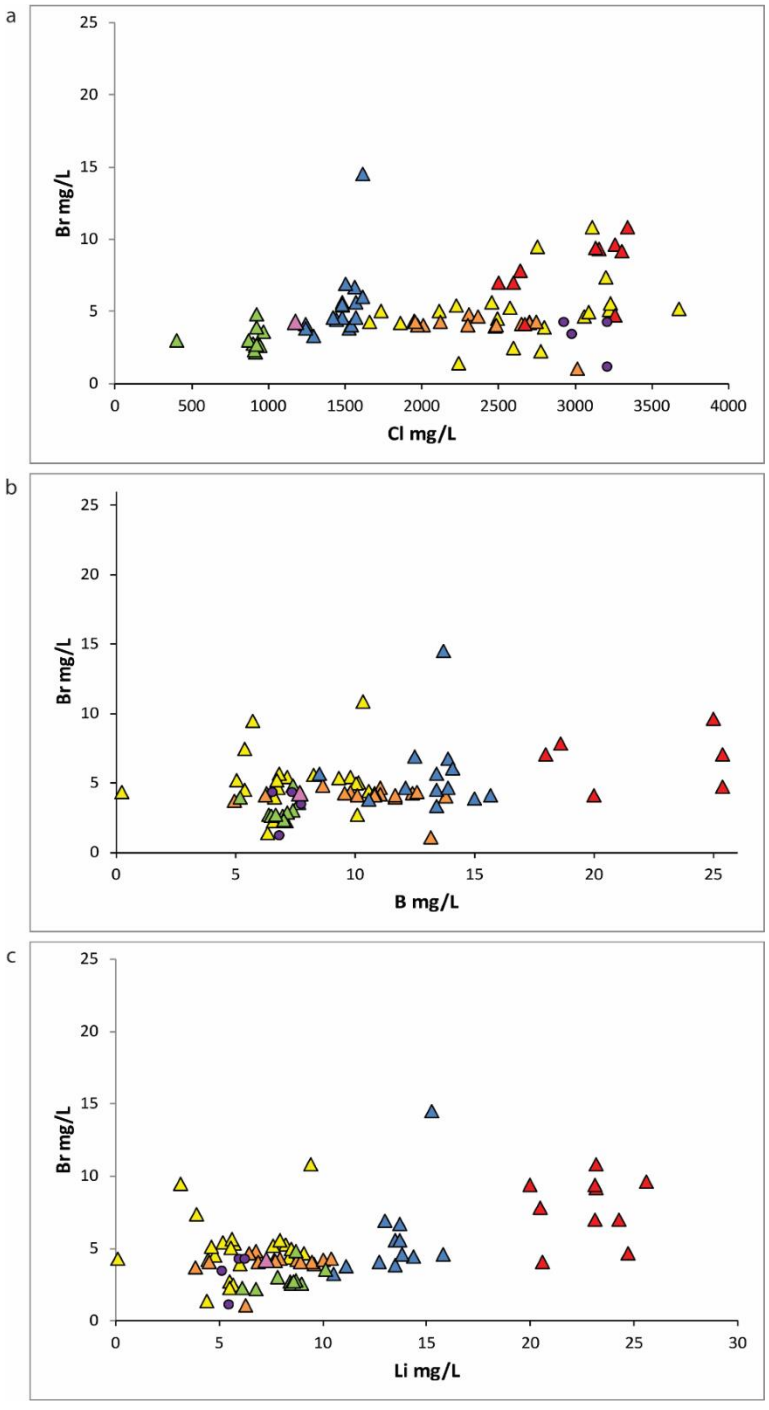

Figure S7. Trace element plots, a) Br vs Cl shows increasing Cl with constant Br, b) Br vs B show how Br values remain relatively constant with increasing B values, c) Br vs Li has a greater increase in Li, in relation to Br.

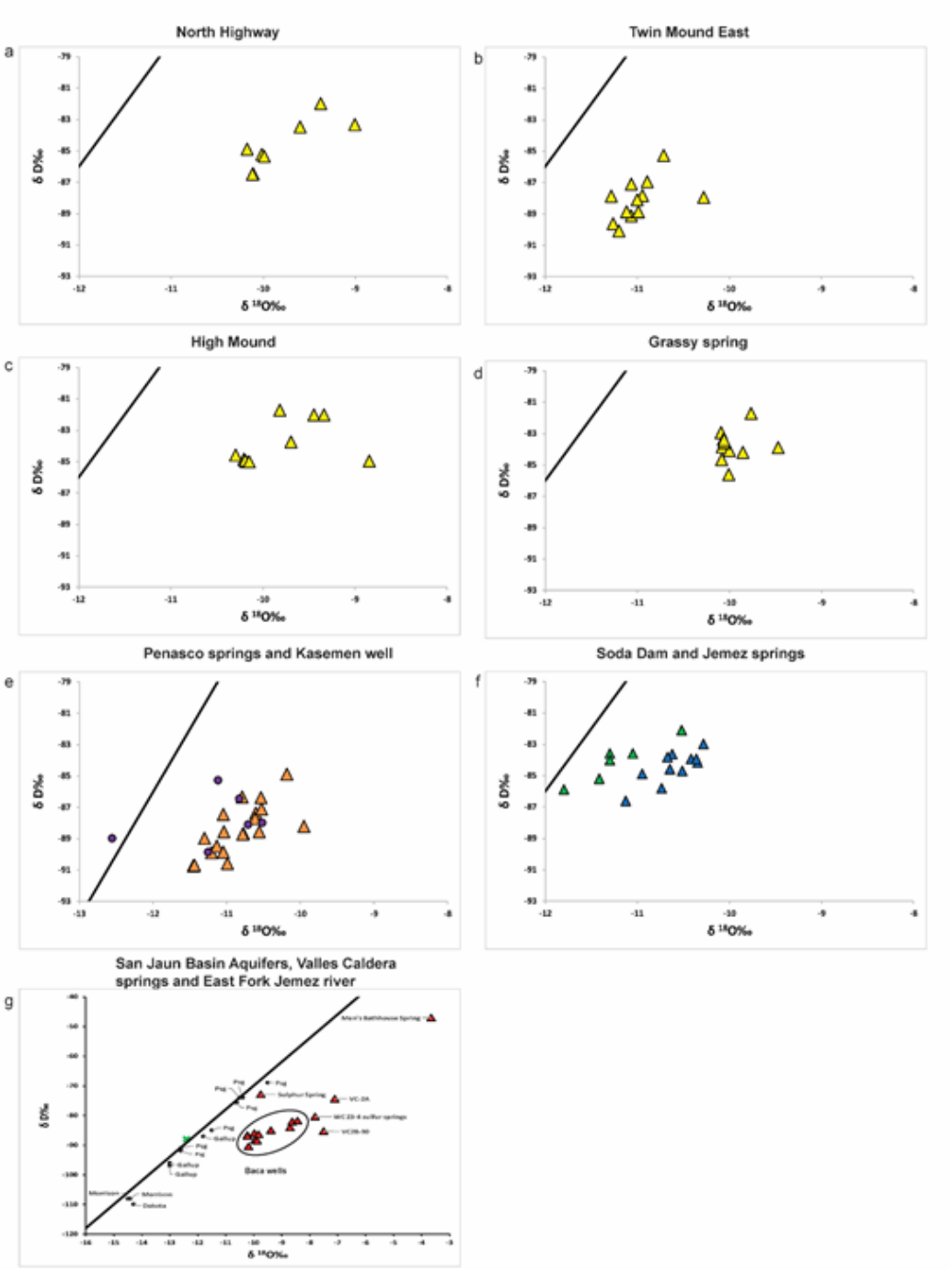

Figure S8. Stable isotopes of ^{18}O and D for a) North Highway, b) Twin Mound East, c) High mound, d) Grassy spring, e) Penasco springs, f) Soda Dam (blue triangles) and Jemez Springs (green triangles) and g) Valles Caldera (red triangles), East Fork Jemez river (green X) and San Juan Basin aquifers (black dots, individually labelled). The Kasemen Well sample which plots close to the GWML is considered meteoric water. The well has been capped, but now leaks, and the area surrounding the well is flooded. If sampling took place after a rain event, then it is possible to be primarily meteoric water, rather than representing well water

CHAPTER 2: Using Time-series environmental sensors to investigating fluid movement in the Nacimiento fault through analysis of Earth tides and Barometric Pressure

C. McGibbon[1], L. J. Crossey[1], and K. E. Karlstrom[1]

[1] Earth and Planetary Science, University of New Mexico, Albuquerque, NM, USA
Corresponding author: Chris McGibbon (mcgibbon@unm.edu)

Abstract

Over two years of autonomous sensor data from a series of artesian springs located along the Nacimiento Fault, NM, were analyzed to assess temporal and spatial variations, provide information about fluid movement within the fault zone, and aquifer properties. Barometric Response Function indicates springs are semi-confined with a barometric efficiency of ~0.2, but more interestingly, have a two-component response to atmospheric pressure events, an initial unconfined response, followed by a confined response. The unconfined response has negative values indicating water depth initially increases with increases in barometric pressure. A fault zone hydrologic system model is used to explain this phenomenon, where water held in storage within the fault damage zone is forced towards the springs with increases in barometric pressure. Specific storage is calculated from barometric efficiency based on a range of porosity values. The higher than expected range, 1×10^{-6} to 1.5×10^{-5} m^{-1} (porosity from 10 to 30%) for springs sourced predominantly from a limestone aquifer, may be due to the overlaying sandstone aquifers, assumptions in the equation used, the semi-confined nature of the aquifer, and the location of the spring, close to the Nacimiento fault. Spectral analysis of near-synchronous spring depth variations have power at peaks with

a period of 12 and 24 hours, which coincide with solid Earth tides of S_1 and S_2. These occur in all springs, but the relative power of each spectral peak varies within each spring, and between springs, decreasing across the springs from north to south, higher to lower elevation. Atmospheric tides cause barometric pressure cycles with similar periods of 24 and 12 hours, and distinguishing between the spectral power due to Earth tides and barometric pressure is not possible with existing data. The spatial variations in spectral power may be due to an Earth tide component with the data, which varies from north to south. This is the first time these methods have been applied to a series of fault-co-located artesian springs and provide a first attempt to use such a spring network to investigate aquifer properties.

Introduction

Investigation of subsurface properties is one of the major purposes of field studies in hydrogeology, with applications ranging from groundwater management to hydraulic fracturing relying on accurate, in situ estimates of aquifer properties. Faulting provides further complexity to subsurface investigations, and despite its importance in permeability and fluid flow in aquifers, hydrocarbon migration, CO_2 sequestration, and storage of nuclear waste, the specific role faulting plays is often not well understood (Bense et al., 2013) even though characterizing fracture and fault networks and connectivity between springs (or wells) is a required step to identify contaminant transport pathways or recharge processes (Burbey and Zhang, 2010). The dominant

method for determination of in-situ aquifer properties is the analysis of pumping tests (e.g., Theis, 1935; Jacob, 1940), where data collection is primarily from wells. An alternative method is continuous monitoring of spring parameters, and in particular, the analysis of the response to variations in natural loading phenomena, such as barometric pressure and Earth tides. This is a cost effective method for investigating the subsurface, whilst also gaining an understanding of the hydrology of the spring system.

Spring head (depth) variations are sensitive to numerous factors such as precipitation, recharge, regional flow and pumping, barometric pressure, Earth tides and seismic events; these phenomena induce enough stress to deform aquifer structure to the extent that pore pressure is altered, which is manifest as variations in water/head level. Several methods have been developed that focus on the loading response from barometric pressure and Earth tides that allow the analysis of water level to provide information about in-situ aquifer parameters (Bredehoeft, 1967; Hsieh et al., 1987; Narasimhan et al, 1984; Rasmussen, et al., 1997). These methods have also been used to evaluate the success of hydrofracing to increase (water) well production (Burbey and Zhang, 2010), for fault and fracture characterization (Burbey, 2009) and to highlight changes in groundwater systems after seismic events (Zhang et al, 2019).

Whereas most hydrogeologic studies analyze well data to investigate aquifer properties, the use of spring hydrographs has seen less examination. Here we use data from a series of artesian springs aligned along the Nacimiento fault in New Mexico to

investigate aquifer properties and study fluid movement within the fault zone. Figure 1 shows the broader study area with regional Quaternary faulting. This location is unique

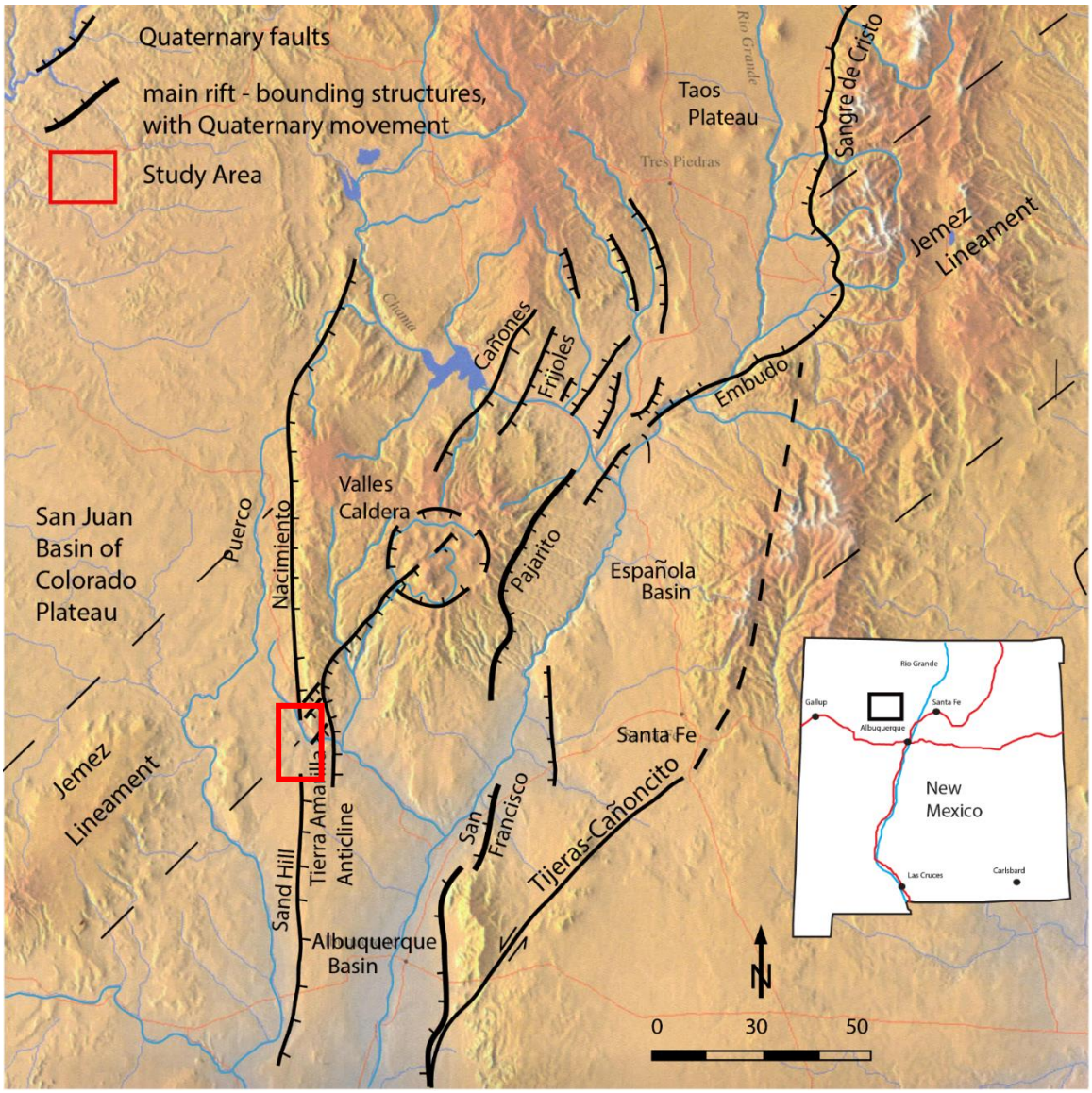

Figure 1 – DEM of the regional study area showing major structural features, San Juan Basin of the Colorado Plateau, Jemez Lineament, Valles Caldera. Inset state map.

as there are a series of artesian springs (four springs across ~1.5km length of the fault), which act analogously to a closely spaced well network and provide information on hydraulic head, response to natural loading and are areas of increased of permeability within the fault zone. Figure 2a shows the location of the springs in the study area, and 2b is a geology map with cross section lines in red. This paper uses techniques

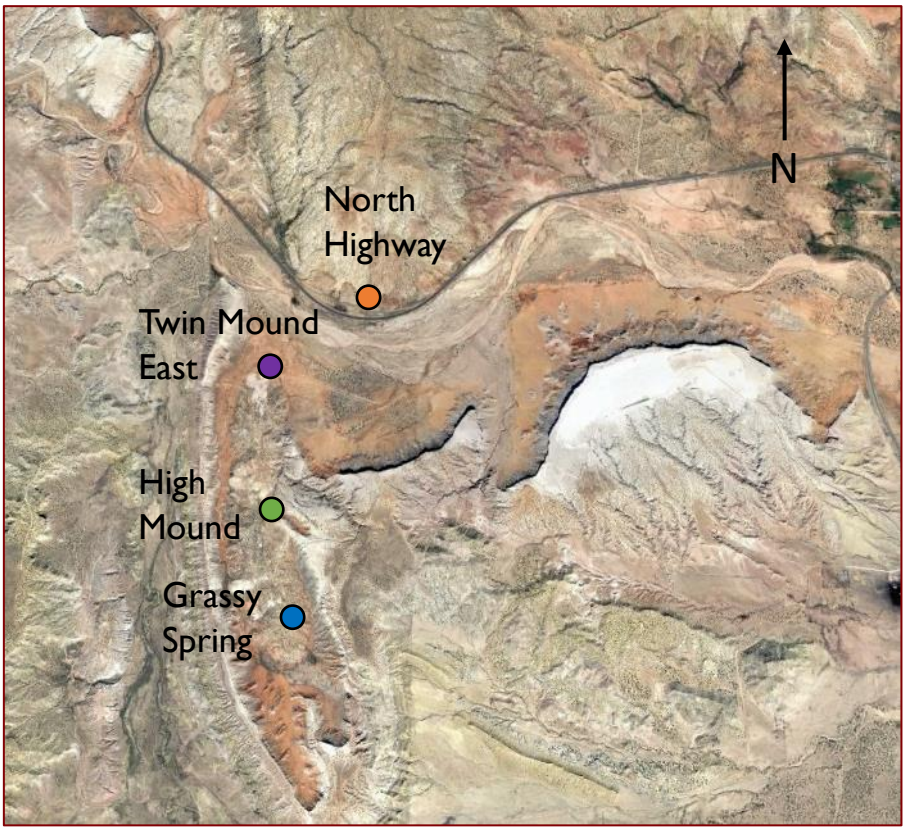

Figure 2a – Locations of springs and monitoring sites. Springs are located on or slightly off axis of the fault, and travertine occurs at all spring locations.

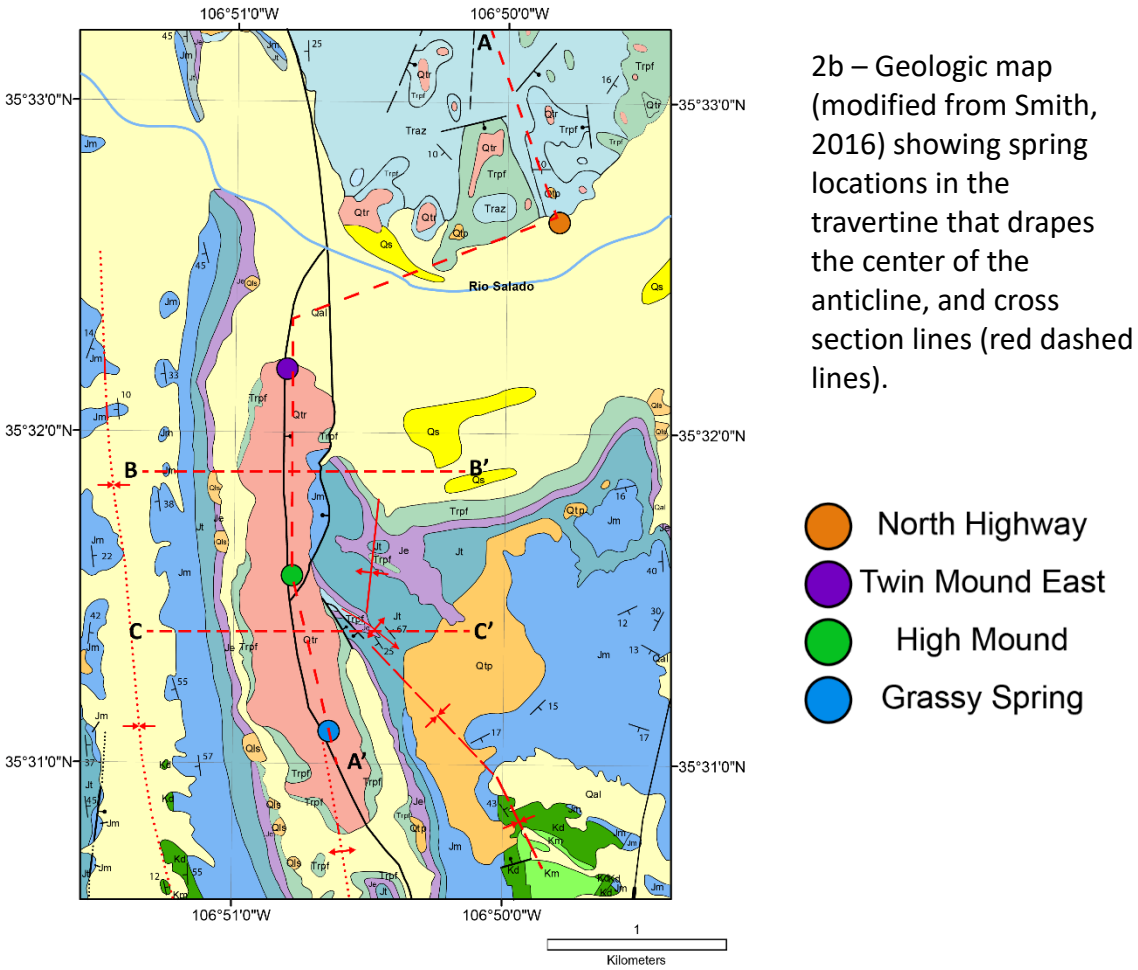

2b – Geologic map (modified from Smith, 2016) showing spring locations in the travertine that drapes the center of the anticline, and cross section lines (red dashed lines).

previously published to examine well data, but applies them to a series of springs to provide new insight on fault controlled spring hydrology, in particular, investigate aquifer properties (specific storage) and provide evidence for along fault fluid flow.

Long term baseline monitoring is a vital start point in understanding regional hydrogeology, and monitoring environmental change through time. This data set provides a unique opportunity to investigate multiple springs that discharge from within the fault zone, where variations in the response to loading can be compared to provide information about the individual spring and hydrostratagrphic continuity between the

spring system. Furthermore, it indicates a unique response to barometric pressure, where fluid movement within the fault zone migrates towards the springs, with increases in barometric pressure. Faulting has a demonstrable effect on spring discharge and permeability (Levens et al., 1994; Mayer et al., 2007; Bense et al., 2008; Burbey, 2009), and this work shows how the traditional view of how barometric pressure effects well water level may be misinterpreted if data is taken from a spring or well within a fault zone.

Previous research

The assessment of aquifer properties from analysis of water level fluctuations due to periodic variations, such as barometric pressure and Earth tides, provide a feasible and economical tool for improving information about aquifer parameters (Fuentes-Arreazola et al., 2018). In applied settings, the desire to understand the effects of loading is simply to remove them from the data, to provide more accurate readings, such as when taking depth to water measurements for piezometric maps, or during pumping tests (Fileccia, 2011, Toll and Rasmussen, 2007). However, this knowledge has greater utility. It has been used to estimate specific storage and porosity, such as in the Floridan Aquifer, Florida, where calculated results were comparable to pumping tests and measurements from core samples (Merritt, 2004). Acworth et al., (2016), used atmospheric tides at a frequency of 2 cycles/day as a tracer to examine how BE and specific storage vary with depth. Using piezometers screened at depths between 5 and 55m, they created a BE depth profile, and showed how phase difference between

hydraulic head and barometric pressure can be used to determine spatiotemporal changes in confinement, associated with drying and cracking of smectite clay-dominated sediments. Burbey, (2009) used well response to Earth tides to quantify the specific storage and secondary porosity in a fault zone aquifer, while Shen et al., (2020), compared hydraulic conductivity from pumping tests with that inferred from tidal response in a coalfield perched aquifer and found that the range of tidal response values was close/similar the pumping test values. Burbey and Zhang, (2010) used Earth tides and Barometric response to assess hydrofracing success in wells, and showed how, post-fracing, wells had almost identical responses to loading, indicating hydrologic connection.

Analysis of time series hydrographs improves understanding of hydrology and water quality, and can lead to more effective resource management. Hydrographs are able to capture seasonal, diel and event driven fluctuations, and can be used to optimize sample collection periods. Though far more attention is paid to water supply problems associated with water quantity, water quality is in increasingly important issue (Phillips et al., 2003). Time series data provides a baseline against which future variations can be compared, allows signal analysis to establish controlling factors within the data, and enable more accurate construction of management practices. Additionally, variations discovered through continuous monitoring can inform understanding of hydrologic drivers. This catalogue of uses serves to illustrate the significance of autonomous sensors in studying longer-term change in hydrological systems, and its utility.

Faulting and fluid flow

The permeability of aquifer material has been measured for over a century, but values for fault rock permeability are less common and more difficult to measure (Ran et al., 2014). Understanding fluid flow around fault zones in different geological environments it is often not well understood (Bense et al., 2013) with fault permeability depending on host rock type and deformation history (Heffner and Fairley, 2006). Figure 3 is a schematic diagram showing the fault zone, which is composed of a fault core, where most of the displacement takes place, a damage zone, a network of fractures that bound the core, usually with increased permeability, and the Protolith (Caine et al., 1996).

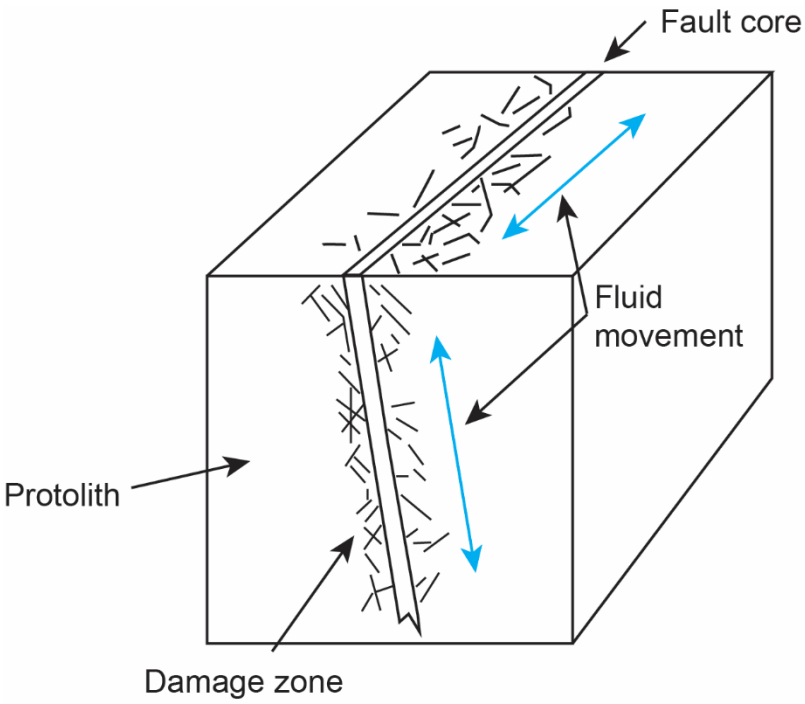

Figure 3 – Fault permeability model showing fault core, damage zone and host rock/protolith. The damage zone is considered to be the location of highest permeability within the fault zone hydrologic system, and fluid movement occurs here.

The structures related to the damage zone include fractures, veins, cleavage, folds and small faults, which result in heterogeneous and anisotropic permeability structure of the damage zone (Caine et al. 1996). The variability in permeability of fault architecture, leads to fault zones acting as conduits, barriers or duel systems (Caine et al., 1996), however the extent to which this occurs is controlled by rock type, deformation history and mineralization/cementation within the fault zone (Bense and Person, 2006; Lockner et al., 2000).

The analysis of fault zone hydrology is carried out using multiple methods (Bense et al., 2013). At the local scale, direct fault analysis through outcrop mapping of fault attributes such as fracture characteristics, fault rock grain size, porosity, permeability and CO2 flux measurements help establish fault core and damage zone size and permeability (Smith, 2016; other refs needed). Subsurface studies infer hydrogeologic behavior from well or spring networks, which provide information on hydraulic head/groundwater levels, and can show step or inflections in hydraulic gradient, which can provide information about fluid movement around the fault zone (Anderson and Bakker, 2008; Bense et al., 2003). Outside of developed areas, where outcrops for study are rare, fault zone analyses are often on a more regional scale, but can be combined with geochemical, temperature and CO_2 flux data to help constrain flow paths across, or along fault zones (Bense et al, 2008, Smith, 2016).

Water level response to loading

Groundwater hydrology attempts to estimate values for aquifer properties, variables that are able to quantify water transmitting and storage properties. Estimates are based on measuring a change in the pressure field of groundwater caused by the application of mechanical stresses, which change the rate of water movement and release from storage. One such stress is through an aquifer test, where water is quickly added or removed from a well, and the resulting variations in water level over time provide estimates of aquifer properties, e.g. permeability and storativity. Many subsurface mechanical stresses have naturally occurring causes rather than anthropogenic ones, such as the mechanical forcing of an aquifer by ocean and earth tides, and pressure variations in the atmosphere. Investigation of aquifer properties using water-level fluctuations caused by natural processes represents an easily available and cost reducing alternative to well pumping. (Merritt 2004).

Water level response to barometric pressure

Pressure loading and unloading caused by changes in the weight of the atmosphere is a source of natural stresses acting on subsurface formations. The changes are due to periodic, diurnal and semidiurnal, variations in atmospheric pressure, and to aperiodic, longer-term movements of masses of air of higher and lower pressure across the surface of the earth. A change in atmospheric pressure leads to a change in aquifer pore pressure, to accommodate this change, water in a well tapping the aquifer or a spring sourced from the aquifer, varies by an amount proportional to this pressure change. (Merritt, 2004; Rhoads and Robinson, 1979).

The extent of response is a function of the properties of the aquifer, confining layer, and in the case of wells, borehole design. These fluctuations were first reported in the 17th century by Blaise Pascal. Since then, refinements in methods have attempted to isolate the variations due to barometric pressure from other factors, such as recharge or Earth tides (Butler et al., 2011; Rasmussen et al., 1997; Rojstaczer 1989; Toll et al., 2007; Weeks, 1979). Water levels from entirely confined aquifers fluctuate in response to barometric pressure changes, while entirely unconfined aquifers have no response. Entirely confined and unconfined aquifers represent end members and most aquifers fall on a spectrum in between, being semi-confined with a confining unit that is not entirely impermeable, or semi-unconfined, where the unsaturated zone is thick or has low permeability (Hussein et al., 2013).

In purely confined aquifers, where confining layer has zero permeability, changes in barometric pressure are transmitted to the aquifer instantaneously and are distributed between the aquifer skeleton and pore water (Batu, 1998; Spane, 2002). Springs, or wells that are open to the atmosphere, experience this pressure loading in its entirety, and it is this difference that leads to a pressure imbalance, where an increase in barometric pressure leads to a decrease in water level, and vice versa. For a perfectly confined aquafer, this ratio in change of barometric pressure to water level is constant, and the relationship can be characterized by the static barometric efficiency (BE) [Jacob, 1940]:

$BE = \Upsilon \Delta W / \Delta B$ where

BE = Barometric efficiency

ϒ = Specific weight of water

ΔW = Change in hydraulic head

ΔB = Change in atmospheric pressure (meters of water)

A BE of one is a perfectly confined aquifer, while a BE of zero, is entirely unconfined. While most values fall in between, values outside of these boundaries indicate other process are affecting water depth simultaneously, such as Earth tides, recharge or pumping from a nearby well.

However, in semi-confined/unconfined aquifers, this relationship is a function of barometric pressure frequency. Here, a constant barometric efficiency is inadequate to describe the response, and a barometric response function is required to represent this frequency dependent relationship.

Barometric response function

The BE calculated by Jacob (1940), was used originally in confined aquifers, where the air pressure wave travels fast, BE values refer to short term changes (1 to 2 hours), and do not vary with time. When other influences are present, Earth tides, recharge, fault zones, static BE values may be inaccurate and vary with time, and the barometric response function (BRF) was introduced as a way to characterize the longer-term response (Rasmussen et al, 1997; Spane, 2002). The BRF estimates the time-lag response between barometric pressure changes and water level changes. Being able to trace the BE as a function of time helps identify if the initial BE is different from the final, and can be used to identify aquifer type, level of confinement, and skin effects in wells.

Diagnostic plots are used to identify these different phenomenon. These plots consider the sole control on the water level change to be barometric pressure, whereas in reality, other factors such as recharge, evapotranspiration, Earth tides, and in wells pumping, need to be considered, identified, and where possible removed.

Water level response to Earth tides

The motion of the sun and moon that leads to ocean tides, also causes dilatation, and expansion and contraction of aquifer rock matrix/skeleton. These effects are referred to as Earth tides and occur because of gravitational and centrifugal accelerations occurring at a point on the surface of the Earth, due to the movements of planetary bodies (Burbey, 2009; Merritt, 2004). As the aquifer skeleton dilates, pore water pressure is altered, leading to a change in the head of water in a well or spring. These water level oscillations are cyclic, coincide with known Earth tidal constituents, and can be compared with theoretical tidal potential (Agnew, 2005; Merritt 2004). Each tidal component will have a different affect depending on the relative location of the planetary body; the moon exerts a different force vector on the horizon, than when overhead. This is further complicated if faults or fractures are present, as a normal force will have a larger effect on apertures than a tangential force, and the orientation of the feature (fault or fracture) will also lead to different affects depending on the location of planetary body (Agnew, 2005). The Earth tide harmonic components are expressed as sinusoidal functions of given amplitude and frequency; however, the amplitude and phase relations for each component are controlled by the location on the Earth,

latitude, longitude and elevation (Melchior, 1983; Godin, 1972). The results of this are that, of the tidal harmonic components, five are responsible for 95% of tidal potential (Galloway and Rojstaczer 1988). Although Earth tidal responses are rarely reported in well data, they are often not the main reason for the well monitoring, in China, about 80 % of the water level in wells show earth tidal effects (Yan et al. 2014).

Study area

The springs are situated along the Nacimiento fault, in north-central New Mexico, approximately 50 km north-north-east of Albuquerque and 40 km south-east of the proximal Valles Caldera. This area is at the nexus of the Rio Grande rift, the San Juan basin of the Colorado Plateau, the southern extent of the Rocky Mountains and the Jemez Lineament (Fig 1). The springs and geology are described in detail in McGibbon et al., (2018) and references therein, but in brief, monitored springs are situated over a 1.5 Km stretch of the north-south trending Nacimiento fault, a Laramide thrust fault that has been reactivated as a normal fault during extension of the Rio Grande rift. Springs occur predominantly on axis of the fault zone, but off axis springs and seeps occur, often on perpendicular cross cutting faults, but were not monitored as part of the study. The monitored springs form pools whose depth ranges from ~0.2 m to up to ~8 m within travertine mounds and cisterns, where some overflow, forming small rivulets. Figure 4 shows a series of photographs of the springs in the study. The sizes of the spring orifices vary along their long axis from ~0.1 m to ~10 m. U-series age geochronology shows that

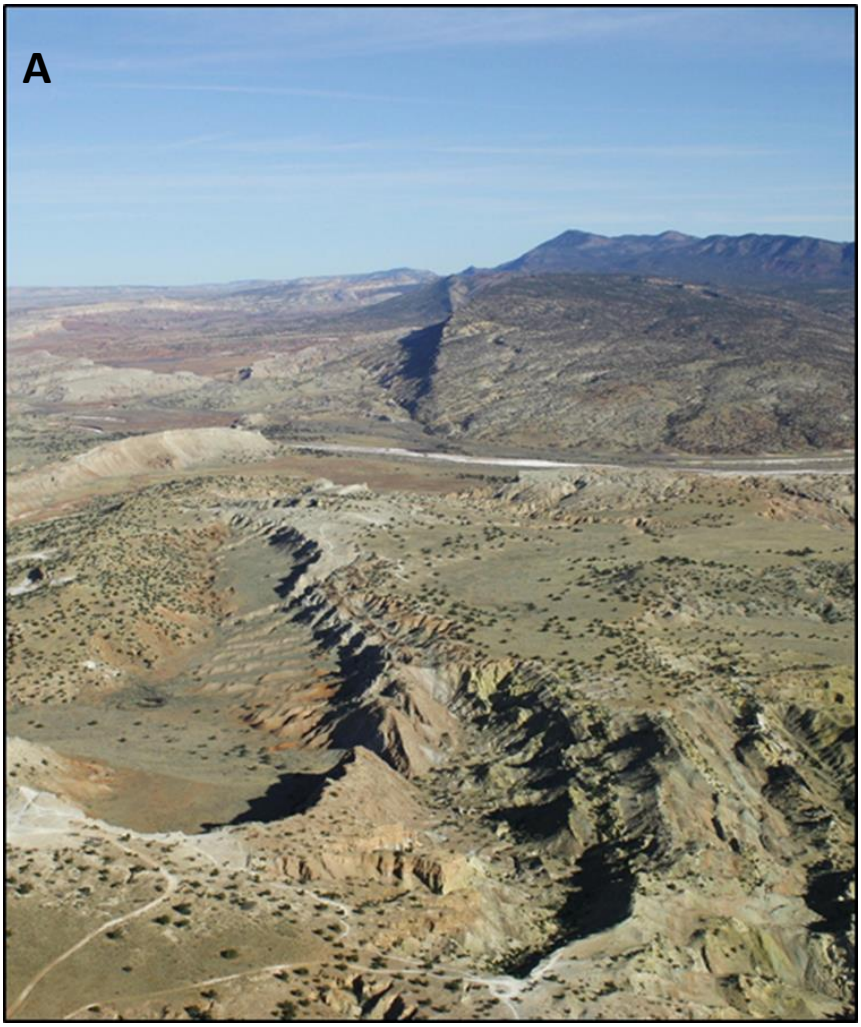

Figures 4a and b. Photos showing A. Aerial photograph looking north along the Nacimiento fault, and the eastern limb of the anticline. B. travertine mound spring

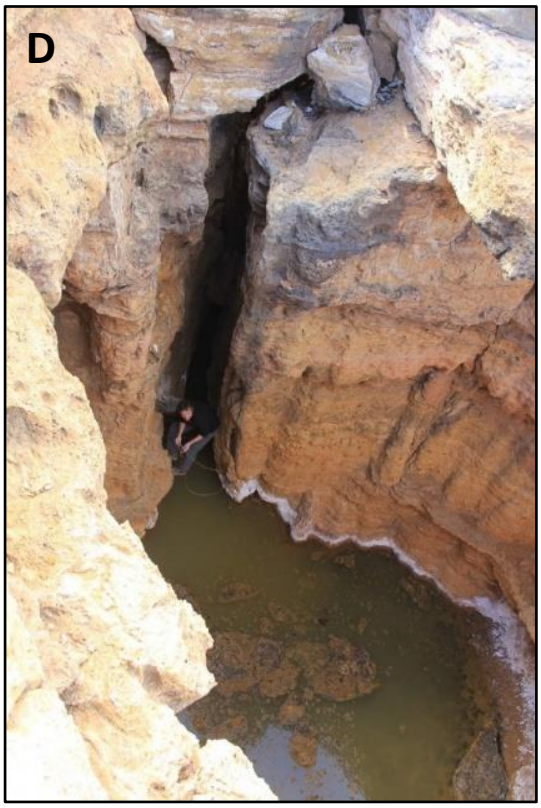

Figure 4c,d and e. C. overflowing spring forming pools and rivulets which escape down the side of the travertine mound. D. collapsed cistern spring.
E and F. North Highway showing different depths, E - maximum depth (~0.55 m), over flowing and F - drained, minimum depth (~0.2 m)

springs have been active intermittently from before 270 ka, at highest elevations, to modern actively forming mounds (Cron, 2011). Springs are artesian, forming up to 100m higher elevation than the proximal Rio Salado, saline, 12,000 to 16,000 µS, warm, ~20 ^{o}C, and degas CO_2. The elevation and co-alignment along the fault indicate a confined or semi-confined aquifer and suggests fluid movement within the fault zone. The hydrostratigraphy include the Madera Group limestone, a fractured carbonate aquifer which is believed to be the dominate source aquifer for the springs (McGibbon et al., 2018). Above this the Abo and Yeso formations act as a confining layer (Crouch, 1994) between the Madera and the San Andres-Glorieta aquifers, and the Chinle shale is the confining unit above the Agua Zarca aquifer, and below the Nacimiento fault springs. Together, these from a confined to semi-confined stacked sedimentary aquifer. Figure 5a is a simplified stratigraphic column, and 5b a simplified cross section from north to south with cross section line A – A' shown in figure 2b. Figure 5c and d are detailed cross sections perpendicular to the fault, with cross section lines B – B' and C – C' shown in figure 2b. Based on CO_2 flux measurements (Smith, 2016), a damage zone of 169 m has been proposed (approximately 98 m on the western footwall, and 72 m on the eastern hanging wall) for the Nacimiento fault in the area of the springs. The amount and location of small springs and seeps, and extent of travertine formation indicate this is a reasonable estimation. Electrical resistivity imaging propose circular conductive features on either side of, and perpendicular to the fault (Halihan et al., 2011), and suggest

mixing of water with different sources/salinities that may be associated with areas of differing permeability.

A

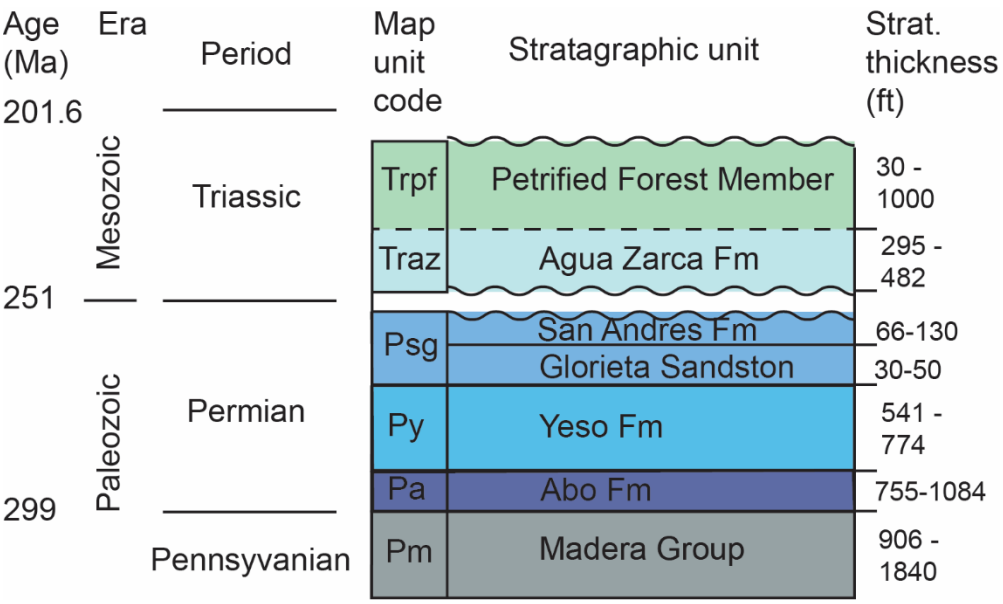

B

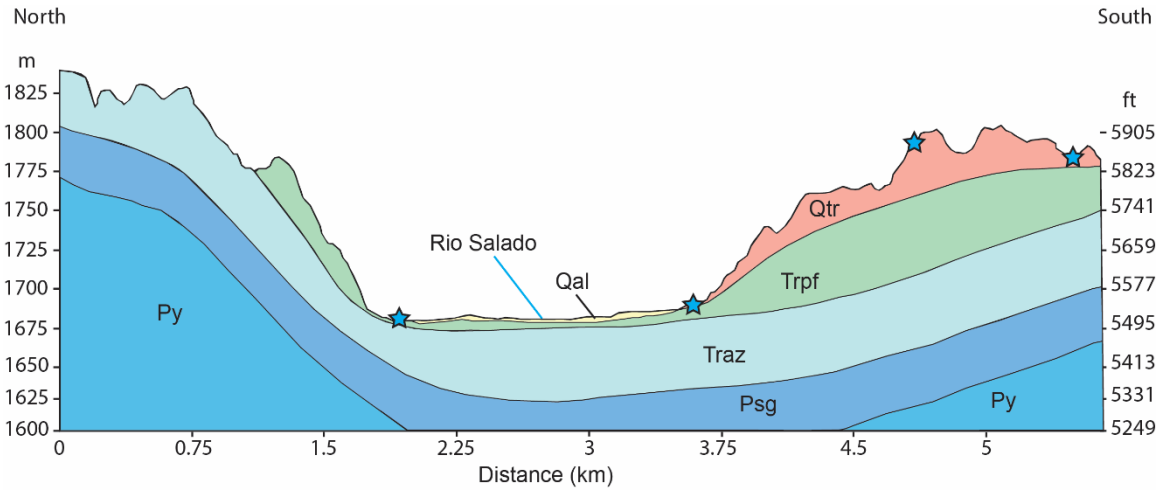

Figure 5a Simplified stratigraphic column (modified from Connell 2011) and 5b cross section, line A – A' in figure 2b, showing spring locations.

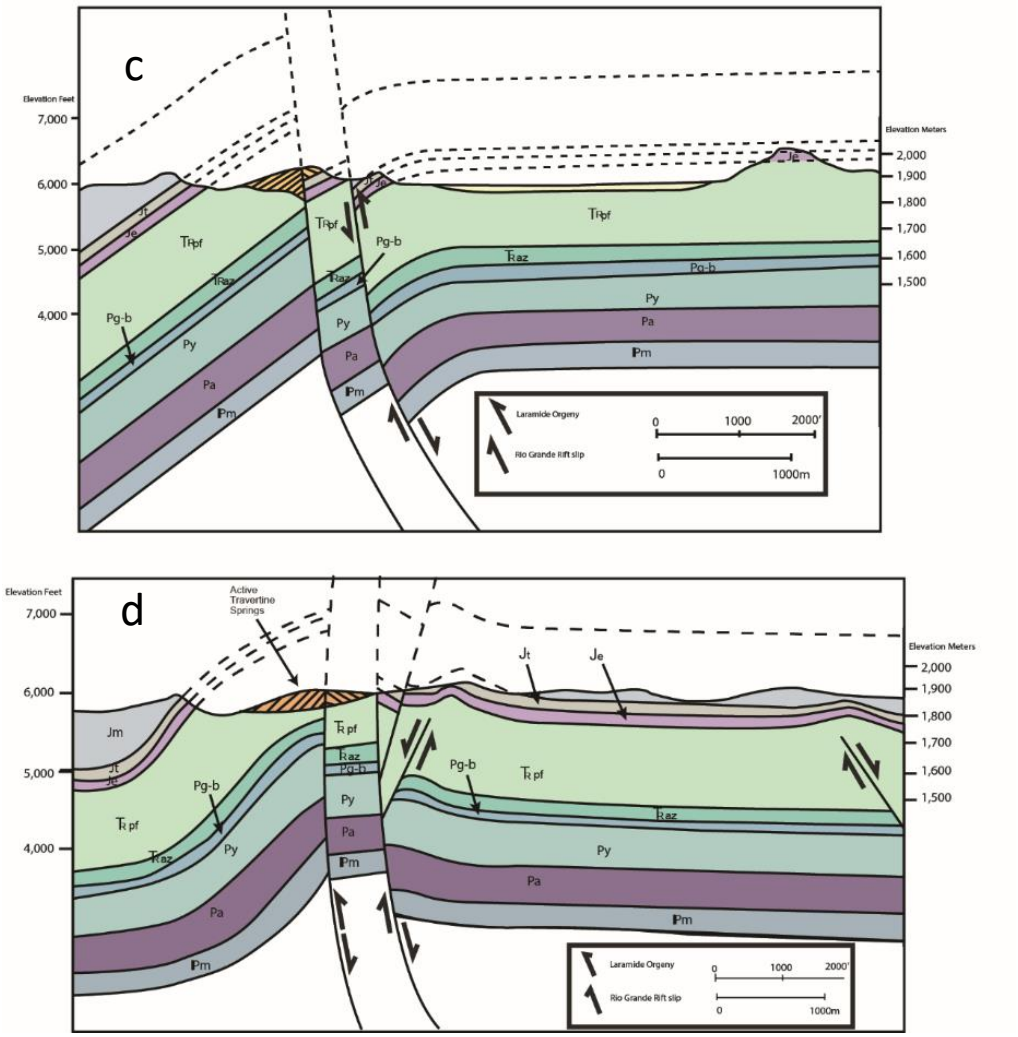

Alluvium
Clay, silt, sand, and gravel, mostly along valleys, includes minor colluvium (30 feet thick).

Sand dunes
Mostly fine-grained, windblown sand, dunes are mostly stabilized with partial cover of vegetation (10 feet thick)

Travertine
Light tan, thin to thick bedded (50 feet thick)

Morrison Formation
Four members sandstone and mudstone members: (total thickness 920 feet)

Todilto Formation
Basal brown, laminated limestone 4 to 5 foot thick, overlain by white gypsum about 100 foot thick.

Entrada Sandstone
Light orange-tan, white, and pale-yellow, fine to medium grained massively bedded sandstone (100-120 feet thick)

Petrified Forest Member
Reddish-orage and brownish-maroon shale with subordinate reddish sandstone and minor green shale, brown clastic limestone, and small pebble conglomerate (1,000 feet thick).

Agua Zarca Sandstone Member
White to buff or locally deep-red, very think bedded, medium to very coarse grained, quartzrose sandstone, grit, and conglomeratic sandstone (150-250 feet thick).

Glorieta Sandstone and Bernal Formation undivided
Bernal formation (upper): reddish-brown, very fine to medium-grained, thin-bedded sandstone (15-60 foot thick). Glorieta Sandstone (lower): white to tan, fine to coarse-grained, thick-bedded sandstone (85-100 feet thick)

Figure 5c, d Detailed cross sections perpendicular to the fault plane (Cron, 2011). Cross section lines B – B' and C – C' in figure 2b.

Methods

Multi-parameter hydrologic sensors were deployed in four springs (Fig 2a, b) and one barometric pressure sensor was installed in a shaded area, close to High Mound spring. The sensors were installed for 2 years and six months (December 2012 to May 2015). The parameters monitored were pressure (as a proxy for water depth/head), temperature and conductivity. The sensors were Solinst Levelogger Junior Model 3001 LTC. The sensor utilizes piezoresistive silicon with Hastelloy pressure sensor, platinum resistive temperature detector and 4-electrode platinum conductivity sensor. Calibration is not required for temperature and pressure as these come with lifetime factory calibration, but are required regularly for conductivity. Calibration was carried out using a 3-point calibration with conductivity solutions of 1,314 (µS), 5,000 µS and 12,880 µS. For Barometric corrections, a Solinst Levelogger Edge was used to record air temperature and atmospheric pressure. Resolution was initially set at 15 minutes intervals, increased to 5 minutes after 2 months, then reduced back to 15 mins after a further 1 year and 10 months. Sensors were deployed attached to wire cables and suspended in the pool formed by the springs. Depth of deployment was controlled by the depth of the pool, with the sensor suspended as deep as possible without being affected by sediment from the base of the spring. Data were downloaded in the field using a laptop and infra-red sensor USB connector. Corrections were made to delete anomalous readings, such as, sensors being removed for recalibration/download, anthropogenic interference and to make depth corrections for barometric pressure and

elevation. Management and analysis of continuous monitoring water data was carried out using Excel, Aquarius Time Series software and Matlab.

Data analysis focused primarily on water depth and is split into the analyses of Earth tides, and response to barometric pressure changes. For Earth tide analysis a domain shift was carried out using the fast Fourier transform. This is an algorithm for computing the Discrete Fourier Transform, a process which decomposes a series of values into components of different frequencies. These frequencies can then be compared with known Earth tide values/frequencies. Prior to the analysis, data were filtered to remove frequencies above and below 30 and 10 hours respectively to remove the effects of high and low frequency data.

To analyze the response to changes in barometric pressure, the barometric response function was calculated using the Kansas Geological Survey Barometric Response Function software (Bohling et al, 2011). This program uses regression deconvolution methods from Furbish (1991) and Rasmussen and Crawford (1997) and calculates how the barometric efficiency changes through time. The input variables are the depth time series data, barometric pressure, time step, length of BRF analysis (in this instance 150 time steps, which is equal to ~12 hours) and optionally Earth tide data. The use of synthetic Earth tide data, in this case generated from Tsoft (Van Camp et al, 2005), allows the effects of Earth tides to be removed prior to BRF analysis. Time periods for analysis were selected based periods when seasonal variations, if any, were minimal, and there were no step changes in the data. After a series of trial an error, a period of ~4 weeks was selected for the BRF analysis (Table 1). This was chosen as it

Spring	BRF dates			
	1	2	3	4
North Highway	4/8 - 4/30/13	8/1 - 8/31/13	9/5 - 10/5/14	3/1 - 3/31/14
Twin Mound East	3/2 - 4/2/13	5/10 - 6/10/13	10/1 - 11/1/13	4/1 - 5/1/14
High Mound	3/1 - 4/1/13	5/10 - 6/10/13	3/25 - 4/25/14	11/1 - 12/13/14
Grassey Spring	3/10 - 4/10/13	5/10 - 6/10/13	2/10 - 3/10/14	10/1 - 11/1/14

Table 1. Dates for barometric response function calculation

represented the maximum length of time that could be used repeatably across the time series where there was minimal disruption. Longer time periods were examined, but there was little variation in the BRF output, outside of seasonal and time step effects. The output variable includes the spring depth corrected with barometric efficiency, and the barometric response function, which consists of the barometric efficiency per time step (set 150 above) and time lag. When plotted together, these last two variables show how the barometric efficiency changes through time, in this instance, up to twelve hours.

Results

Full time series data for each parameter can be seen in figures 6 – 8 (by spring in Figs S1-3). Each set of monitoring data will be examined by parameter, focusing on the springs that show the greatest and least variation.

Depth values (Fig 6) are read from the location of the sensor, zero, to the water surface and are considered relative depth variations, and from here on will be referred to as depth. All springs have depth variations in excess of 0.1 m with North Highway

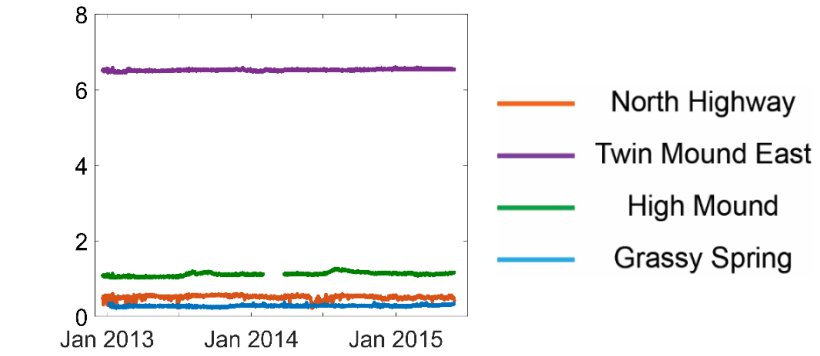

Figure 6. –

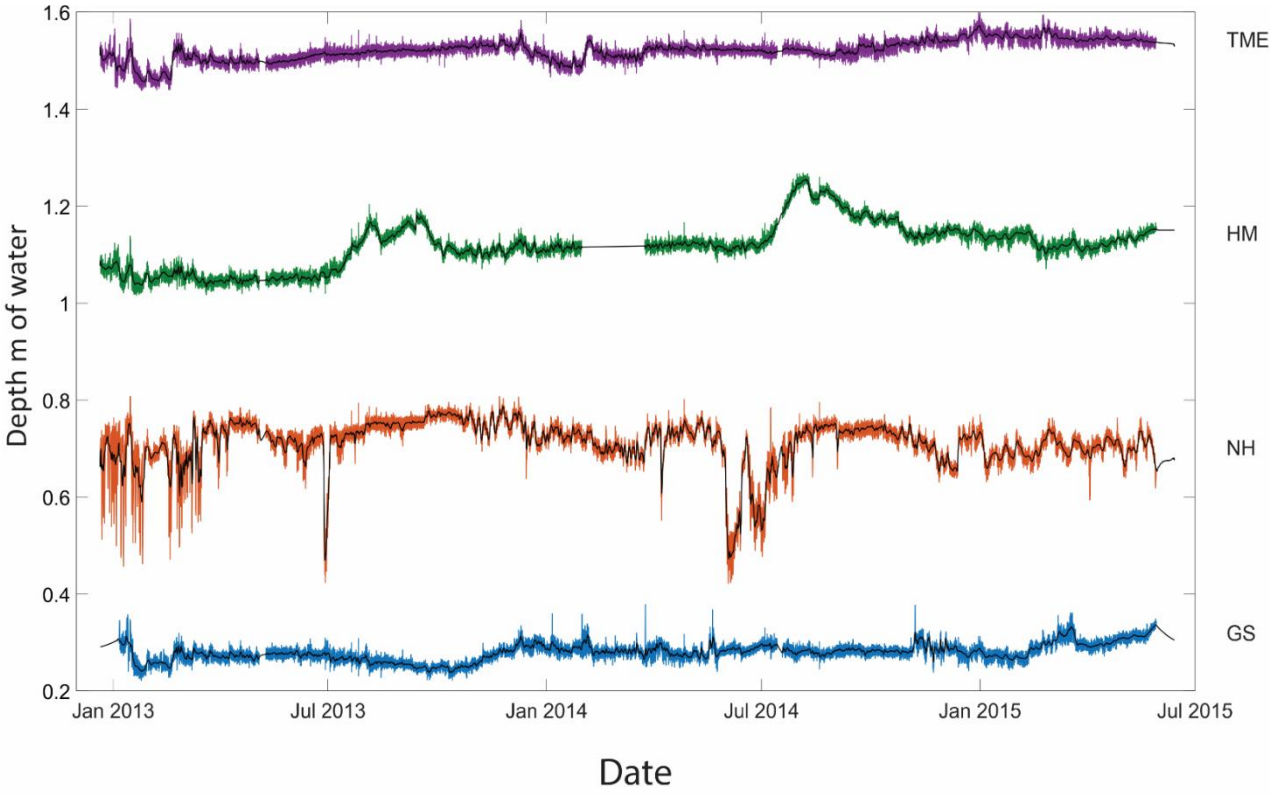

Figure 6 – Spring depth. Depth values are read from the location of the sensor, zero, to the water surface, depth is offset for plotting (top fig shows real spring depth). Depth variations are distinct for each spring, with the nature of the spring, e.g. travertine mound vs collapsed cistern, spring discharge and fault connectivity all playing a role.

having the greatest variation, 0.38 m, with a maximum depth of 0.6 m, minimum depth of 0.22 m and mean of 0.51m. Sharp decreases in depth, of over 0.2 m, to less than 0.25m, for North Highway are seen in July 2013 and June 2014. Twin Mound East has the least variation in depth, 0.16 m, and depth variations show no large or sharp

variations. High mound shows gradual increases in depth from July to October for both years, and has an increase in depth across the study period. Grassy Springs has periodic spikes of varying magnitude and frequency, which occur across the data stream. Synchronous diurnal variations occur in all springs with similar variations in magnitude. These variations are seen through most of the year, however there are temporal and magnitudinal variations, with the summer months having a reduction magnitude. At North Highway this signal alters in both frequency and magnitude in relation to the other springs, and the greatest magnitudinal variation occurs here.

The greatest temperature variation (Fig 7) is in North Highway at 18.6 ^{o}C, with a maximum of 24.1 ^{o}C, a minimum of 5.5 ^{o}C and a mean of 16.2 ^{o}C. The highest, least variation and most stable temperature, is exhibited by Twin Mound East with a range of 2.8 ^{o}C, from 21.9 ^{o}C to 24.7 ^{o}C. Mean temperatures for High Mound and Grassy spring are 16.8 ^{o}C and 18.6 ^{o}C respectively. All springs show seasonal variations, up to a maximum of ~10 ^{o}C, with an increase during the summer months and a decrease in winter. Daily variations occur, ~ 1 ^{o}C in North highway, High Mound and Grassy Spring.

Specific conductance data (Fig 8) was troublesome due to persistent biofouling and instrument failure. North Highway displayed the greatest variation with a value of 9.372 mS, a maximum conductivity of 9.659 mS, minimum of 0.287 mS and mean of 7.382 mS with periodic drops in conductivity in the summer months. All the springs

exhibited sharp variations in conductivity, possibly associated with biofouling, but numerous cyclical patterns are seen in conductivity ranging from hourly to seasonally.

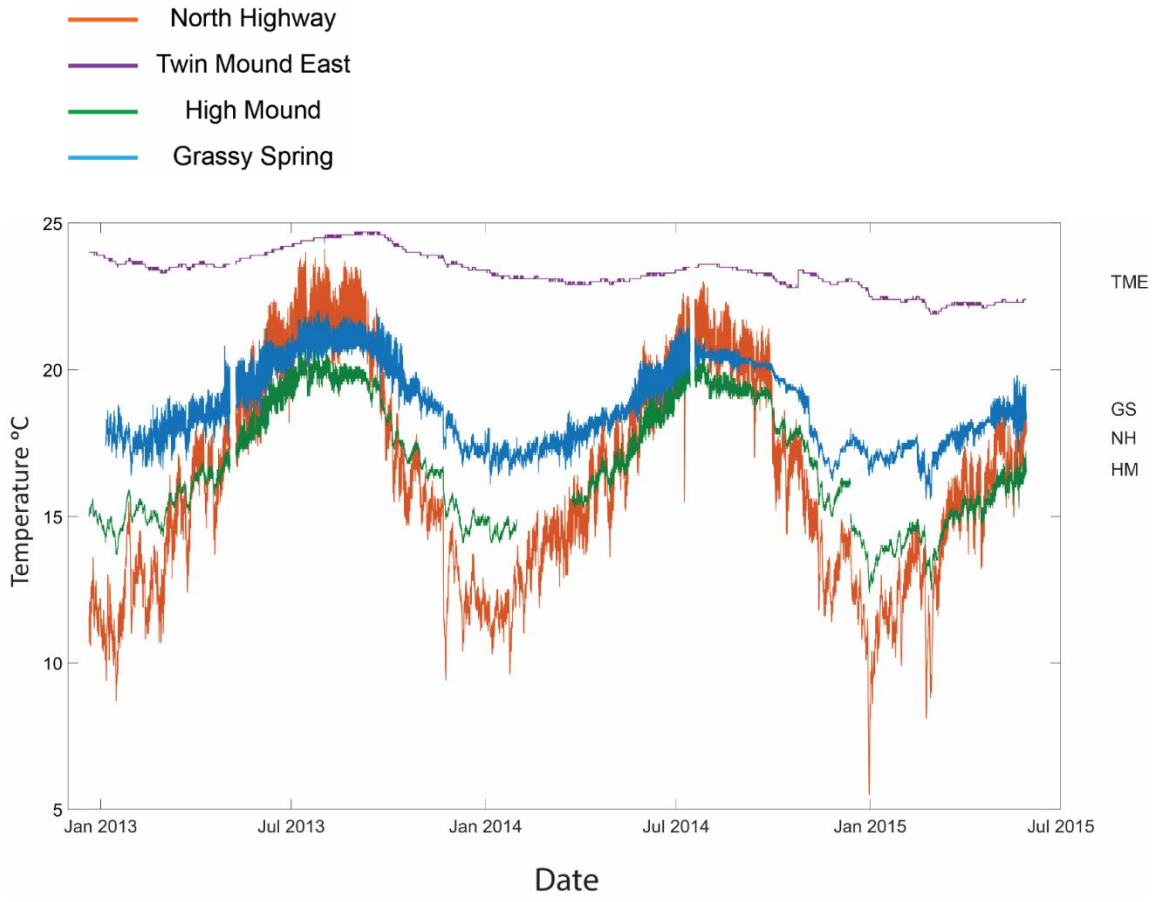

Figure 7. – Spring Temperature. Spring temperature has seasonality, with an increase in the summer. Daily variations occur at NH, HM and GS. The large volume of water (~6.5m deep) and travertine cap at TME, may dampen the daily signal.

Short time scale cyclical patterns show a sharp increase and steady decreases over several hours with a range of ~0.350 mS, but these are not present through the whole

data streams. Daily cycles occur in North Highway, High Mound and Grassy Spring. High Mound shows other sub-diurnal cycles, but these may be an artifact of the sensor, as

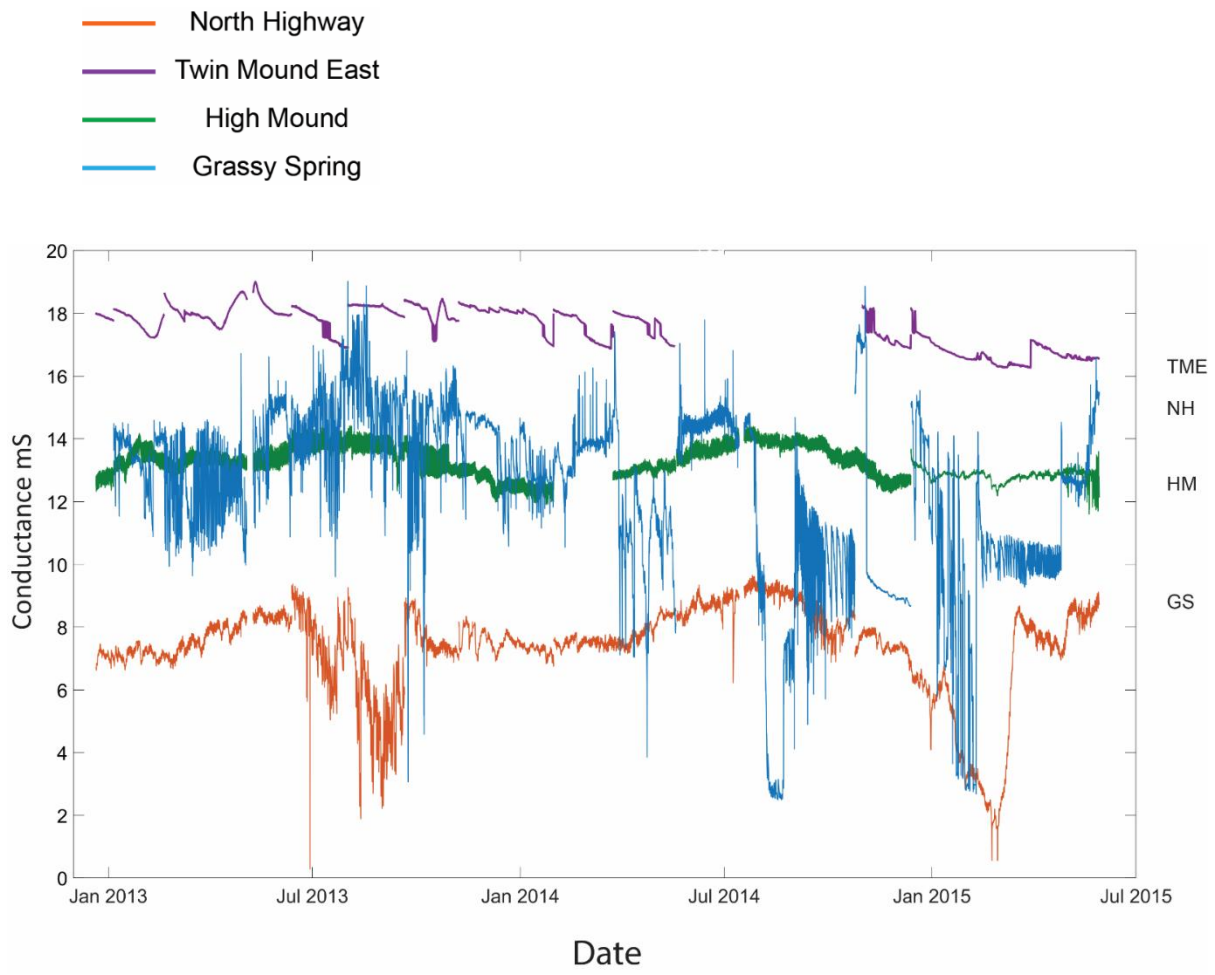

Figure 8 – Spring specific conductance. Specific conductance was problematic due to biofouling of the sensors at NH, TME and GS. HM is the least effected, and highlights seasonality, an increase in specific conductance associated with increases in temperature.

they are not present in later data after the sensor was replaced. High Mound also has increases in specific conductance through the summer months. The springs show synchronous variations between different parameters that are non-periodic, and/or

non-stationary, indicating coupling between the data. North Highway, High Mound and Grassy Springs all have variations in depth that are associated with, and potentially drive, variations in temperature or specific conductance.

Discussion

Discussion will focus on variations in depth, but will consider temperature and specific conductance where appropriate. The seasonal controlling factors on spring depth variations include spring discharge/recharge to the spring pool, precipitation, mainly monsoonal events, and spring snowmelt. On a smaller time scale, response to barometric pressure changes and Earth tides will alter depth periodically, but on a smaller scale in terms of magnitude. As described above these variations can be used to quantify aquifer parameters and will be used here to investigate fluid movement within the fault zone.

Barometric response function

The BRF for each spring is shown in figure 9a (mean values and diagnostic response plots in Fig 9b). Each spring has a similar response that varies in magnitude, but not timing. The responses are unusual to other published BRF (Butler et al, 2011; Cook et al., 2017, Rasmussen and Crawford, 1997) in that they show a two component response, an initial unconfined response (black circle in fig 9b), followed by a step

change at ~30 mins (0.04 days) leading to a positive, confined response with BE of ~ 0.2.

The long term (12 hour) confined response has a slight decrease and is typical of the

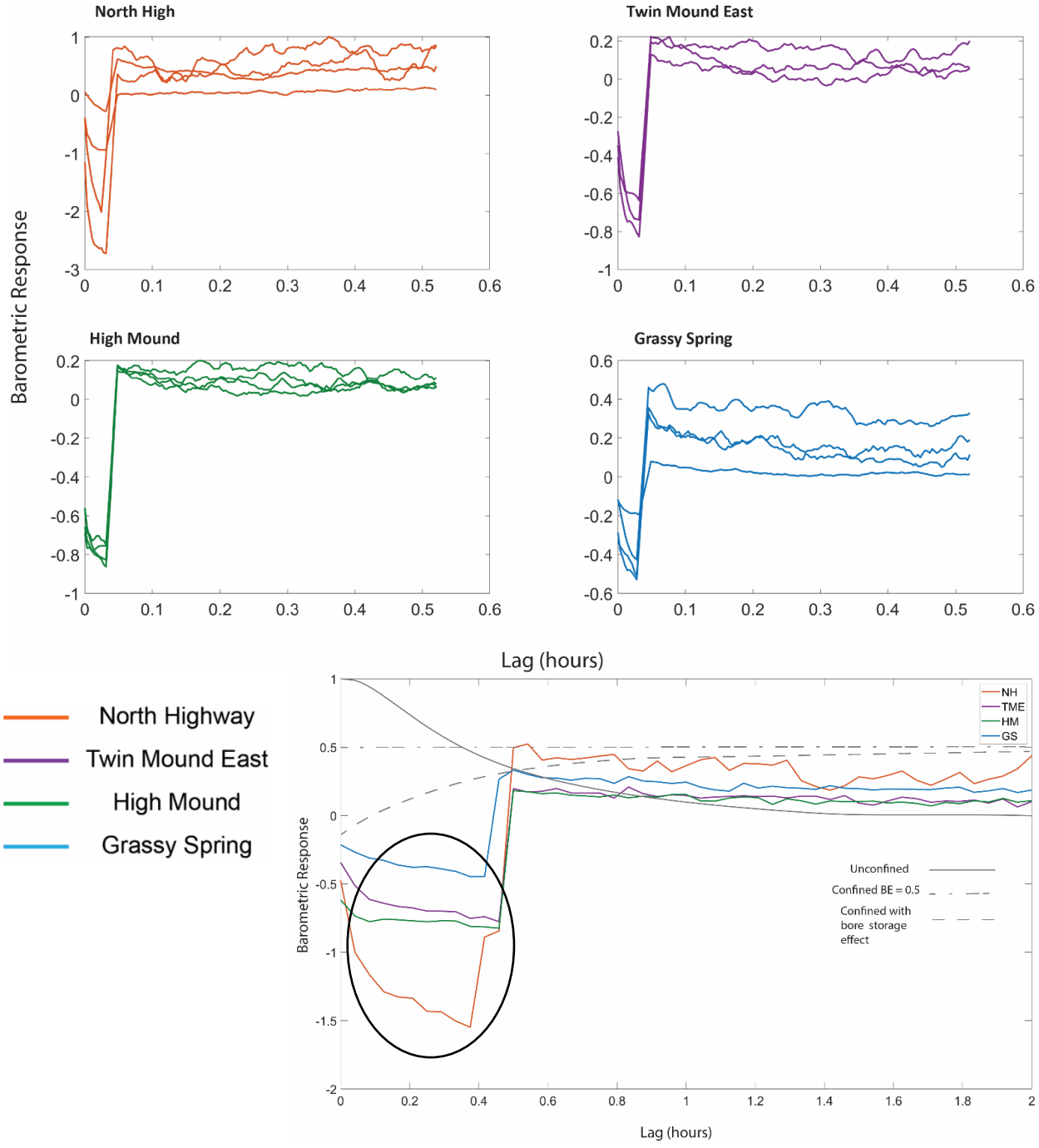

Figure 9a. – BRF. Initial lowering and negative values suggest an unconfined response and that water is moving into the spring, with an increase in barometric pressure. A confined response occurs subsequently. NH has the greatest variation, and also shows

greater variation in other physical and chemical parameters. 9b. – mean values for the BRF, with diagnostic response plots for BRF. Black circle shows the unconfined and negative response portion of the plot.

response from a semi-confined aquifer (Butler et al, 2011), where water leaking through the aquitard equilibrates head over time. During the initial unconfined response, BRF values are negative. A negative value in the BRF suggests spring depth is increasing with increases in barometric pressure, the reverse of a typical barometric pressure/water level response. Figure 10 a plots spring depth and atmospheric pressure (data offset for comparison). Synchronous increases in atmospheric pressure and spring depth occur, with almost identical variations in magnitude. These variations only occur when there is a rapid change in barometric pressure and are not seen across the entire data stream, on occasions, the opposite occurs (Fig 10b), but with a variety of factors influencing spring depth, variation in the signal is unsurprising. Figure 11 shows the spring depth that has been smoothed and reduced with a band-pass filter which removes frequencies below 2.4 (10 hours) and above 0.8 (30 hours) cycles per day and centers the data around zero, and detrended barometric pressure. North Highway spring has depth variations that coincide almost perfectly with barometric variations, while other springs have similar variation in magnitude, but a phase shift between the parameters. The phase difference for the other springs suggests other factors are influencing spring depth on a periodic time scale, similar to, but slightly offset from barometric pressure

(discussed below). These variations show agreement with the BRF negative value response that water depth is increasing due to increases in barometric pressure. For this

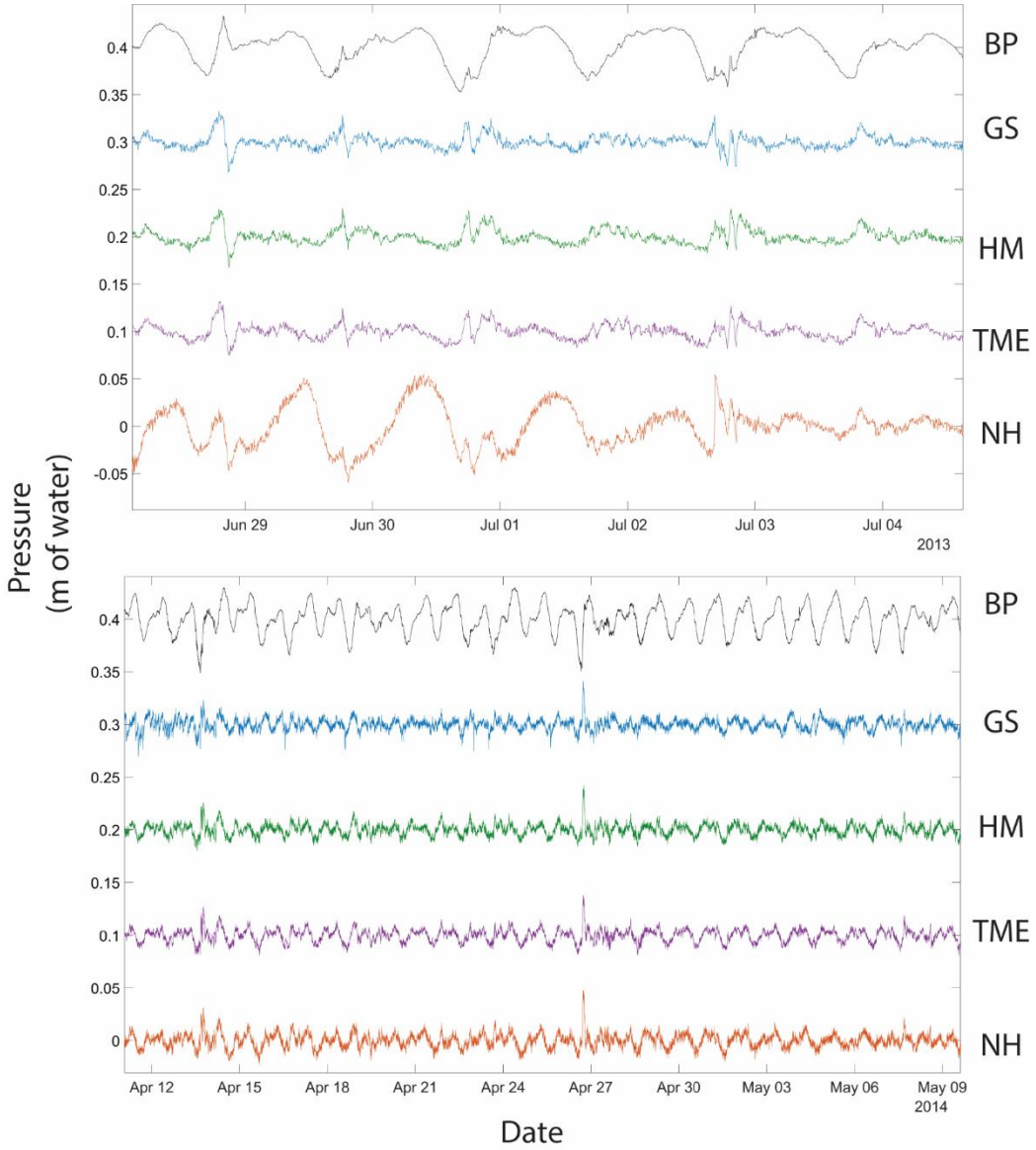

Figure 10a, b– Synchronous variations in spring depth associated with variations in BP (black line). 10a Depth and BP increases are similar/identical in timing and magnitude. 11b Variations are similar in timing, but opposite in sign, magnitude of variations vary. Data is offset for plotting.

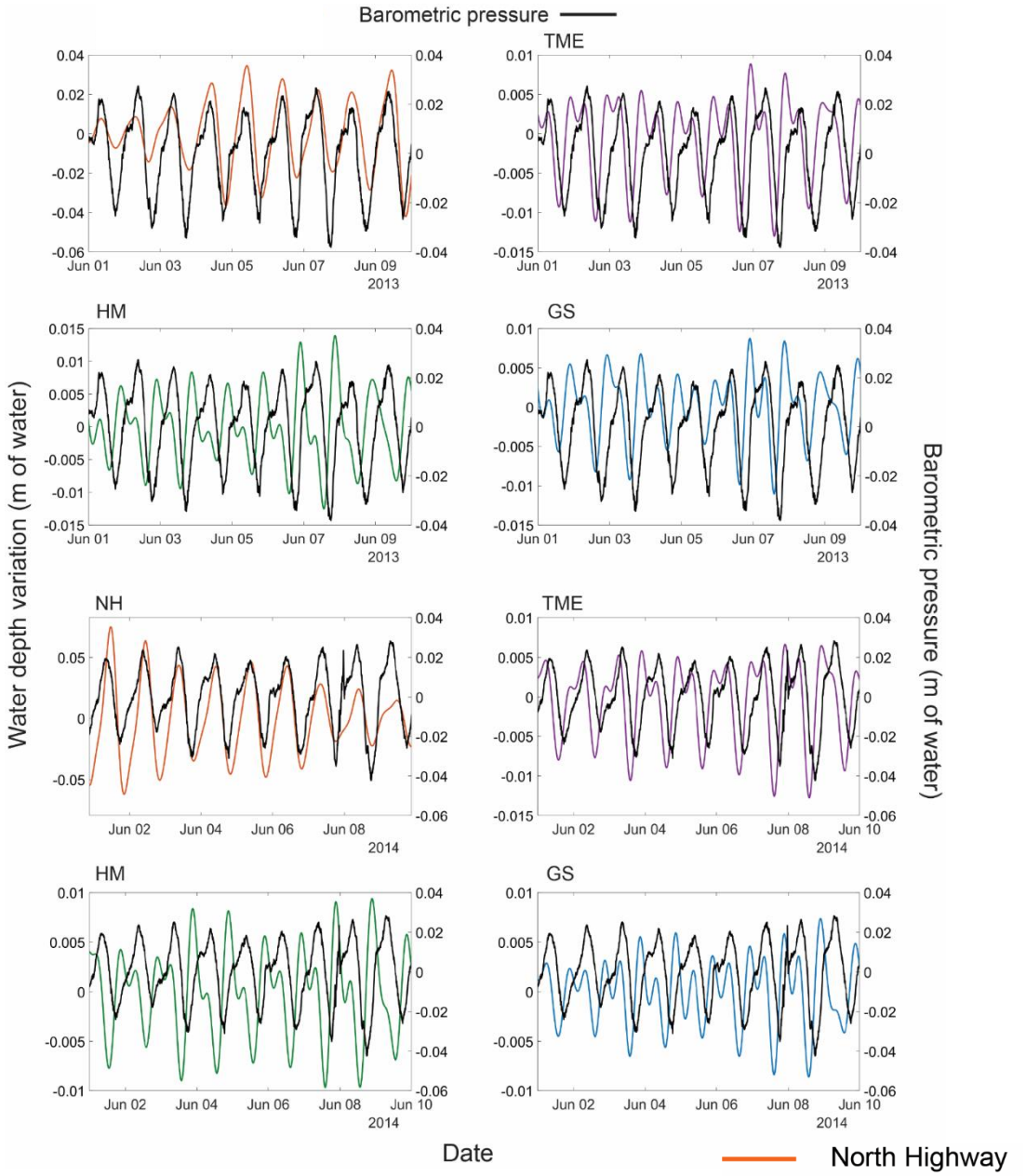

Figure 11. Smoothed and reduced spring depth (left axis) and detrended barometric pressure (right axis, black line) for a ten-day period in 2013 and 2014. Phase similarities and differences and noticeable between each spring and BP. Note different y-axis scale for NH, and HM (2013 only).

phenomenon to occur, water needs to be moving into the spring, during increases in barometric pressure. Previous work (Halihan et al., 2011; McGibbon et al., 2018) have

suggested fluid movement along the fault zone based on resistivity surveys and spring geochemistry respectively, and the increase in spring depth may be attributed to fluid moving from the fault zone to the spring. Figure 12 shows a conceptual model where the fault zone acts as storage for water, and as barometric pressure increases sharply, the pressure wave propagates through the fault damage zone, forcing water vertically and laterally towards the springs. There are no synchronous changes in temperature or specific conductance associated with these changes, indicating similar water source, and likely the springs provide the recharge for the fault zone hydrologic system, and as

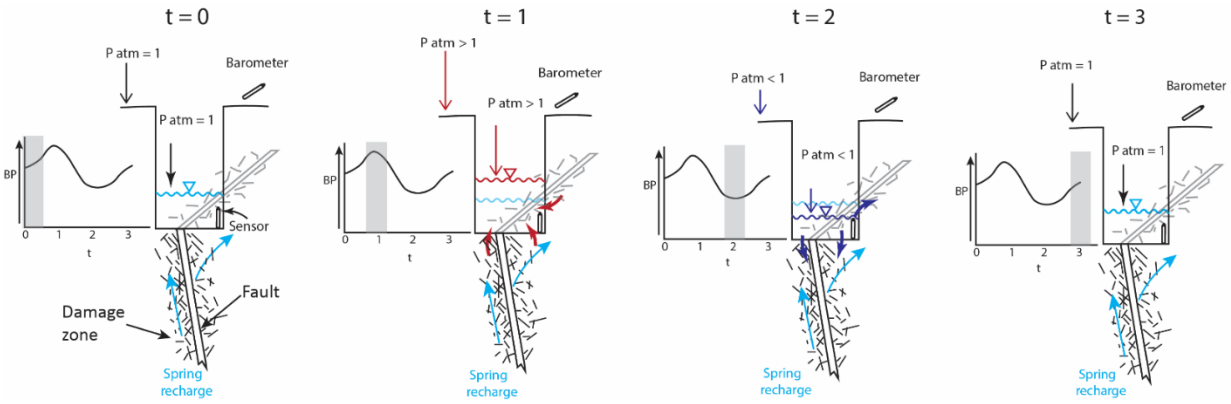

Figure 12. Model of the inferred flowpaths for ground water during changes in barometric pressure (BP) over time (t). t=0, spring water is in equilibrium with BP and fluid within the fault zone, t=1, BP increases, spring water level/ depth increases (red lines) as fluid moves both up and along the fault zone into the spring. t=2, BP decreases (dark blue lines), spring depth decreases as fluids moves back into the fault zone. t=3 BP returns to the original value, and spring water is in equilibrium with fluid within the fault zone. The lateral movement of fluid along the fault zone is considered to represent the unconfined response in the BRF, with the simultaneous increase in water depth and BP representing the negative values.

water moves from the fault to the spring, it is in equilibrium with spring temperature and specific conductivity.

A second model for the BRF relates to the water source for the spring, and which aquifer/s the water is sourced from. A well is screened at a certain depth to ensure water is sourced from the desired aquifer, in springs, this is not the case, and water can be sourced from multiple aquifers. Based on geochemistry (McGibbon et al., 2018), the Madera aquifer is considered the dominant water source for the springs, above this the San Andres-Glorietta and Agua Zarca also contribute a smaller component. Distinguishing each component is complex, and not the purpose of this paper, but each aquifer will likely respond differently to changes in barometric pressure, and these variations may influence the BRF. The San Andres-Glorietta and Agua Zarca are semi-confined to confined, bounded above by the Yeso Formation and Petrified Forrest Member of the Chinle Formation respectively (Figs 5c, d), so an unconfined response in the BRF is unlikely, but they may alter the value of the final confined BE.

The similarity in BE (~0.2 – 0.3), magnitude and timing in the change of response from unconfined to confined for each spring indicate hydrostratagrphic continuity between the springs, despite being separated by ~1.5 km. North Highway has the greatest range and variation of BRF values. This spring is to the north of the Rio Salado, and also at the base of the dip slope of the Agua Zarca (Fig 2b) and may experience recharge events, and potentially pumping from nearby wells, which are not experienced south of the river. This spring also has BRF values above one, (in this case below

negative one), so other factors, such as those mentioned above, must be affecting the BE for it to be outside of the 0 – 1 range.

Although BE alone are useful parameters, they are most useful as an intermediate value used to calculate other aquifer properties. Using the equation from Jacob (1940) and Turnadge et al., (2019), specific storage can be calculated as a function of BE:

$S_S = \rho_W \cdot g \cdot \theta_E \cdot C_W / BE$, Where

S_S = specific storage,

ρ_W = water density

g = gravitational constant

C_W = compressibility of water

θ_E = effective porosity

Values for three of these variable are generally accepted to be: $\rho_W \approx 1000 kg/m^3$, $g \approx 9.81\ m/s^2$ $C_W \approx 4.58 \times 10^{-10}$ (for freshwater) (Turnage et al, 2019). Effective porosity is site and lithology specific but, with no exposures of the Madera limestone locally, a range of values has been taken from the literature, 5 – 40% (Jenkins, 1982; Fitts, 2014). Figure 13

shows the values for specific storage for a range of BE and θ_E values. The confined BE has a range of values from ~0.1 - 0.3 (Fig 9b), which give specific storage values between

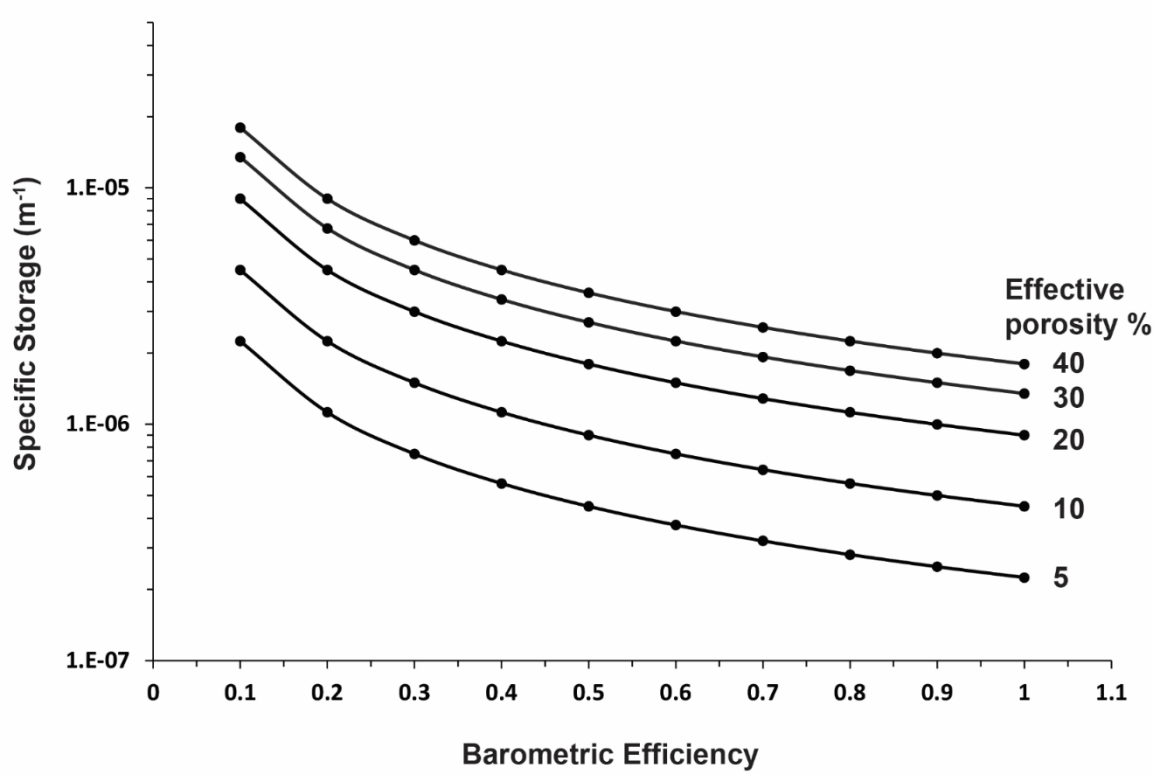

Figure 13. Specific storage values for a range of BE and effective porosity. The confined response is limited to a BE of 0.1 – 0.3. Values above this represent the unconfined response, but porosity in the fault zone is likely different then in the aquifer.

7×10^{-7} to 2×10^{-5} m^{-1}. These include the extreme ranges of porosity values, and a more realistic range will be closer to 1×10^{-6} to 1.5×10^{-5} m^{-1} (θ_E from 10 to 30%). These latter values are closer to those proposed by Batu (1998) for fissured rock of 4.9×10^{-6} to 6.8×10^{-5} m^{-1}, but higher than values for limestone from Kuang et al., (2020) of 1.6×10^{-7} to

4.21×10^{-7} m^{-1}. The Agua Zarca and San Andreas-Glorieta are both sandstone aquifers, with Ss values up to 8.75×10^{-5} m^{-1} (Kuang et al., 2020), and the calculated Ss for the springs may be increased by these aquifers. Further to this, a key assumption in the Jacob (1940) solution, is that grains are incompressible, if compressible grains are considered, then values for specific storage will be overestimated (van de Kamp and Gale, 1983). Also, the semi-confined nature of the aquifer may also lead to higher specific storage values due to leakage from aquitards. These three points help to explain the high Ss values for the springs sourced from what is considered a predominantly limestone aquifer, but the fluid movement along the faulty may play a role, as describe above.

Earth tides

Earth tides analysis focused on cycles between 12 and 24 hours. This was based on the periodic nature of depth variations, which coincided with these time periods. Figure 14 shows smoothed and deduced spring depth data (as in Fig 11) and synthetic Earth tide Data. Power spectral density plots (psd) of each spring can be seen in figure (15). The first noticeable aspect is all spring have power at periods of 12 and 24 hours coinciding with known Earth tides. The relative power of each peak varies within each spring, and from spring to spring. In general spectral power decreases from north to south, by an order of magnitude, and power at 1 cycle/day (24 hours) is greater at North

Highway and Twin Mound East, and also shows a decrease from north to south. Figure 16 shows psd for barometric pressure (black line) and synthetic Earth tide (red line).

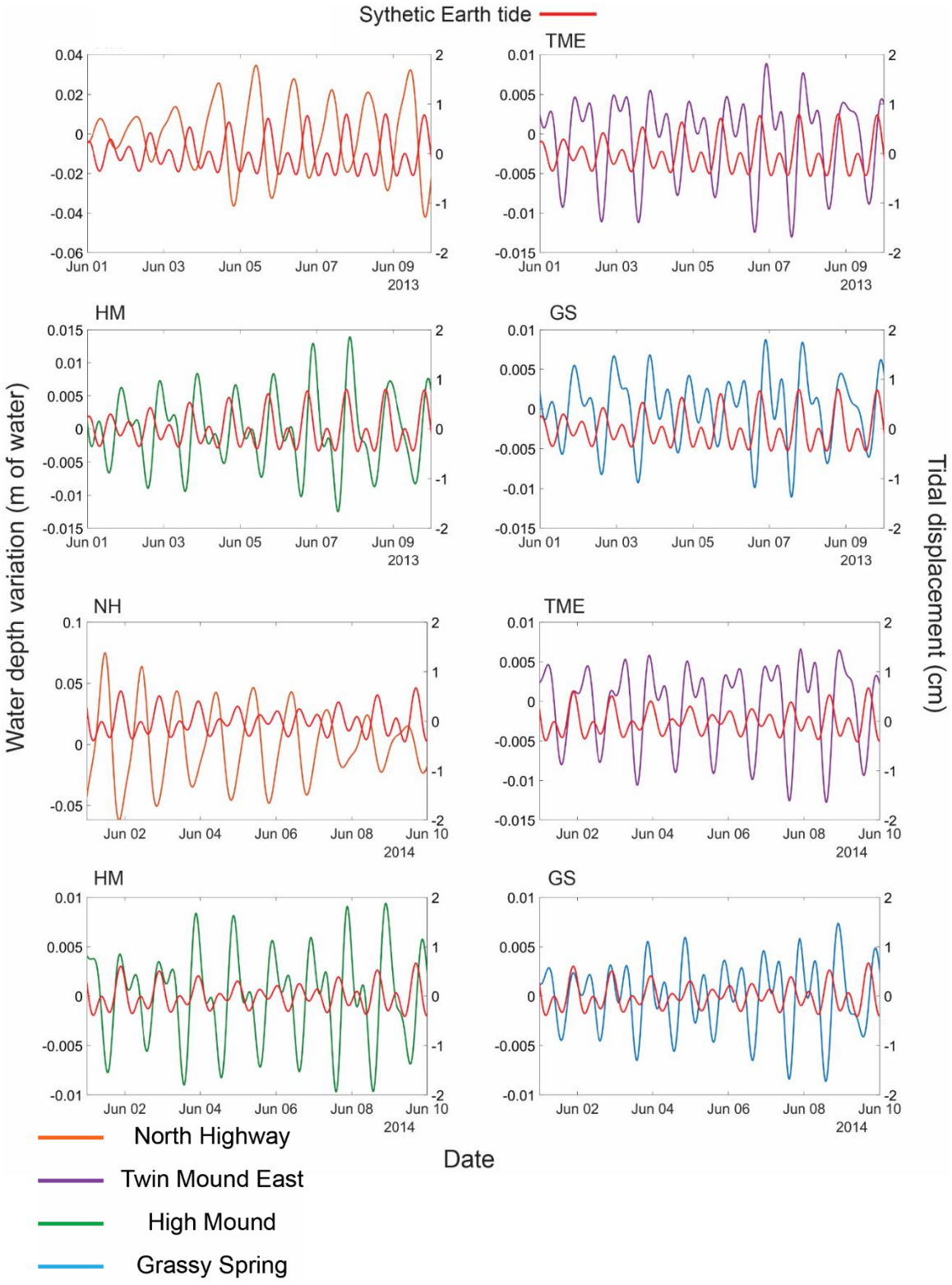

Figure 14. Smoothed and reduced spring depth (left axis) and synthetic Earth tide displacement (right axis). Phase similarities and differences and noticeable between each spring and ET. Note different y axis scale for NH, and HM (2013 only).

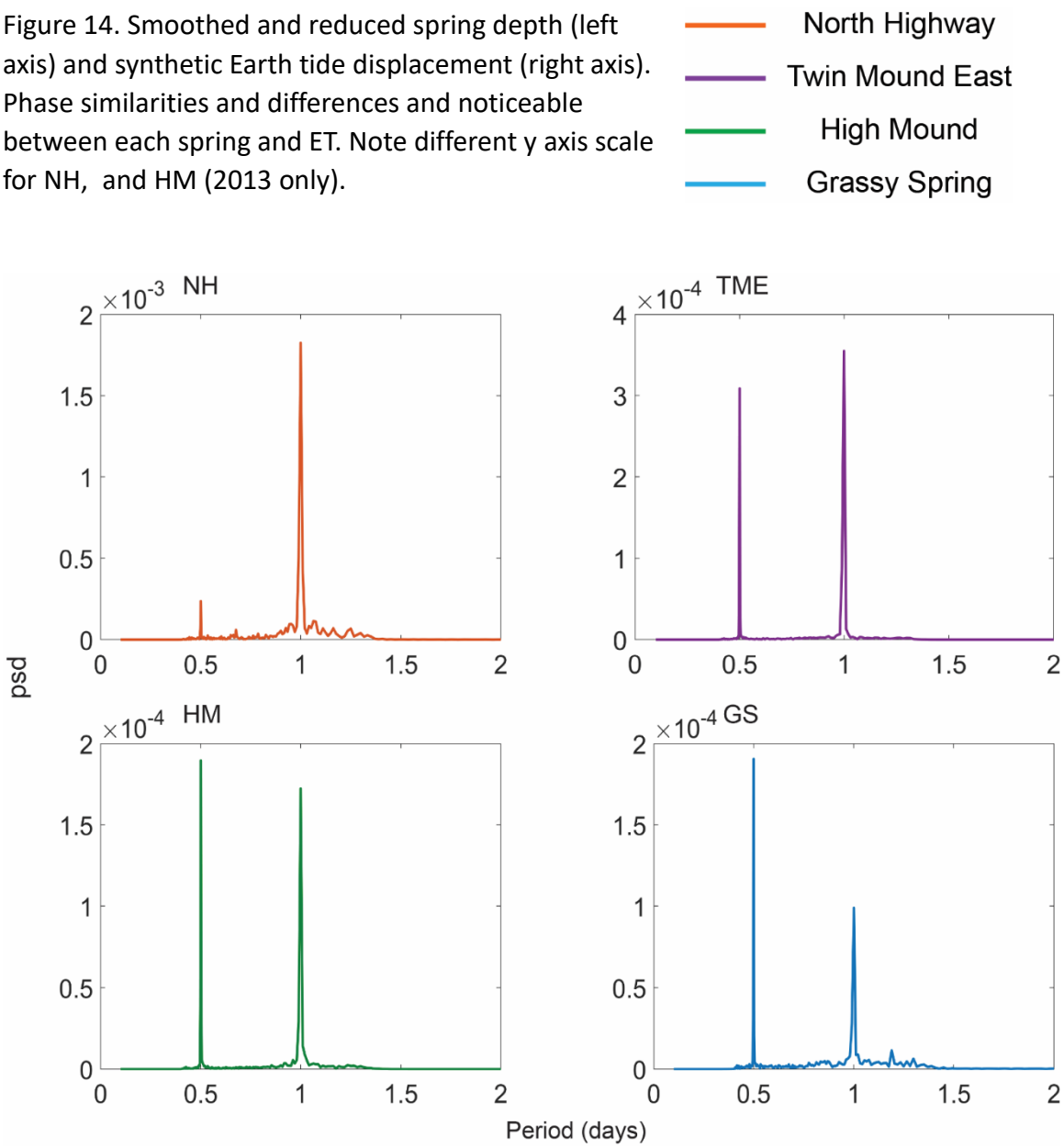

Figure 15 – psd for all springs. Spectral peaks occur at 12 and 24 hours. Spectral power decreases by two orders of magnitude from north to south for peaks at 24 hours (Figure 2 for spring locations), but similarities between proximal spring peaks occur at 12 hours.

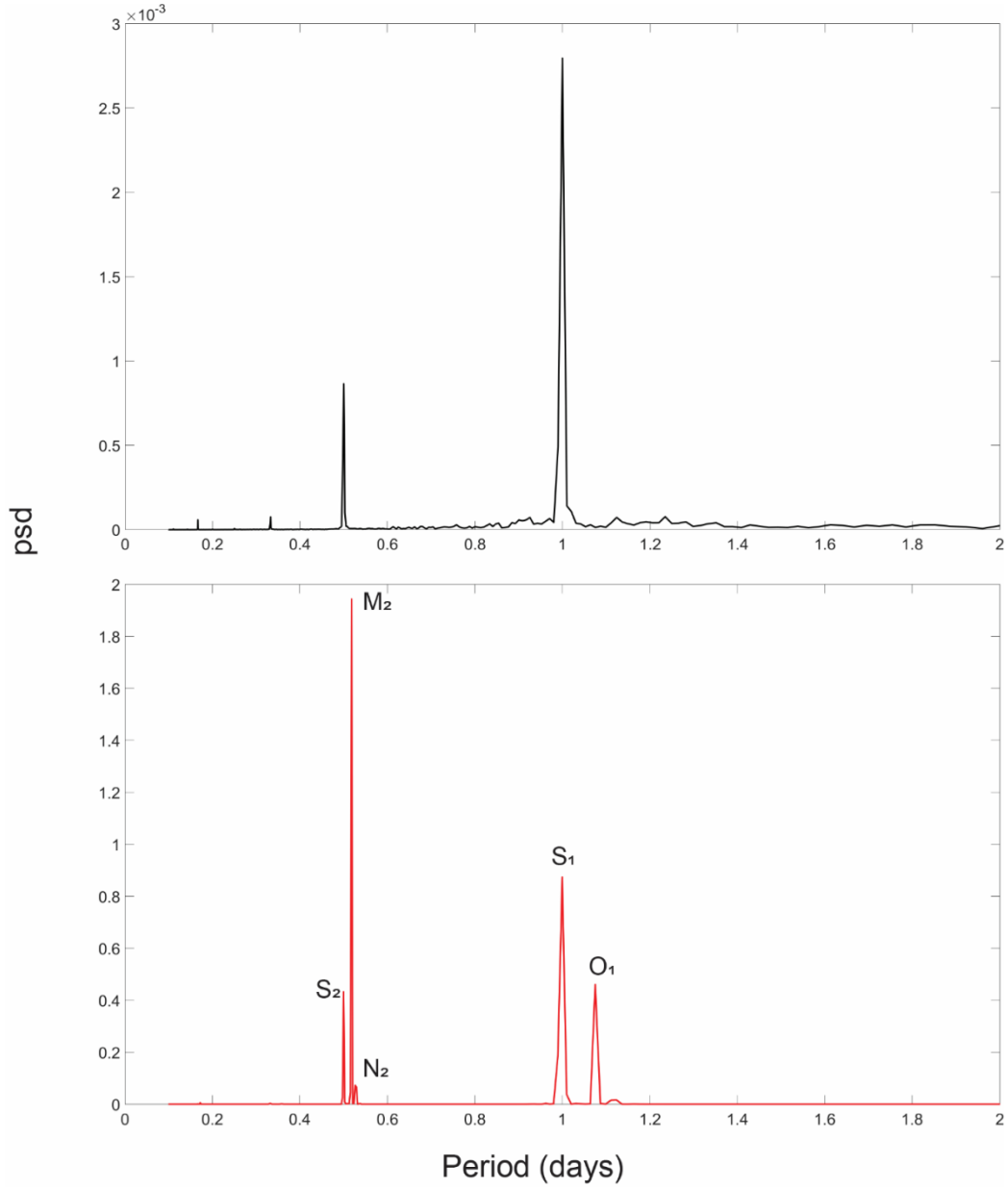

Figure 16 – psd for Barometric pressure (black line) and theoretical Earth tide (red line). Spectral peaks occur at 12 and 24 hours for BP. Earth tide peaks coincide with earth tides of S2 -12 hours (solar semi-diurnal), M2 – 12.421 hours, N2 – 12.658 hours, S1 -24 hours (solar diurnal), O1 – 25.819 hours.

The barometric pressure psd has power at 12 and 24 hours (and smaller peaks at 6 and

8 hours), with the greater power at 24 hours. The psd for the synthetic Earth tide has a

range of peaks (Fig 16, Table 2), but the S_1 and S_2 peaks align with spectral peaks in the spring and barometric pressure psds.

Tidal constituent	Period (hours)
S_2 (Solar semi-diurnal)	12
M_2	12.421
N_2	12.625
S_1 (Solar diurnal)	24
O_1	25.819

Table 2. Tidal constituent and period present in synthetic Earth tide.

The spectral peaks for the barometric pressure psd are not due to Earth tides, but are associated with heating of the atmosphere by the Sun, which generates atmospheric/thermal tides. The timing of these peaks makes distinguishing spring water level variations due to Earth tides alone problematic. Pervious workers (Merritt, 2004) have dealt with this by using tidal components other than S_1 and S_2, but the timing of the spectral peaks for the springs are limited to 12 and 24 hours (compare Figs 15 and 16). This naturally leads to the question of whether Earth tides are present in data, as it is possible that the spectral peaks are caused by barometric pressure alone. As the BE for each of the springs are similar (Fig 9b) and the spectral power of each peak changes spatially, it is potentially a combination of barometric pressure and Earth tides which affected spring depth, but with Earth tide frequencies limited to tidal constituents S_1

and S_2 (24 and 12 hours). This combination of factors effecting spring depth could also help explain the BRF above 1 (below negative 1) for North Highway.

Conclusions

Over two years of autonomous sensor monitoring at multiple springs along the Nacimiento fault, NM, provides a first attempt using spring depth data alone to investigate aquifer properties using the aquifer's response to loading. The Barometric Response Function indicates springs are semi-confined with a barometric efficiency of ~0.2, but also have an initial unconfined response with negatives values indicating water is recharging the spring pool with increases in barometric pressure. The location of springs along the Nacimiento fault is believed to be a factor, with water stored within the fault zone being forced towards the springs with increases in barometric pressure. The lack of emerging water/springs outside of areas draped with travertine and at lower elevations, suggests cross fault fluid movement is minimal, or at least permeability across the fault is much lower than within the fault plane. The similarity in timing and magnitude of the BRF indicate hydrostratagrphic continuity between the springs, at distances of 1.5 km. Specific storage values for the springs calculated from BE are 1×10^{-6} to 1.5×10^{-5} m^{-1} (θ_E from 10 to 30%). These values are higher than expected for a limestone aquifer, but with higher specific storage values for the overlaying sandstone Agua Zarca and San Andreas-Glorieta aquifers, assumption for the Jacob (1940) solution,

and semi-confined (leaky) nature of the aquifers, a higher specific storage value may be justified. In considering barometric efficiency, there are numerous issues to bear in mind. As the study sites are springs and not wells, the nature of recharge to the spring pool, and discharge/leakage to the fault zone will affect the BRF in ways not fully understood. The artesian nature of the springs may also influence how the spring responds to changes barometric pressure.

Spectral analysis shows the springs have power at 1 and 2 cycles/day (24 and 12 hours). Although these coincide with Earth tidal constituents S_1 and S_2 (24 and 12hours respectively), they are difficult to separate from atmospheric tides (barometric pressure), which also have power at 1 and 2 cycles/day. Spectral power decreases spatially from north to south across the springs, and potentially both Earth tides and barometric pressure cycles are present, which explains this change, as Earth tide affects vary depending on location on the Earth. pressure cycle may contribute to the above 1 (below negative 1) values in the BRF for North Highway. This combined Earth tide and barometric pressure cycle may contribute to the above 1 (below negative 1) values in the BRF for North Highway.

Acknowledgments

The authors would like to thank the Bureau of Land Management, and anonymous reviewers for there feedback and input. This work was supported in part from the NSF EPSCoR, Geothermal (Award#IIA-1301346; to Laura Crossey).

References

Acworth, R. I., Halloran, L. J. S., Rau, G. C., Cuthbert, M. O., & Bernardi, T. L. (2016), An objective frequency domain method for quantifying confined aquifer compressible storage using Earth and atmospheric tides, *Geophysical Research Letters*, *43*(22), 11,671-11,678. https://doi.org/10.1002/2016GL071328

Agnew, D. C. (2005), Earth Tides: an Introduction. https://doi.org/10.1002/asi

Anderson, E. I., & Bakker, M. (2008), Groundwater flow through anisotropic fault zones in multiaquifer systems, *Water Resources Research*, *44*(11). https://doi.org/10.1029/2008WR006925

Batu, V. (1998), Aquifer hydraulics : a comprehensive guide to hydrogeologic data analysis, 727.

Bense, V. F., Gleeson, T., Loveless, S. E., Bour, O., & Scibek, J. (2013), Fault zone hydrogeology, *Earth-Science Reviews*, *127*, 171–192. https://doi.org/10.1016/j.earscirev.2013.09.008

Bense, V. F., & Person, M. A. (2006), Faults as conduit-barrier systems to fluid flow in siliciclastic sedimentary aquifers, *Water Resources Research*, *42*(5). https://doi.org/10.1029/2005WR004480

Bense, V. F., Person, M. A., Chaudhary, K., You, Y., Cremer, N., & Simon, S. (2008), Thermal anomalies indicate preferential flow along faults in unconsolidated sedimentary aquifers, *Geophysical Research Letters*, *35*(24). https://doi.org/10.1029/2008GL036017

Bense, V. F., Van Balen, R. T., & De Vries, J. J. (2003), The impact of faults on the hydrogeological conditions in the Roer Valley Rift System: An overview, *Geologie En Mijnbouw/Netherlands Journal of Geosciences*, *82*(1), 41–54. https://doi.org/10.1017/S0016774600022782

Bohling, G. C., Jin, W., & Butler, J. J. (2011), *Kansas Geological Survey Kansas Geological Survey Barometric Response Function Software User's Guide*. Retrieved from www.kgs.ku.edu

Bredehoeft, J. D. (1967), Response of well-aquifer systems to Earth tides. *Journal of Geophysical Research*, *72*(12), 3075. https://doi.org/10.1029/JZ072i012p03075

Burbey, T. J., & Zhang, M. (2010), Assessing Hydrofracing Success from Earth Tide and Barometric Response. *Ground Water*, *48*(6), 825–835. https://doi.org/10.1111/j.1745-6584.2010.00704.x

Butler, J. J., Jin, W., Mohammed, G. A., & Reboulet, E. C. (2011), New insights from well responses to fluctuations in barometric pressure, *Ground Water*, *49*(4), 525–533. https://doi.org/10.1111/j.1745-6584.2010.00768.x

Caine, J., Evans, J., & Forster, C. (1996), Fault Zone Architecture and Permeability Structure, *Geology*, *18*(11), 1025. https://doi.org/https://doi.org/10.1130/0091-7613(1996)024<1025:FZAAPS>2.3.CO;2

Cook, S.B., (2020), Exploring for the Future-Barometric response function interpretations in the McBride and Nulla basalt provinces: Upper Burdekin region, North Queensland, https://doi.org/10.11636/Record.2020.052

Cook, S. B., Timms, W. A., Kelly, B. F. J., & Barbour, S. L. (2017), Improved barometric and loading efficiency estimates using packers in monitoring wells, *Hydrogeology Journal*, *25*(5), 1451–1463. https://doi.org/10.1007/s10040-017-1537-9

Cron, B. (2012), Geochemical characteristics and microbial diversity of CO2-rich mound springs of the Tierra Amarilla anticline, New Mexico, *Earth and Planetary Sciences ETDs*. Retrieved from https://digitalrepository.unm.edu/eps_etds/13

Crouch, T. M. (1994), Hydrogeology and aquifer test on the San Andres-Glorieta Aquifer on the southwest part of the Zuni Indian Reservation, Cibola County, New Mexico, *Water-Resources Investigations Report*. https://doi.org/10.3133/WRI944033

Evans, J. P., Forster, C. B., & Goddard, J. V. (1997), Permeability of fault-related rocks, and implications for hydraulic structure of fault zones, *Journal of Structural Geology*, *19*(11), 1393–1404. https://doi.org/10.1016/S0191-8141(97)00057-6

Fileccia, A. (2001), Correcting water level data for barometric pressure fluctuations. Theoretical approach and a case history for an unconfined karst aquifer (Otavi, Namibia), *Acque Sotterranee*, (n.126), 22. Retrieved from www.acquesotterranee.com

Fitts, C. R. (2013), Groundwater Science. *Groundwater Science*, https://doi.org/10.1016/C2009-0-62950-0

Fuentes-Arreazola, M. A., Ramírez-Hernández, J., & Vázquez-González, R. (2018), Hydrogeological properties estimation from groundwater level natural fluctuations analysis as a low-cost tool for the Mexicali Valley Aquifer, *Water (Switzerland)*, *10*(5). https://doi.org/10.3390/w10050586

Furbish, D. J. (1991). The response of water level in a well to a time series of atmospheric loading under confined conditions, *Water Resources Research*, *27*(4), 557–568, https://doi.org/10.1029/90WR02775

Galloway, D., and S. Rojstaczer (1988), Analysis of the frequency response of water levels in wells to Earth tides and Atmospheric loading, in Proceedings of the Fourth Canadian/American Conference on Hydro- geology. Fluid Flow, Heat Transfer and Mass Transport in Fractured Rocks, vol. 4, pp. 100–113, National Water Well Association, Dublin, Ohio

Godin, G. (1972). The analysis of tides, [Toronto] ;[Buffalo]: University of Toronto Press.

Halihan, T., Crossey, L. J., Karlstrom, K. E., Cron, B. R., Halihan, T., Crossey, L. J., … Cron, B. R. (2011), ERI investigation of fluid flow in the Nacimiento Fault, New Mexico, *AGUFM*, *2011*, H11H-02

Heffner, J., & Fairley, J. (2006), Using surface characteristics to infer the permeability structure of an active fault zone, *Sedimentary Geology*, *3–4*(184), 255–265. https://doi.org/10.1016/J.SEDGEO.2005.11.019

Hsieh, P. A., Bredehoeft, J. D., & Farr, J. M. (1987), Determination of aquifer transmissivity from Earth tide analysis. *Water Resources Research*, *23*(10), 1824–1832, https://doi.org/10.1029/WR023i010p01824

Hussein, M. E. A., Odling, N. E., & Clark, R. A. (2013), Borehole water level response to barometric pressure as an indicator of aquifer vulnerability, *Water Resources Research*, *49*(10), 7102–7119. https://doi.org/10.1002/2013WR014134

Hussein, M. E. A., Odling, N. E., & Clark, R. A. (2013), Borehole water level response to barometric pressure as an indicator of aquifer vulnerability, *Water Resources Research*, *49*(10), 7102–7119. https://doi.org/10.1002/2013WR014134

Jacob, C. E. (1940), On the flow of water in an elastic artesian aquifer, *Eos, Transactions American Geophysical Union*, *21*(2), 574–586. https://doi.org/10.1029/TR021I002P00574

Jenkins, D. N., & Prentice, J. K. (1982), Theory for Aquifer Test Analysis in Fractured Rocks Under Linear (Nonradial) Flow Conditions, *Groundwater*, *20*(1), 12–21. https://doi.org/10.1111/J.1745-6584.1982.TB01325.X

Kuang, X., Jiao, J. J., Zheng, C., Cherry, J. A., & Li, H. (2020), A review of specific storage in aquifers. *Journal of Hydrology*, *581*, 124383, https://doi.org/10.1016/J.JHYDROL.2019.124383

Mayer, A., May, W., Lukkarila, C., & Diehl, J. (2007), Estimation of fault-zone conductance by calibration of a regional groundwater flow model: Desert Hot Springs, California, *Hydrogeology Journal*, *15*(6), 1093–1106. https://doi.org/10.1007/s10040-007-0158-0

McGibbon, C., Crossey, L. J., Karlstrom, K. E., & Grulke, T. (2018), Carbonic springs as distal manifestations of geothermal systems, highlighting the importance of fault pathways and hydrochemical mixing: Example from the Jemez Mountains, New Mexico, *Applied Geochemistry*, *98*, 45–57. https://doi.org/10.1016/j.apgeochem.2018.08.015

Melchior, P. J. (1983), The tides of the planet earth (2nd ed.,. New York: Pergamon Press. Retrieved from https://bibdata.princeton.edu/bibliographic/991497833506421

Merrit, M. L. (2004), Estimating hydraulic properties of the Floridan Aquifer System by analysis of Earth-tide, ocean-tide, and barometric effects, Collier and Hendry Counties, Florida, *U.S. GEOLOGICAL SURVEY*, *03*(4267), 70. https://doi.org/10.3133/wri034267

Narasimhan, T. N., Kanehiro, B. Y., & Witherspoon, P. A. (1984), Interpretation of earth tide response of three deep, confined aquifers (USA), *Journal of Geophysical Research*, *89*(B3), 1913–1924. https://doi.org/10.1029/JB089iB03p01913

Phillips, F. M., Mills, S., Hendrickx, M. H., & Hogan, J. (2003), Environmental tracers applied to quantifying causes of salinity in arid-region rivers: Results from the Rio Grande Basin, Southwestern USA. *Developments in Water Science*, *50*(C), 327–334, https://doi.org/10.1016/S0167-5648(03)80029-1

Rasmussen, T. C., & Crawford, L. A. (1997), Identifying and removing barometric pressure effects in confined and unconfined aquifers. *Ground Water*, *35*(3), 502–511, https://doi.org/10.1111/j.1745-6584.1997.tb00111.x

Rhoads, G.H. Jr., and E.S. Robinson. (1979), Determination of aquifer parameters from well tides. Journal of Geophysical Research 84, no. B11: 6071–6082

Rojstaczer, S., & Agnew, D. C. (1989), The Influence of Formation Material Properties on the Response of Water Levels in Wells to Earth Tides and Atmospheric Loading. Journal of Geophysical Research, *94*(10), 403–412. Retrieved from

Shen, Q., Zheming, S., Guangcai, W., Qingyu, X., Zejun, Z., & Jiaqian, H. (2020), Using water-level fluctuations in response to Earth-tide and barometric-pressure changes to measure the in-situ hydrogeological properties of an overburden aquifer in a coalfield, *Hydrogeology Journal*, 1–15. https://doi.org/10.1007/s10040-020-02134-w

Shih, D. C.-F. (2018). Storage in confined aquifer: Spectral analysis of groundwater in responses to Earth tides and barometric effect, *Hydrological Processes*, *32*(12), 1927–1935, https://doi.org/10.1002/hyp.13131

Smith, J. (2016), CO2 Flux Along Faults of the Central Rio Grande Rift, New Mexico, 103, Retrieved from http://digitalrepository.unm.edu/%0Aeps_etds/108

Spane, F. A. (2002), Considering barometric pressure in groundwater flow investigations, *Water Resources Research*, *38*(6), 14-1-14–18. https://doi.org/10.1029/2001WR000701

Theis, C. V. (1935), The relation between the lowering of the Piezometric surface and the rate and duration of discharge of a well using ground-water storage, *Eos, Transactions American Geophysical Union*, *16*(2), 519–524. https://doi.org/10.1029/TR016i002p00519

Toll, N. J., & Rasmussen, T. C. (2007), Removal of barometric pressure effects and earth tides from observed water levels, *Ground Water*, *45*(1), 101–105. https://doi.org/10.1111/j.1745-6584.2006.00254.x

Turnadge, C., Crosbie, R. S., Barron, O., & Rau, G. C. (2019), Comparing Methods of Barometric Efficiency Characterization for Specific Storage Estimation, *Groundwater*, *57*(6), 844–859. https://doi.org/10.1111/gwat.12923

Van Camp, M., & Vauterin, P. (2005), Tsoft: graphical and interactive software for the analysis of time series and Earth tides, *Computers & Geosciences*, *31*(5), 631–640. https://doi.org/10.1016/J.CAGEO.2004.11.015

Van Der Kamp, G., & Gale, J. E. (1983), *Theory of Earth Tide and Barometric Effects In Porous Formations With Compressible Grains*, *WATER RESOURCES RESEARCH* (Vol. 19). Retrieved from https://agupubs.onlinelibrary.wiley.com/doi/pdf/10.1029/WR019i002p00538

Weeks, E. P. (1979), Barometric fluctuations in wells tapping deep unconfined aquifers, *Water Resources Research*, *15*(5), 1167–1176. https://doi.org/10.1029/WR015I005P01167

Wells, S. G., Grambling, J. A., & Callender, J. F. (1982), New Mexico Geological Society Geohydrology of the Madera Group, western Estancia Basin, New Mexico Annual NMGS Fall Field Conference Guidebooks, *370*, 361–366

Zhang, H., Shi, Z., Wang, G., Sun, X., Yan, R., & Liu, C. (2019), Large Earthquake Reshapes the Groundwater Flow System: Insight From the Water-Level Response to Earth Tides and Atmospheric Pressure in a Deep Well, *Water Resources Research*, *55*(5), 4207–4219. https://doi.org/10.1029/2018WR024608

SUPPLIMENTARY MATERIAL

Full time series data are available in the excel sheet ‘chpt2_Data’

Supplementary Figures and Tables

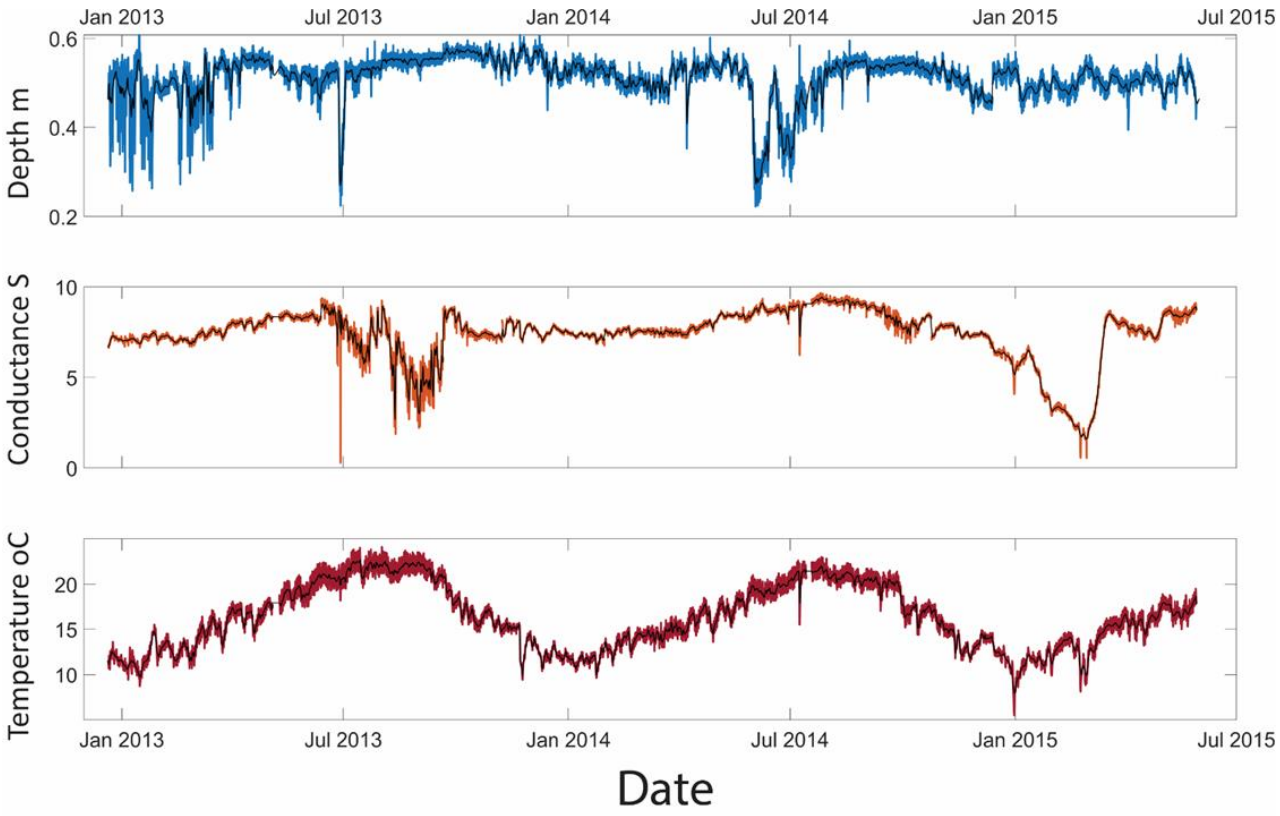

Figure S1. – North Highway depth, conductivity and temperature, with daily moving mean (black line). Depth has greatest variation during the start of the monitoring period and large decreases in July 2013 and 14. Conductance has mostly 'stable' values with sharp decreases in July 2013 and 14m a large decrease from Feb –March 2015. Temperature variations track daily and seasonal changes, with occasional sharp decreases. Synchronous variations in values occur, in all parameters, potentially associated with precipitation events

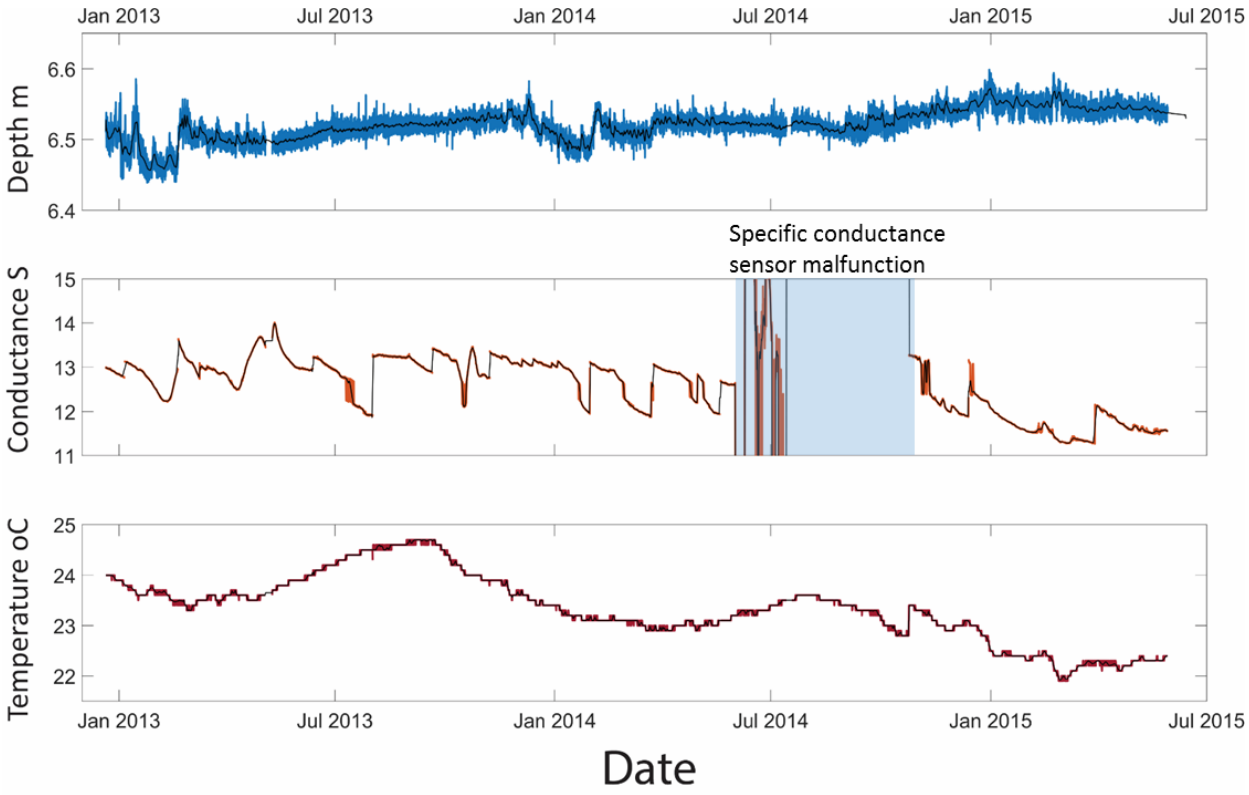

Figure S2. – Twin Mound East depth, Conductivity and Temperature, with daily moving mean (black line). Depth has variations during the start of the monitoring period and a decrease in Jan 2014. Depth values are relativity stable, but there is a general increasing trend across the data ~2 cm.

Conductance values with lower steadily, the increase sharply. From June to July of 2014 there was a sensor malfunction.

Temperature variations track seasonal changes. Variations are small ~1 ^{o}C across each year, but a general decreasing trend is seen.

Figure S3. – High Mound depth, Conductivity and Temperature, with daily moving mean (black line). Depth has greatest variation during Aug – Sept of 2013 and 14, with an increase in depth associated with both times. There is an increase in depth across the data of ~6 cm. Conductance has variations associated with variations in temperature. Temperature variations track daily and seasonal changes. Synchronous variations in values occur, in conductivity and temperature.

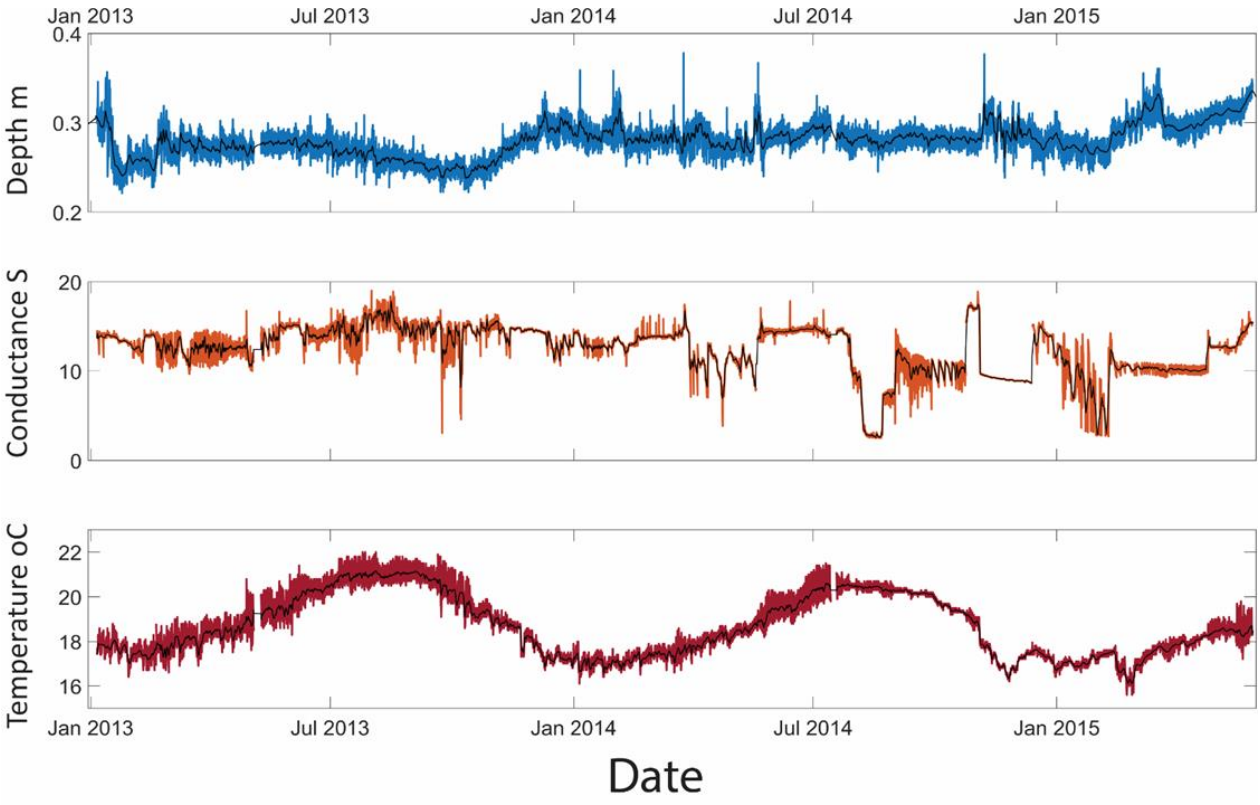

Figure S4. – Grassy Spring depth, Conductivity and Temperature, with daily moving mean (black line). Depth variations are small, but there are large, ~5 cm, increases which spike the data through 2014. Conductance has mostly 'stable' values with decreases that are considered to be associated with sensor malfunction or biofouling. Temperature variations track daily and seasonal changes. Synchronous variations in values occur, in all parameters, potentially associated with precipitation events

Full time series data for all springs and parameters - See the attached Excel data files 'SYData_Depth', 'SYData_Temp' and 'SYData_SpCond'.

CHAPTER 3: Fence Spring system of Grand Canyon: Insight into the karst aquifer system of the Colorado Plateau region

Authors and affiliations

C. McGibbon[1]*, Laura J. Crossey[1], Karl E. Karlstrom[1]

1. Department of Earth and Planetary Sciences, University of New Mexico, Albuquerque, NM 87131

Abstract

Fence springs are the highest discharge springs of the Redwall-Muav (R-M) karst aquifer in Marble Canyon, eastern Grand Canyon, Arizona. Vents on opposite banks of the Colorado River within the Fence fault system have similar chemistries indicating the springs are connected hydrologically within the confined karst aquifer below the Colorado River. Stable isotopes fingerprint the main recharge area for both springs to be the Kaibab Plateau, west of the river. Chemical variation in nearby R-M springs indicates complex mixing between karst base flow, as represented by the Fence springs, and fast-traveled meteoric waters. A 7-year record from 2012 to 2019 from autonomous sensors identifies the base flow to have steady temperature (21 °C) and specific conductance (2000 µS/cm) and no seasonality. A progressive decrease of 1.5 °C and 100 µS/cm in both springs over 7 years suggests declining discharge accompanying declining meteoric recharge. Fortuitous high-flow experiments in the Colorado River in 2012, 2013, 2014, 2016, and 2018 during Glen Canyon Dam management operations provide an experiment analogous to a "slug test" for the groundwater system. Rapid increase in river level from ~5000 to 43,000 cubic feet per second (cfs; 1218 m^3/s) caused the springs to be inundated and mixed with river water. Recovery curves showed rapid return of spring temperature from ~10 to 21 °C and specific conductance from 500 to 2000 µS at stages below ~ 10,000 cfs. An increase in short-term fluctuations during recovery in post-2016 experiments also supports declining spring discharge through the seven-year period.

Introduction

Grand Canyon's > 1- km- deep incised aquifer offers a cut-away view of the hydrogeologic system of the greater Colorado Plateau region. Groundwater in the eastern Grand Canyon region is recharged from the ~ 2500 m elevation Kaibab plateau and discharged in major springs within Grand Canyon (Fig. 1). Two important examples include Roaring Spring, the major water supply source for both the North and South Rim Park developments, and Fence springs, the major spring system in Marble Canyon and the subject of this study. Figure 1B shows schematic results of a dye tracer study from sinkholes on the Kaibab Plateau that showed long distance fault-related fast pathways to major springs (Jones et al., 2018). Figure 2 shows the stacked sedimentary aquifer system of the Colorado Plateau (Huntoon, 2000) that includes world-class karst aquifers of the Redwall-Muav (R-M) aquifer, the mixed karst-sandstone aquifer of the Coconino aquifer (C- aquifer), and fault networks that allow vertical connectivity between aquifer units. The Muav and Redwall limestones form the Redwall-Muav aquifer, which discharges the vast majority of groundwater in Grand Canyon. The hydrogeology of the R-M aquifer remains incompletely characterized in part because there are few deep wells on the Coconino or Kaibab plateaus and limited geophysical surveys (Bills et al 2016; Jones et al., 2017). Fence spring system in Marble Canyon (Figs. 1C, D) is a unique example of a high discharge artesian spring system, located along a normal fault system, which vents from the Redwall-Muav aquifer on opposite banks of the Colorado River. This spring system represents most of the groundwater discharge for the 50-mile stretch of Marble Canyon between Lees Ferry and the Eminence fault.

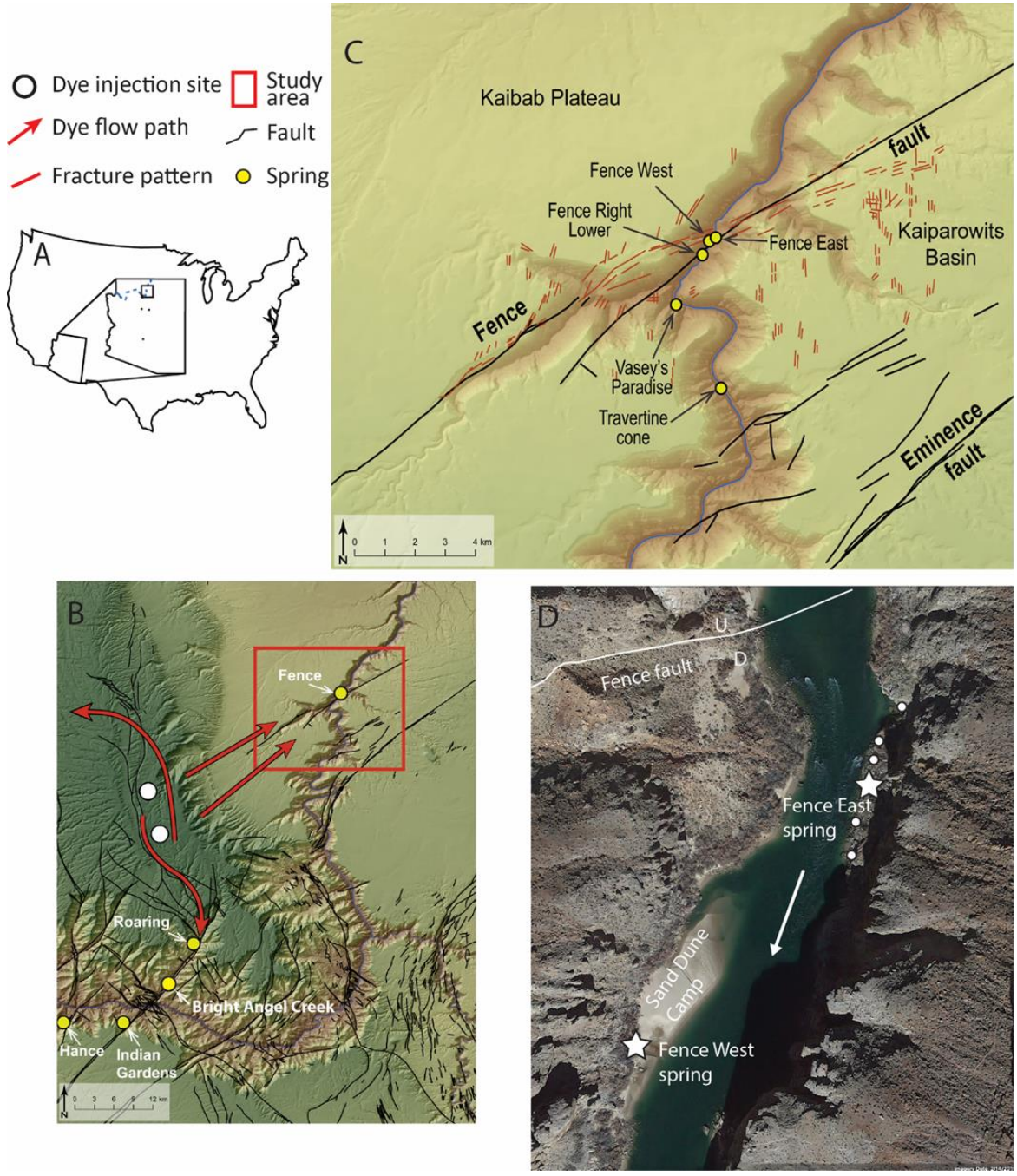

Figure 1. Springs and faults of the Fence fault area of Marble Canyon. **1A**) location in Arizona, western U.S.; **1B**) location relative to Kaibab uplift with white dots showing injection locations for dye tracers that arrived within a year at Vasey's and Fence springs (Jones at al., 2008). **1C**) Fence spring system within Eminence graben showing dominant NE and N-S trending fractures that control the cave system at Vasey's Paradise (Huntoon, 1981, p. 27). **1D**) Fence East and Fence West main springs are marked with stars; subsidiary springs as dots.

It was first studied in detail by Huntoon (1981), who suggested that the springs on the east and west sides of the river are hydrologically and geochemically connected with each other, but not with the river, thus providing a case study of numerous karst aquifer characteristics. Huntoon (1981) noted that during high river stages, spring discharge still occurred, as evidenced by water temperature around the springs, and that during low stages spring temperature remained constant, indicating that river water did not enter the fault zone. He interpreted the different chemistries of the subsidiary springs of the system to reflect mixing between two end members, one represented by Fence East and the other by Fence West Lower (his Diagonal spring) that had different depths of circulation in the confined karst aquifer (Fig. 3A, B). The different chemistry of Vasey's Paradise spring, about 2 km down river (Fig. 1C), was interpreted to reflect a partially independent flowpath from the Kaibab uplift. Huntoon (2000) proposed a hypothesis for dual permeability flow with two main flowpaths: 1) unconfined high gradient cave and fault conduits carrying fast-traveled meteoric recharge; and 2) confined low gradient 3-D mazes of fractures with steady flow, high storage, and significant water-rock interaction, hence higher total dissolved solids (TDS). This concept was amplified by Crossey and others (2006, 2009) who showed several types of waters with different water chemistries that mix in Grand Canyon springs. These include geochemically potent but small volume endogenic (deeply sourced) hydrothermal fluids that ascend along faults and contain high CO_2, high TDS, and mantle-derived ^3He. These fluids interact with the large volume karst waters of the R-M aquifer (# 2 above) that are carbonic and warm due mainly to long flow paths but also potential geothermal input. These mix with meteoric recharge (# 1 above) within the stacked aquifer system. Recent dye tracer studies on the Kaibab Uplift north and west of the Colorado river (Fig. 1B) help quantify the fast-traveled component (weeks) for snowmelt and monsoonal events along the unconfined fault and cave conduits (Jones et al., 2018).

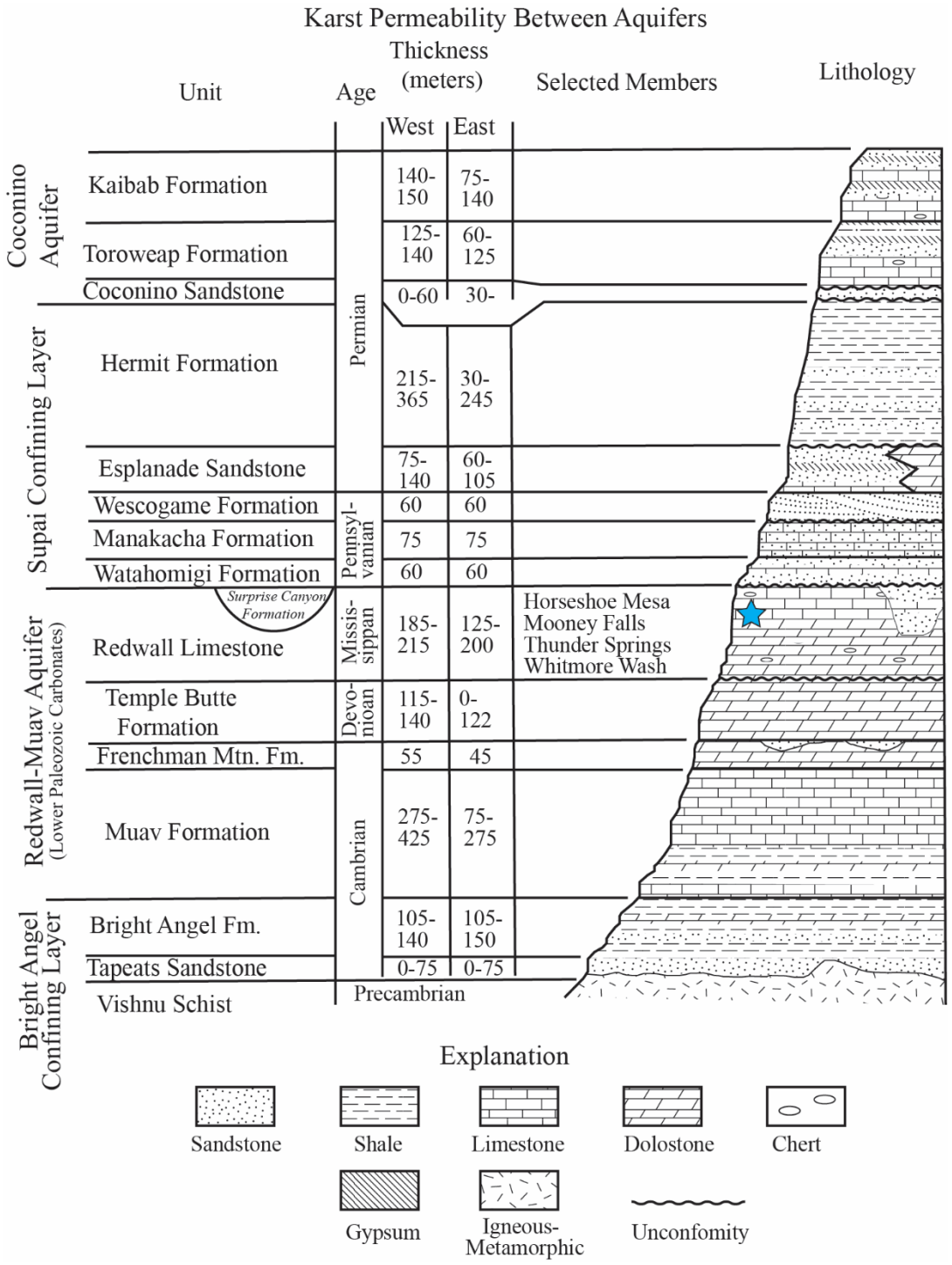

Figure 2. Paleozoic rocks and hydrostratigraphic units of the Grand Canyon region of the Colorado Plateau (modified from Huntoon, 2000). Blue star is the approximate stratigraphic level of the Fence spring system.

The goal of this paper is to further explore the interrelationships between multiple permeabilities and multiple hydrochemistries in the Grand Canyon hydrologic system by a more detailed analysis at the Fence spring system. We summarize the 17 years of campaign sampling and add major ion analyses, stable isotope geochemistry, and continuous monitoring data (depth, temperature and specific conductance). Our data reinforce the overall conclusions of a confined fault-related aquifer system that connects the springs beneath the river (Huntoon, 1981) but stable isotope data suggest that springs on both sides are sourced predominantly

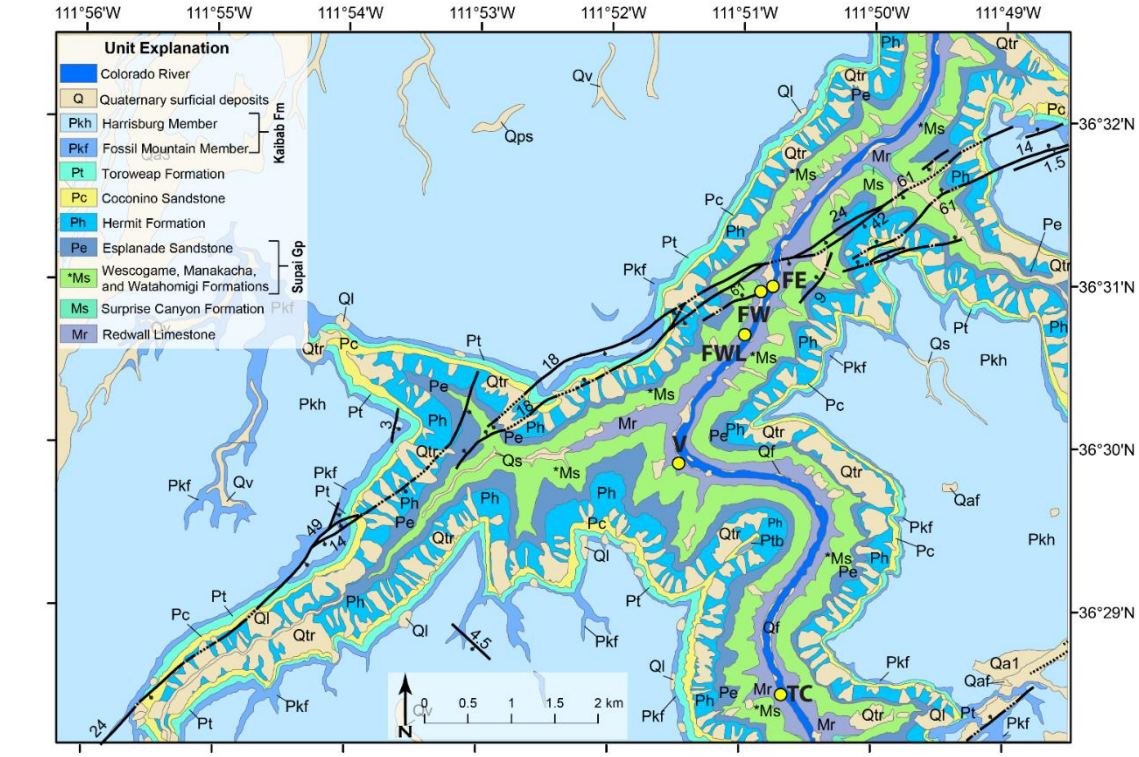

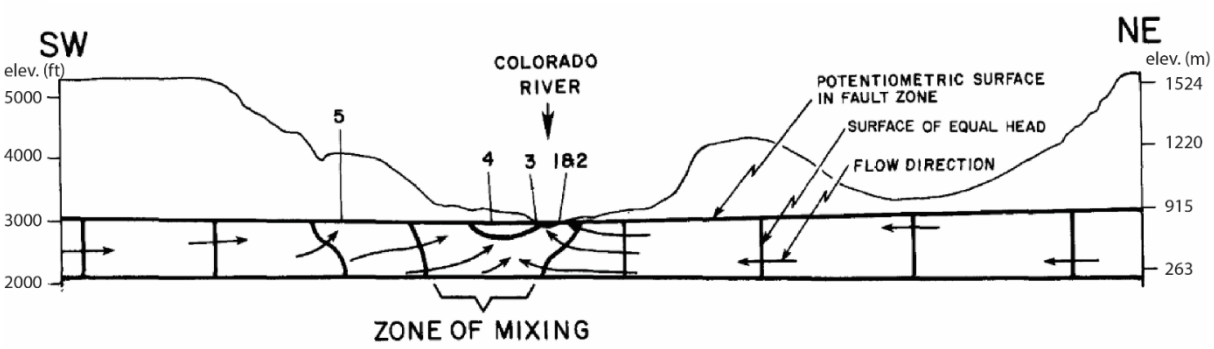

Figure 3. A) Geologic map of the Fence fault area (adapted from Billingsley and Hampton, 2000 and Billingsley and Priest, 2013); main springs (yellow dots) are shown. **B**) SW-NE, fault-parallel, cross section (Fig. 6 of Huntoon, 1980) "showing the assumed circulation system which accounts for sub-river water flow under the Colorado River, Marble Canyon, Arizona. The base of the active groundwater circulation is assumed to be the base of the soluble Paleozoic carbonates." Numbers refer to Huntoon's numbering of springs: #2 = our Fence East (FE), 4= our Fence West (FW) location, #5= our Fence West Lower location (Huntoon's Diagonal Spring). But note that the highest discharge west-side spring reported by Huntoon (1981) was his # 5 which we assume is the same as our highest discharge FW spring located at his location #4. Shift of spring vent locations between 1980 and 2012 may explain this discrepancy. Huntoon (1981) concluded that some of the water in Fence West (#3&4) originated from the east (# 1&2). In contrast, we conclude from stable isotope values that water in both the highest discharge springs of Fence East and Fence West are both derived from the Kaibab Plateau of the North Rim area to the west.

from the Kaibab Plateau west of the Colorado River. Other R-M springs within a few river miles of this spring system are shown here to be hydrochemically distinct from the overlapping Fence East and Fence West spring system, and these differences help further evaluate mixing trends, not between Fence East and Fence West, but as additions of fast and flashy (unconfined) conduit-flow waters into the slow and steady base flow (confined) pathway of the groundwater residing in the Eminence graben in the R-M karst system.

We also apply autonomous sensor technologies to look at changes through time at these springs over the past 7 years. We installed sensors in 2012 and hence have semi-continuous temperature, depth, and specific conductance data from 2012-2019. This time period included several high-flow experiments (HFE's). These were large releases, up to 43,000 cubic feet per second (cfs) (1218 m^3/s), from Glen Canyon Dam designed to refine dam management and ecosystem sustainability protocols, but they also provide us with a fortuitous set of multi-million-dollar slug test experiments to evaluate the R-M karst aquifer.

This study presents an example of the type of merged dataset of natural and anthropogenic geochemical tracers combined with spring monitoring that is needed to establish

a long-term base line for springs and groundwater within different regions of Grand Canyon. Both water supply and water quality are major concerns due to increases in visitation to Grand Canyon Village, growth of local towns of Tusayan and Valle (Fig. 1), uranium mining, and development schemes such as the Grand Canyon Escalade project (Adams 2005, Bills and Flynn 2002). As a world famous location, Grand Canyon geology has seen extensive study, but research on its hydrogeology has been somewhat more limited (Huntoon, 2000; Monroe et al 2005; Bills et al., 2016; Tobin et al, 2018; Solder et al., 2020, and references therein). An urgent need for hydrogeological research in the region is to gain a better understanding of the aquifer systems at depth, in part via analysis of karst-fed Grand Canyon springs. The Fence spring system provides an ideal locality to examine the Marble Canyon region, east of the Kaibab uplift.

Study Area

Geology and regional hydrology

Figure 4 shows the hydrologic setting of the Fence spring system in eastern Grand Canyon. Four hydrochemical waters are shown to mix in the aquifer system (Crossey et al., 2006). 1) The Colorado River is sourced by snowmelt in the Rocky Mountains and is hydrochemically distinct from local springs and groundwaters; it is cold (10 °C) because it emerges from the base of Lake Powell at Glen Canyon Dam. 2) Meteoric recharge from the Kaibab uplift finds its way down fast pathways in faults and caves through the different aquifers. 3) Karst base flow in the Redwall-Muav aquifer has the region's largest volume of storage and has a mixture of all the fluid components; groundwater moves slow enough through the karst fracture systems to equilibrate with rock and emerge at Fence springs at ~ 20 °C. 4) Small volume but geochemically potent carbonic fluids ascend along faults as shown by trace gas studies that reveal traces of mantle ^{3}He, significant deeply sourced CO_2, and a variable geothermal temperature addition (Crossey et al., 2006; 2009). The resulting mixture of different

fluid chemistries at a given spring or well depends on incompletely known end member fluid compositions and volumes within the different end member permeability pathways, defined by Huntoon (2000) as unconfined fast pathways and confined base flow. But, like Huntoon (2000), we considered there to be a spectrum among both hydrochemical and karst pathway end members that results in every imaginable gradation that can influence resulting spring discharge and hydrochemistry. The Fence spring system is an important occurrence to help understand how these mixing and pathway complexities interact because this area reflects nearly all of the water discharging east of the Kaibab uplift within Marble Canyon and its different spring compositions can be used to parse both source and flowpath differences. We compare them to

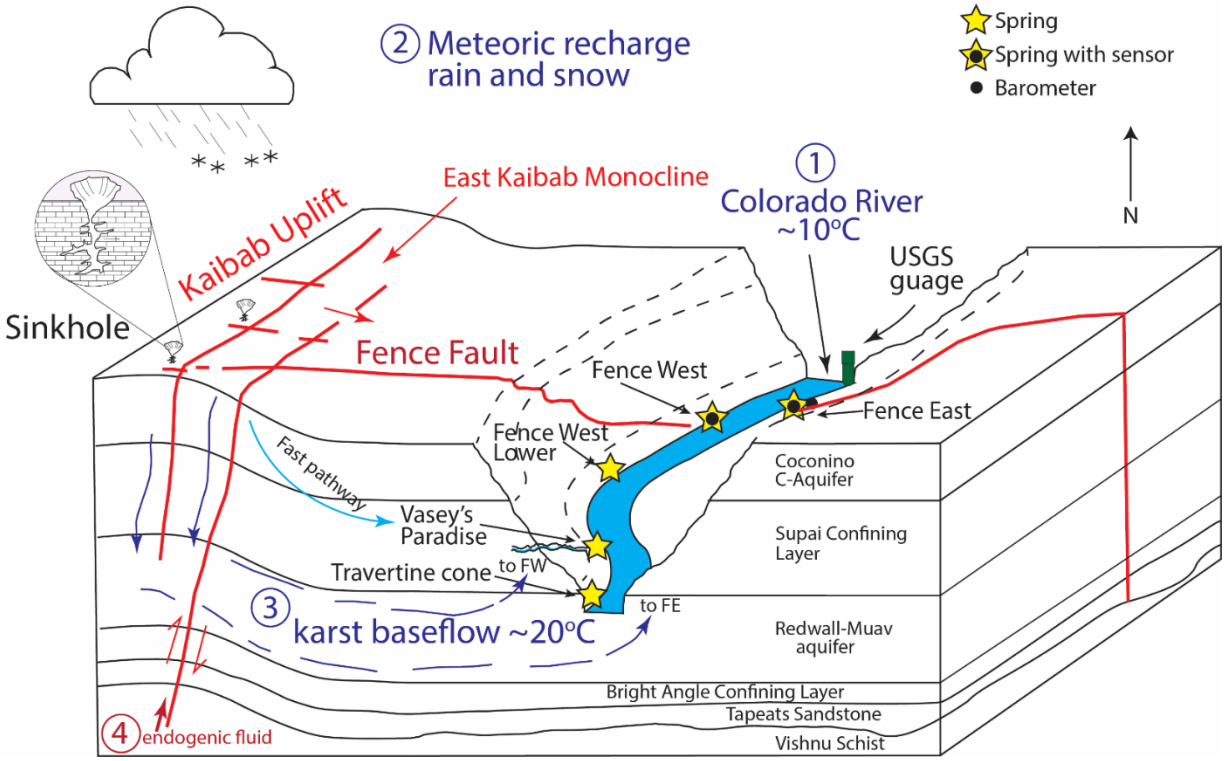

Figure 4. Block diagram showing springs investigated in this paper; main flowpaths from the Kaibab uplift recharge area are interpreted to be downward along faults and canyonward in the R-M karst aquifer. Fence West and East springs, located in the Fence fault zone, are fed by recharge from the Kaibab uplift as shown by stable isotope data. Numbers refer to endmember water mixing components to be evaluated: 1) snow and rain recharge from the high elevation

Kaibab uplift (T ~ 0-10 C), 2) Colorado River (T~ 10 C), 3) R-M aquifer baseflow (T ~ 20 C), 4) Small volume but geochemically potent endogenic fluid. The base of the active groundwater circulation is assumed to be shales of the Bright Angel Formation confining layer.

Roaring Springs and Bright Angel Creek that discharge Kaibab uplift-sourced recharge water from the Kaibab uplift, south into Grand Canyon (Fig. 1).

The source of recharge for the deep R-M aquifer regionally includes the high elevation uplands of the Coconino and Kaibab Plateau. Groundwater from the plateaus flow towards Grand Canyon, the hydrogeologic sink in the area (Monroe et al, 2005). Precipitation from snowmelt and monsoonal events is concentrated in the San Francisco Peaks areas south of the Grand Canyon (Bills et al., 2007; Crossey et al., 2009) and the Kaibab uplift north of Grand Canyon. The latter source region is of most importance for the Fence spring system. Water infiltrates volcanic rocks and the C- aquifer in the high elevations of the plateaus and descends through dissolution-enhanced faults, fractures and sinkholes (Huntoon 1974, 2000; Kessler 2002). Monsoonal events can lead to rapid changes in discharge, temperature and specific conductance in the unconfined parts of the karst systems, whereas these events are dampened in the confined basin karst systems, in some cases, to the point where they may not even be recognized (Huntoon, 2000; Jones et al., 2018; Solder et al., 2020). Groundwater sourced in the Kaparowitz hydrologic basin (Cooley et al., 1969) to the east of Marble Canyon was considered important by Huntoon (1981) but is not considered a major source for Fence springs in this study as discussed further below.

Overall, the Paleozoic sedimentary strata of Grand Canyon have relatively low permeability and hydraulic conductivity, due in part to the stratigraphy being primarily fine-grained, mudstone and sandstone, limestone and dolomite, as well as the confining nature of the alternating rock types (Fetter, 2000). As a result, faults, fractures, and folds play an

important role in the infiltration and transportation of groundwater (Kessler 2002). The faults and fracture zones act as conduits, providing lateral and vertical planes of increased permeability in areas with typically low hydraulic conductivity. The increased vertical permeability provides hydraulic continuity across confining beds within the Paleozoic section and serves to connect the plateau surface with the aquifers (Metzger, 1961; Huntoon, 1981).

Fence fault system

Fence fault is the northwestern fault system of the Eminence graben, a 6-mile-wide graben bounded on the southeastern side by the Eminence fault (Fig. 1C). Both are high angle normal faults, with displacement ranging up to 76 m that pre-dated the erosion of Marble Canyon (Huntoon and Sears, 1975). The Eminence graben is pervasively fractured by vertical joints in the inter-fault areas as shown in Figure 1C and this permeability increased groundwater circulation through the dropped down blocks prior to erosion of the canyon. The result is joint-controlled caves in the carbonates, present evidence of which is seen in caves up to 46m high on the canyon walls. The main modern counterparts that make use of these ancient circulation systems are the Fence spring system (Huntoon, 1981).

Fence fault is located at River Mile (RM) 30.5 in eastern Grand Canyon (river miles are measured downstream from Lees Ferry). At this location, multiple springs discharge near the Fence fault along subsidiary fractures and through karst breccias in the Redwall limestone on either side of the river (Fig 4). Spring vents are in the damage zone of the river-crossing Fence fault, on its downthrown side, not along its main strand. Fence East Spring (410 l/s; ~0.4 m^3/sec, or 14 cfs) is artesian and emerges at the edge of the river; it is emergent at low river stage (< 283 m^3/sec; 10,000 cfs) (Figs. 5A, B), and covered at higher river stages. Fence West Spring has lower flow (57 l/s; 0.06 m^3/sec; 2 cfs) and emerges mainly from alluvium near river level (Figs. 5C, D). A

network of much smaller spring vents on both sides of the river reflect the complex karst fracture system (Fig. 5E) but we concentrate on the highest discharge springs on the East and West banks. Springs downriver from the Fence fault that we compare hydrochemically to the Fence fault springs include Vasey's Paradise at RM 32 (Figs. 5F, G, H, I), and Travertine Cone springs and Hanging Gardens at about RM 34.5 (Figs. 5J, K), all reflecting discharge from the R-M aquifer in the downthrown region of the Eminence graben.

Methods

Water sampling

Water sampling was carried out following procedures set out in USGS National Field Manual for the Collection of Water-Quality Data (2006). Water samples for cations were collected in 60 mL High Density Polyethylene bottles (HDPE). Samples were filtered (0.45µm) and acidified using concentrated HNO_3. Samples for anions, alkalinity and $\delta^{18}O$ and δD isotope analysis were collected without headspace in 120 mL HDPE bottles.

Analytical methods

Water temperature, pH, and specific conductance were measured using an Oakton waterproof pH/CON 300 multi-meter. Major ion chemistry was analyzed using inductively coupled plasma optical emission spectroscopy (cations) and ion chromatography (anions) using standard methods, comparable to US EPA 200.7 and EPA 300.0 respectively. Carbonate alkalinity was measured by titration using standard methods comparable to 2320 ALKALINITY (American Public Health Association, 1995).

Figure 5A) and **5B**) Fence East spring bubbles up, artesian, into the Colorado River. **5C**) and **5D**) Fence West emerges from alluvium near river level and gets inundated by the river more easily than Fence East. The hydrochemistry of Fence East and Fence West springs are very similar and stable isotopes suggest both are sourced by recharge from the Kaibab uplift to the west. **5E**) fractured Redwall Limestone about 4 meters directly above Fence East spring shows the nature of the fractured karst aquifer.

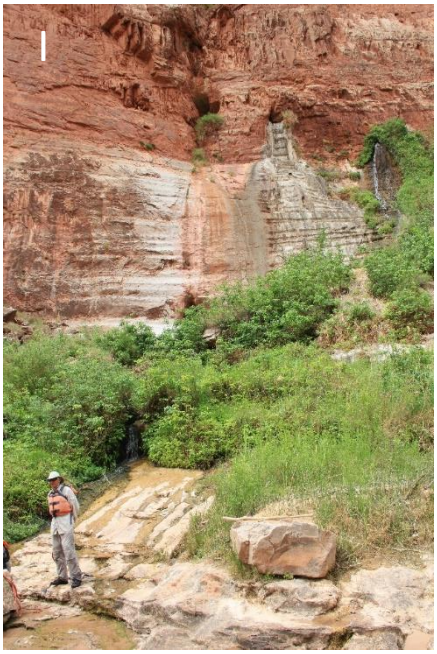

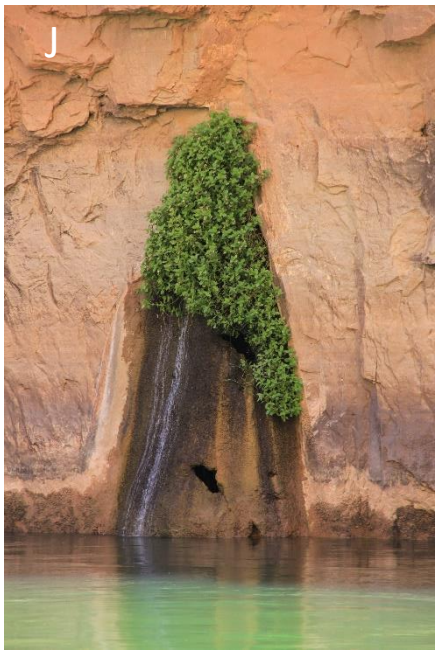

Vasey's Paradise at River Mile 32 has variable discharge: **5F**) May 17, 2019 has relatively high flow from two cave openings; **5G**) May 19, 2013, left vent had somewhat lower flow and slightly lighter stable isotope values; **5H**) May 22, 2016- left vent was dry and isotopes were most negative. I) May 19, 2018, both vents were nearly dry. **5J**) Travertine Cone is a small- discharge travertine- depositing spring that vents from the Redwall Limestone at river mile 34.6; **5K**) Hanging gardens also occur along seeps near River Mile 34.6.

These analyses were carried out at the Analytical Geochemistry Laboratory at the University of New Mexico (UNM). Isotopologues of oxygen and hydrogen were measured using cavity ring down spectroscopy (Picarro L1102-I) with methods comparable to Wassenar et al., (2012) at the Center for Stable Isotopes, UNM. Typical error bars for analyses are ≤0.2‰ for $\delta^{18}O$ and ≤0.4‰ for δD. Dissolved inorganic carbon (DIC) was calculated using the speciation model PHREEQC (Parkhurst, 1995).

Continuous monitoring

Unvented multi-parameter sensors were deployed for up to seven years and were downloaded or replaced annually. The parameters monitored were pressure (as a proxy for depth), temperature, and specific conductance. The sensors used were Solinst Levelogger Junior Model 3001 LTC. The sensor utilizes piezoresistive silicon with Hastelloy pressure sensor, platinum resistive temperature detector and 4-electrode platinum conductivity sensor. Calibration is not required for temperature and pressure as these come with lifetime factory calibration and are accurate to within 0.1 ^{o}C and 0.1% FS (0.5 cm). Calibration is required for conductivity and a 3-point calibration was carried out using conductivity solutions of 1,314 µS, 5,000 µS and 12,880 µS. For barometric corrections, a Solinst Barologger was used to record air temperature and atmospheric pressure; these were placed in shaded protected areas within tens of meters of the water sensors and were downloaded or replaced at the same times.

Fence East and Fence West springs were monitored. Barometric pressure was recorded in close proximity to Fence East. Resolution was initially set at 30-minute intervals and reduced to 60 minutes after the first year. Sensors were deployed within each spring below river level although the Fence West sensor became partly exposed at lowest flows of ~ 5,000 cfs (141 m^3/s). Data were downloaded in the field using a laptop and infra-red sensor USB connector, and saved as a CSV file. Corrections were made to delete anomalous readings, such as sensors

being removed for recalibration/download, anthropogenic interference, and to make depth corrections for barometric pressure and elevation. Management of continuous monitoring water data was carried out using Excel, Aquarius Time Series software, and Matlab. We also incorporated data from an adjacent USGS stream gauge that continuously measures stage, temperature, and specific conductance in the Colorado River at River Mile 30 (GCMRC, 2021).

Results of Geochemistry

Sample locations, field parameters, stable isotopes and water chemistry are listed in Tables EMS1 and EMS2, and chemistry data in Table 1. Geochemical results are presented for 9 locations: Fence East Spring (main), Fence West Spring, Fence West

Spring	Ca^{2+}	Mg^{2+}	Na^{+}	K^{+}	HCO_3^{-}	Cl^{-}	SO_4^{2-}	$\delta^{18}O$	δD
Fence East	176	48	219	21	530	356	249	-14.1	-101.7
FenceWest	138	41	174	17	488	257	176	-14.2	-101.4
Fence West Lower	31	20	2	1	197	4	12	-14.0	-100.2
CR-RM-34 (USGS)	60	19	54	3	168	37	167	-14.9	-114.9
Vasey's	47	20	2	1	231	2	5	-13.8	-96.9
[1]Hanging No.1	49	19	1	1	217	2	18	nr	nr
Travertine Cone	67	51	30	11	241	30	210	-13.9	-97.4

Table 1 – Mean chemistry data for springs, ppm and ‰.
[1]Data from Huntoon, 1981

Lower (Huntoon's, 1981, Diagonal Spring), Vasey's Paradise, Travertine Cone and Hanging Garden springs, Roaring Spring and Bright Angel Creek coming off the south side of the Kaibab uplift, and the Colorado River. Our data closely match older reported field and geochemical parameters for both of the main Fence springs. Water temperature is ~20 °C, specific conductivity ~2000 µS/cm. $^3He/^4He$ ratios in Fence East from previous work had an air-corrected value of ~ 0.1 R_A indicating a small but significant amount of mantle-derived volatiles (Crossey et al., 2006; 2016). Discharge

was estimated by Huntoon (1981) as 410 l/s (14 cfs) for Fence East spring and 57 l/s (2 cfs) for the highest discharge spring on the west bank (his Diagonal spring, but we use this value for Fence West spring). We did not verify these discharge estimates but a ~ 7 fold higher discharge for Fence East seems reasonable given its stronger artesian character and less susceptibility to influence by the river. Other spring vents likely are present below river level making discharge estimates approximate. With the exception of discharge, there is little variation in field parameters or hydrochemistry between the main Fence East and Fence West springs.

Figure 6A plots temperature (measured in the field) versus total dissolved inorganic carbon (DIC; computed using PHREEQC) and indicates two groups of spring waters. 1) Fence East and Fence West springs show relatively consistent and overlapping values. In field parameters, Fence East has means of: temperature = 20 ± 0.3 ^{o}C, pH = 6.7 ± 0.3, and specific conductance = 2157 ± 267 µS which is similar to Fence West mean values of temperature 21.1 ± 0.3 ^{o}C, pH = 6.7 ± 0.3, and specific conductance = 1796 ± 255 µS over about 17 years of campaign sampling (Table ESM1). Total dissolved inorganic carbon ranges from 2.63 – 17.88 mol/L with a mean value of 7.78 mol/L reflecting the carbonic nature of these springs. Crossey et al., (2009) reported that the DIC for Fence East was derived 45% from dissolution of limestone in the aquifer, 29% from organic sources (soil gas), and 27% from endogenic (deeply derived/ magmatic sources). 2) The other springs: Fence West Lower, Vasey's Paradise, Hanging Garden, and Travertine Cone are generally cooler, have higher pH, and lower specific conductance in terms of field parameters (Table ESM 1). Figure 6A shows that they are spread out in temperature at low DIC of 2.5 - 5 mol/L (Fig. 6A). The DIC values are more similar to Roaring Springs and Bright Angel Creek reflecting a larger meteoric component. A plot of Na vs Cl (Fig. 6B) also

distinguishes two main water groups with intermediate values suggesting mixing. Fence East and Fence West overlap, but Fence West has somewhat lower salinity; Travertine Cone has still lower salinity. The other springs have very low salts but the inset shows some spread along the mixing line.

Figure 6C is a Piper diagram (Piper, 1994) that shows major cations and anions projected into a central parallelogram; it defines the same two hydrochemical groupings. Water is Na + Ca – HCO_3 dominated compatible with the carbonic karst-nature of these waters with concentrations higher in all ions at Fence East and Fence West springs. Fence East and Fence West both show a small range of values and are indistinguishable from each other in their major ions. The other group of waters plot close to the left corner of the parallelogram which Crossey et al., (2006, their Fig. 2) interpreted to be close to a meteoric end member; these plot similarly to Roaring Spring and Bright Angel Creek that drain south off the Kaibab uplift. Fence West Lower, Vasey's Paradise, and Travertine Cone/Hanging Garden Springs plot closer to the meteoric end member but are displaced somewhat towards the other end member, suggesting mixing.

Field parameters and major ions vary from year-to-year. Temporal variation in the spring major ion chemistry for karst springs was minimal between the 1980's sampling of Huntoon, and in the stable isotope data of Ingram et al. (2001), compared to the 2002 to 2012 sampling reported in this study (Fig. 6). In more recent sampling, there is least variation in the high discharge Fence East spring, but, for example, the variation in discharge seen in Vasey's Paradise spring (Figs. 5F, G, H, and I) is reflected by different chemistries. Most notably, in 2016, the conservative tracer Cl (9.8 ppm) is several times its values from other years (1.4 to 2.0 ppm) and is also ~100 ppm higher that year in

Fence East and Fence West (454 and 337 ppm respectively) that year relative to mean values of 347 and 257 ppm respectively (Table ESM2).

Stable isotopes of δD and $\delta^{18}O$ were analyzed (Fig. 7) from the same set of 9 waters. The inset to Figure 7 shows that the stable isotope values for all Grand Canyon springs resolve into two groups. Samples have a range of values that plot generally along the Global Meteoric Water Line (GMWL) with North Rim- derived groundwater more negative than South Rim-derived groundwater due to higher elevation of recharge (Ingraham et al., 2001) and differences in type of recharge (snowmelt versus monsoonal; Solder et al., 2020), and both are distinct from the Colorado River. The Fence spring system is similar to, but more depleted in $\delta^{18}O$ and δD, than waters derived from the Kaibab uplift such as Roaring Springs and Bright Angel Creek. A close inspection of the Fence spring values in the main part of the diagram shows that values for δD and $\delta^{18}O$ range from -13.48 to -14.98 ‰ and -96.84 to -103.72 ‰ respectively for these waters. The springs separate in a similar way for the field parameters and major ions of Figure 6. Fence East and Fence West Springs have more variation in δD: from -100 to -105 ‰ with $\delta^{18}O$ from -15 to -13.5 ‰, whereas the more meteoric-dominated springs have generally less negative δD ~ -92 to -97 ‰ with $\delta^{18}O$ of -13 to -15 ‰.

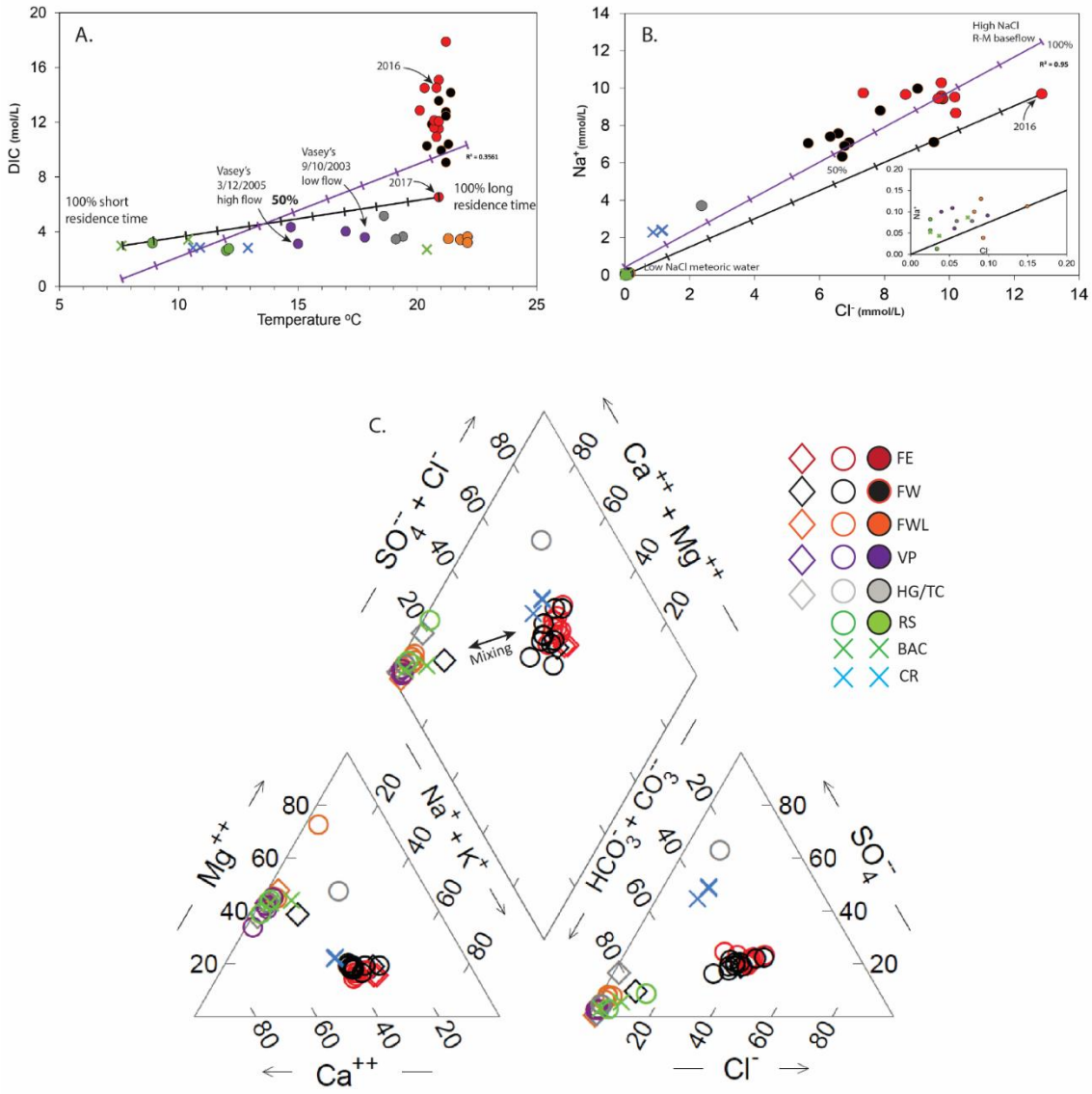

Figure 6A) Na and Cl content of springs; low NaCl waters in the lower left corner (see inset) includes more meteoric springs; high NaCl waters are from Fence East and Fence West springs. Mixing lines are shown relative to regressed data (purple) and selected potential end member samples (black). **6B**) Field temperature versus dissolved inorganic carbon (DIC; calculated from PhreeQc; Parkhurst, 1995). Temperature is interpreted to be a proxy for residence time in the R-M aquifer and shows a spread of values; DIC shows two different water chemistry groupings. Mixing lines are shown relative to regressed data (purple) and selected potential end member samples (black). **6C**) Piper diagram of major element analyses of springs in the Fence fault area sampled from 1981 to 2019. Two distinct geochemical groups are evident in the parallelogram: 1) Fence East (red) and Fence West (black) overlap supporting Huntoon's (1980; his data are plotted as diamond symbol) conclusion of connectivity, 2) More meteoric values are seen in Fence West Lower (orange), Vasey' Paradise (purple), Roaring Springs (bright blue) and Bright Angel Creek (dark blue). Travertine Cone and Hanging Gardens (gray) each are fresher than FWL, suggesting mixing. The Colorado River (blue) is hydrochemically different than the springs in its anions.

Temporal variations are noticeable, for example 2016 $\delta^{18}O$ values are more negative in Fence East (2 samples), Fence West, and Vasey's Paradise (no sample for FWL). Potential mixing is suggested by the intermediate locations for Fence West Lower and Travertine Cone/Hanging Gardens between the more strongly meteoric values of Roaring Spring and Bright Angel Creek and the steady values at Fence East and Fence West springs. Using multiple tracers, Figure 8 plots log [1/Cl] versus δD. This plot shows a separation between the Fence East and Fence West springs, which (now in log scale) show a slight variation with Fence East having higher [Cl] (lower 1/[Cl]) than Fence West, although they generally overlap. This separation in 1/[Cl] suggests a higher-volume contribution of meteoric component in Fence West, as is also seen for the other springs west of the river. The more meteoric springs spread out considerably, again suggesting different degrees of mixing.

Interpretation of Geochemistry

Spring waters exhibit two main groups. Fence East and West springs are similar to each other but differ from nearby springs further down river, and both differ from the Colorado River. This reinforces the conclusion of Huntoon (1981) that the Fence East and West springs are connected hydrologically within the confined karst aquifer below the Colorado River and are not in communication with river water. All of these springs discharge from the R-M aquifer at depth in the Grand Canyon such that variations in water chemistry can provide information about: 1) the nature of recharge water, 2) water-rock interactions within the aquifer, and 3) the nature of the flowpath.

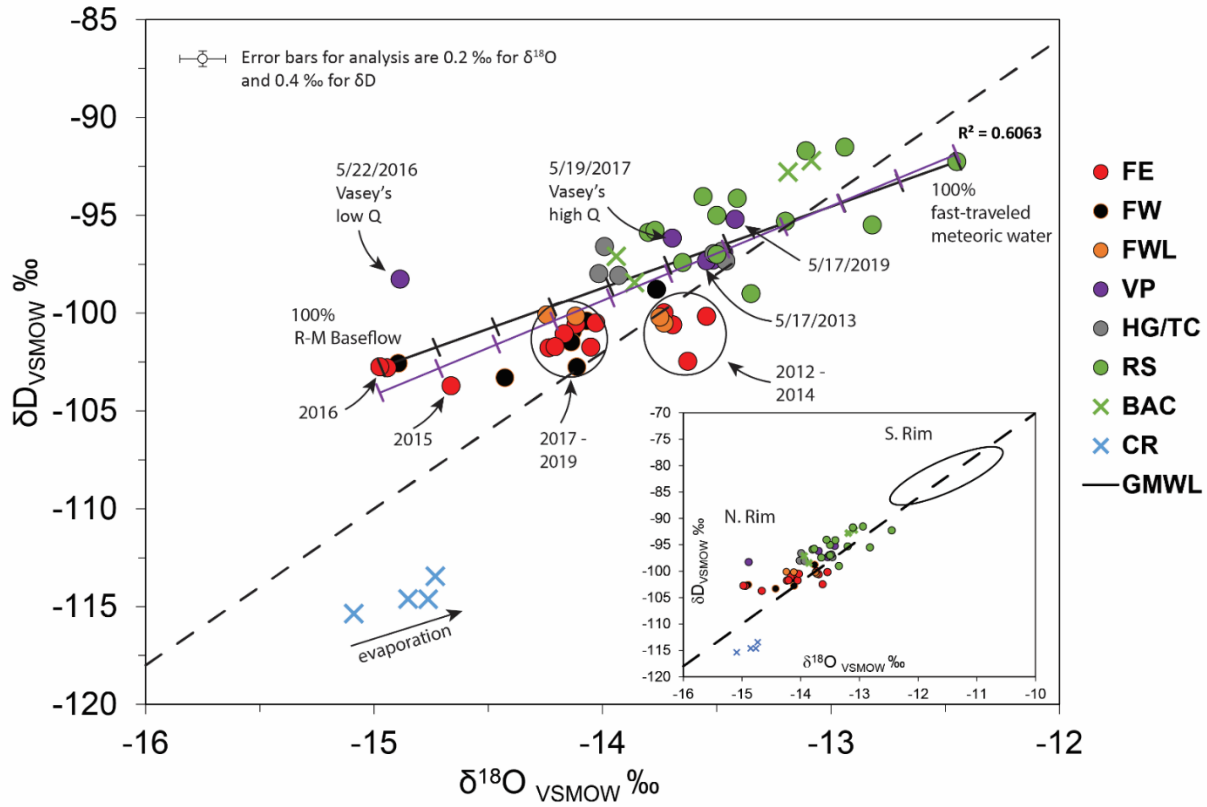

Figure 7. Stable isotope data for springs in eastern Grand Canyon. GMWL is the Global Meteoric Water Line (Craig, 1961). Inset shows distinction between North Rim and South Rim waters. Main figure shows that Fence East (FE) and Fence West (FW) springs have overlapping values and are distinct from Vasey's Paradise (VP), the Colorado River (CR), springs further downstream (FWL, TC, and HG), and Roaring Springs (RS) and Bright Angel Creek (BAC). Mixing is best documented at Vasey's Paradise where values are similar to Fence springs at low flow (larger karst base flow contribution) and similar to Roaring Springs/ Bright Angel Creek at high flow (smaller fast flow contribution). Travertine Cone plots along this mixing trend. These data suggest that water from the Fence spring system is derived dominantly from the Kaibab uplift. Mixing lines are shown relative to regressed data (purple) and selected potential end member samples (black).

To understand mixing of waters and to parse these different variables that affect hydrochemistry we apply multiple tracers that are sensitive to different aspects. Temperature at the spring vent is a proxy for residence time in the aquifer as meteoric recharge progressively heats to rock temperature. Solute types and concentrations are proxies for rock type and

duration of water-rock interaction. Stable isotopes are a proxy for the source of water (recharge). All of these parameters are conservative tracers with respect to mixing of waters, and karst baseflow has less variability than fast-traveled inputs.

The temperature versus DIC plot (Fig. 6A) shows relatively steady temperature for the Fence East and Fence West springs at about 21 °C that we interpret to be the karst baseflow temperature for this region. This temperature reflects equilibration of groundwater with rock temperature at the stratigraphic depth of about 800 m (Fig. 2) for a geothermal gradient of 25 °C/km. The high DIC for these waters is a measure of their carbonic nature and reflects input of ~ 27% deeply derived CO_2 and 29% soil-derived external carbon that makes the groundwater more corrosive and leads to an additional ~ 45% of the CO_2 derived from dissolution of limestone in the aquifer (Crossey et al., 2009). A mixing line based on the temperature variation suggests that temperature variation in Fence and Fence West springs may reflect up to 10% input of cooler short residence time water and up to 10 mol/L dilution of the larger reservoir karst baseflow by meteoric water inputs. The more marked variation in the other springs suggests that Vasey's and Roaring springs temperatures reflect ~30% temperature variation due to temporal changes in the proportion of fast traveled versus matrix flow at different sampling times. The dominant ions, Na + Ca – HCO are found in all samples and reflect water-rock interactions in the limestone aquifer; however, Fence springs have markedly higher ion concentrations, in particular Cl and SO_4 that are interpreted to be characteristic of a deep karst, slow flow end member that has exhibited steady values for at least decades (Figs. 6B, 6C).

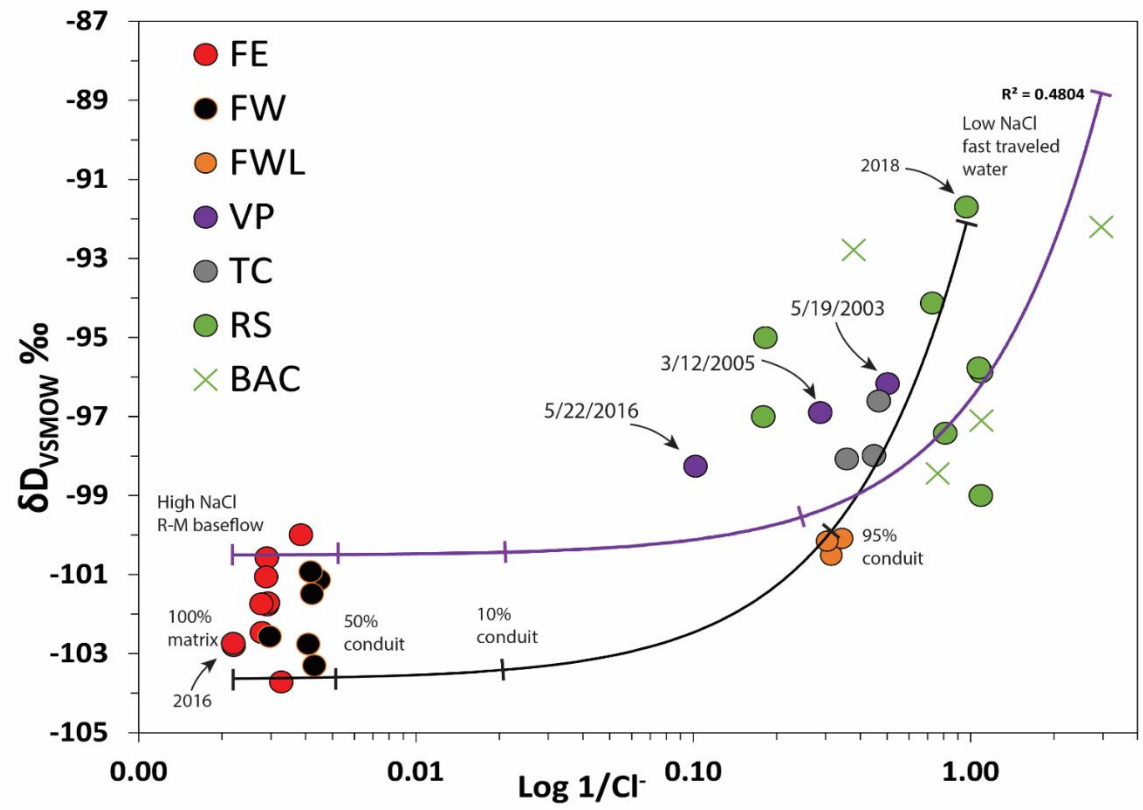

Figure 8. δD vs 1/[Cl]. Clustering of Fence East (FE- red) and Fence West (FW- black) shows similar source and are considered to reflect the karst fracture flow (base flow) end member. Fence West Lower (FWL- orange) has similar isotope values, but lower [Cl-] (high 1/[Cl-]) similar to Vasey's Paradise. This suggests greater contribution from a fast-traveled end member with some contribution from base flow. Vasey's Paradise variation year-to-year shows a mixing line between the base flow end member (at the 2016 time of lowest discharge) and the fast traveled end member (at high discharge). Mixing lines are shown relative to regressed data (purple) and selected potential end member samples (black). Mixing line reflects log values on X axis.

In contrast, as evidenced by the dye tracer test, fast flow of meteoritic waters from the Kaibab Plateau surface to springs can be on the order of months (Jones et al., 2018). This suggests the chemistry of the more meteoric water springs (Vasey's Paradise, Fence West Lower, Travertine Cone/Hanging Gardens) is controlled by variable amounts of the faster flowpath, more meteoric, waters mixing with the deeply sourced karst component. For comparison of these mixed springs: Fence West Lower has stable isotopes closer to the Fence system, but lower specific conductance; Vasey's Paradise has lower specific conductance and temporally variable

stable isotopes; and Travertine Cone and Hanging Gardens show heavier $\delta^{18}O$ and lower specific conductance. All of these variations suggest mixing via dilution of the Fence spring R-M karst baseflow end member with variable meteoric contributions from the Kaibab uplift that arrive via fast pathways (conduit flow) with an end member approximated by Roaring Springs and Bright Angel Creek.

Isotope values of δD and $\delta^{18}O$ (Fig. 7) vary between the same end members. Fence East and West springs are similar and form an overlapping field that is distinct from other nearby Marble Canyon springs. Major conclusions of this paper is that both Fence East and West springs are similar to each other, but are markedly different than South Rim springs and the Colorado River, and that the similarity between Fence East and Fence West supports that the sub-river circulation model of Huntoon (1981). Fence spring $\delta^{18}O$ values are among the most negative values in the entire spectrum of Grand Canyon waters. Given that more negative values are associated with colder, higher elevation recharge (Sharp, 2017; Solder et al., 2020), we infer that both springs were sourced from Kaibab uplift winter precipitation of the North Rim, and that groundwater flow is from the west to east, opposite to Huntoon's (1981) model.

Using simple linear mixing models provides a way to quantify the mixing fraction of conduit, fast flow vs matrix, longer residence time water for the Fence springs. Figures 6A, B, 7 and 8, all have a mixing line (black) which uses a representative sample from Fence springs and Roaring springs as end members, as well as a linear regression line (purple) which utilizes all the data. Figure 6B (using Na-Cl), figure 7, (using stable isotopes), and figure 8 (combined chloride and deuterium) all show up to 40-50% fast flow contribution for the Fence springs, whereas figure 6A (using temperature and DIC) shows less than 10%. Figure 6A shows two separate groups rather than mixing with a mixing line (in temperatures) connecting the non-Fence springs; this reflects variable residence time which, even for the conduit, fast flow water is on

the order of month/s (Jones et al, 2018), and provides time for temperature equilibration within the aquifer. Although all the springs are mixed and no true end members may be sampled, the endogenic component for example, the mixing lines shown using the same extreme values within our data, are similar enough that they suggest the combined geochemical natural traces provide approximate mixing proportions of different water sources and pathways within the aquifer.

Figure 9 shows a schematic cross section that revises the model of Huntoon (1981) to show that most of the recharge is derived from the Kaibab uplift of the North Rim areas, to the west, with no evidence for waters from the South Rim areas or from areas to the east of Marble Canyon. There are two hydrochemical groups of springs: 1) the Fence spring system is considered to reflect a slow base flow near-end member for the karst aquifer; 2) springs located off the fault and are interpreted to be a mixture consisting of fast-traveled meteoric water with slow-traveled karst waters. In our hypothesis (Fig. 9), the greater discharge and artesian character of Fence East spring may be a consequence of subsurface karst plumbing (i.e. derived from flowpaths deeper in the aquifer) rather than different sources with different heads as modeled by Huntoon (1981). In summary, all the springs are R-M karst aquifer waters, but their hydrochemistries vary spring to spring, even in a small area, and time to time at the same spring (e.g. Vasey's Paradise) due to mixing of different waters traveling in different flow paths.

Temporal variations in each of these datasets are considered to be related to spring discharge. This, in turn, is related to the relative proportion of each mixing component, the most variable/changeable being meteoric water. For example, offset of Vasey's Paradise to lighter $\delta^{18}O$ and higher [Cl] is expected at times when karst base flow (for example in Fig. 5I) dominates over faster-traveled meteoric components (Fig. 5F). At longer timescales, it is possible that differences between the $\delta^{18}O$ = -13 to -13.5 ‰ for modern Bright Angel Creek and Roaring

Springs waters, compared $\delta^{18}O$ = -14 to -15 ‰ for Fence springs may reflect a larger (more negative) snowpack component in older waters (e.g. hundreds or thousands of years) of the karst base flow than in the modern karst recharge.

Figure 9. Hydrogeological model showing: 1) derivation of Fence East and Fence West springs from the Kaibab uplift with no mixing with Colorado River water and no known input from the east. 2) Fence springs are close to an end member for karst base flow in this region which we view as the groundwater pool residing in the downthrown block of the Eminence graben. 3) Small volume endogenic fluids ascend along fault and accumulate in the pool as shown by

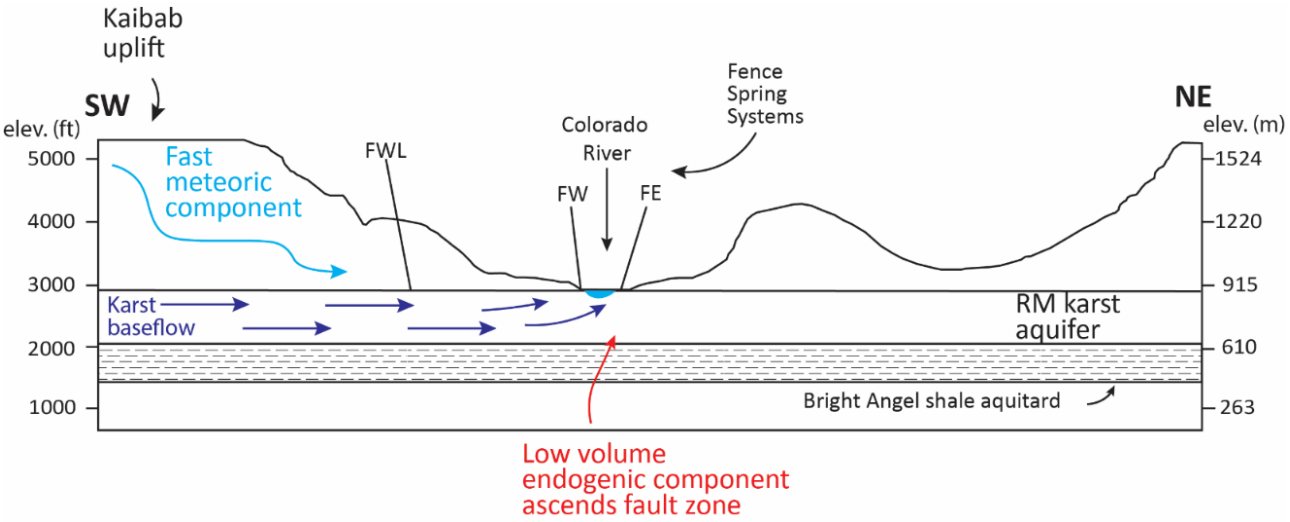

mantle derived helium and high endogenic carbon. 4) R-M springs away from the Fence fault zone are dominated by fast-traveled meteoric water from the Kaibab uplift that mixes into the karst base flow (Fence springs).The artesian character of Fence East reflects its deeper flowpath.

These data are consistent with dye tracer studies (Jones et al., 2018) in that the observed fast response time of meteoric recharge events (especially monsoon storms) seen in some R-M aquifer springs documents the potential for mixing of different end member waters and pathways to produce a wide range of spring compositions. The dye tracer study also documents a direct fast connection (days to months) between snowmelt recharge and discharge for a portion of the water at Vasey's Paradise (Jones et al., 2018).

Results of Continuous Monitoring (7-year record)

The result of continuous monitoring of the main springs of the Fence spring system is presented in two parts: 1) description of the 7 years of data streams for Fence East and Fence West springs; 2) a detailed look at the spring response to the high-flow experiments (HFEs). Fence East erupts upwards with considerable artesian force at the edge, and directly into the Colorado River (Figs. 5A, B). Its probe is submerged at all times within the upward bubbling spring about 1 m below the surface. Fence West is near the end of a sand bank (Sand Dune camp) (Fig 1D); the spring forms a relatively calm pool (Figs. 5C, D) and the probe is located at the spring vent that is close to river level and becomes partly emergent at lowest river stages.

Figure 10 shows a schematic view of the placement of our probes in the main Fence springs in the context of the varying dam-controlled river stages and the groundwater flowpath model inferred from the hydrochemistry of the prior section of the paper. The response of the sensors was controlled in part by river stage, especially by the HFEs, their total duration, and ramp-up and ramp-down curves (Table 2 and Fig. 10). A further factor controlling the response is the difference in discharge of the two springs. Fence East has the higher discharge rate, approximately 410 l/s (14 cfs) compared to 57 l/s (2 cfs) for Fence West (Huntoon, 1981). As a consequence, Fence West had a more variable, rapidly fluctuating probe record than Fence East due to river stage variations. Below we summarize spring response in terms of the three measured parameters: depth, specific conductance, and temperature.

Year	Duration (days, hours)		River Discharge (cfs)	
	total	peak	max	pre/post HFE
2012	3 d 19 h	24h	43000	7 to 9000
2013	5d 5h	96h	37000	7 to 9000
2014	5d 5h	96h	37500	7 to 9000
2016	5 days	96h	36500	7 to 9000
2018	3d 10 h	60h	38100	6500 to9000

Table 2 – HFE comparison data

Figures 11 and 12 show full data streams, by parameter, for Fence East and Fence West springs, respectively, for about 7 years. Descriptive statistics are in Table 3. Gaps in the record are due to either failure of the sensor, years for which we could not obtain Park permits, and/or limited

Spring	Discharge Q (cfs)	Specific Conductance (µS/cm)			Temperature (°C)
		max	min	mean	Max
[2]Fence East	6500	2540	~500*	1933	20.6*
[2]FenceWest	20	2340	~350*	1310	21.1*
[1]Fence West Lower	900	378	338	348	22.1
USGS gauge -RM-34	5428 - 44644	1337	627	740	15.4
[1]Vasey's Paradise	2500	469	268	368.5	19.4
[1]Hanging Graden	30	366	366	366	18.7
[1]Travertine Cone	nr	414	346	380	19.4

Table 3 – Spring parameter descriptive statistics
* These are interpreted values from the data. There are higher/lower values in the data, but these occur when the sensor is above river level.
[1]Values take from spot readings using handheld instrument
[2]values take from sensor

memory for new readings. Some variations in the data may be due to differences in deployment, such as installing the sensor in a slightly different location, but times of data downloads (red arrows in Figs. 11 and 12) in general do not correspond to changes in the time

series arguing that the data record real variations at the probe due to spring- river interactions.

During early deployment (2013-2016), the probe at Fence East was in a more stable position

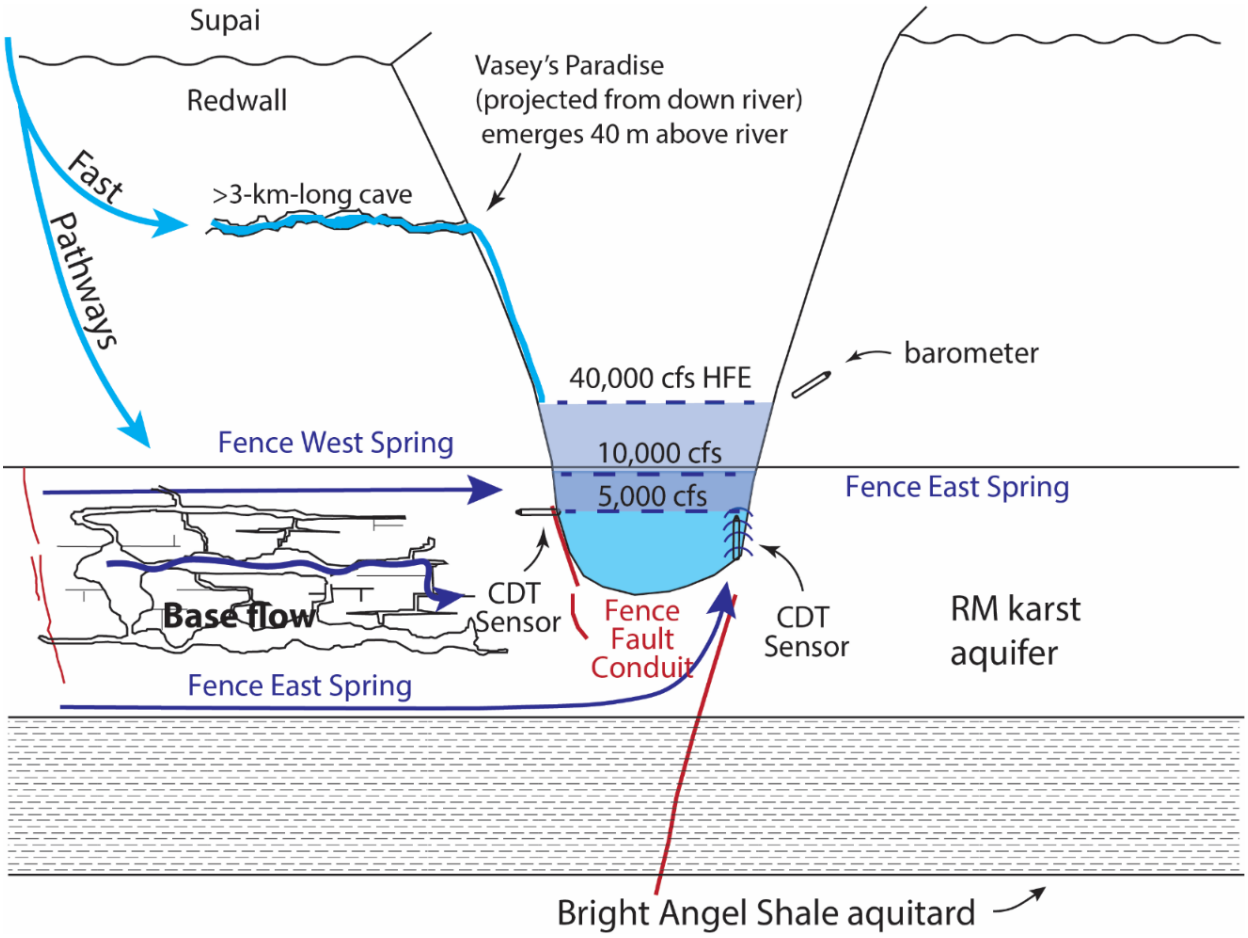

Figure 10. Detail of the inferred flowpaths for spring waters and position of probes. Fence West probe is near the level of the Colorado River at ~ 10,000 cfs stage; Fence East spring is a bubbling spring that vents into the Colorado River and has an artesian head that displaces river water such that the probe does not feel river temperatures at the level of the probe (~ 1 m below 10,000 cfs levels) except at high river stages when the river pressure overcomes the artesian pressure. Fence East and Fence West springs reflect karst base flow for Marble Canyon, east of the Kaibab uplift. Vasey's Paradise spring is projected into this cross section from down river; it emerges from the Redwall 40 m above the river and shows fluctuating flows related to fast pathways. The ~40,000 cfs High Flow Experiments were dam releases that acted as slug tests to determine aquifer characteristics (see text).

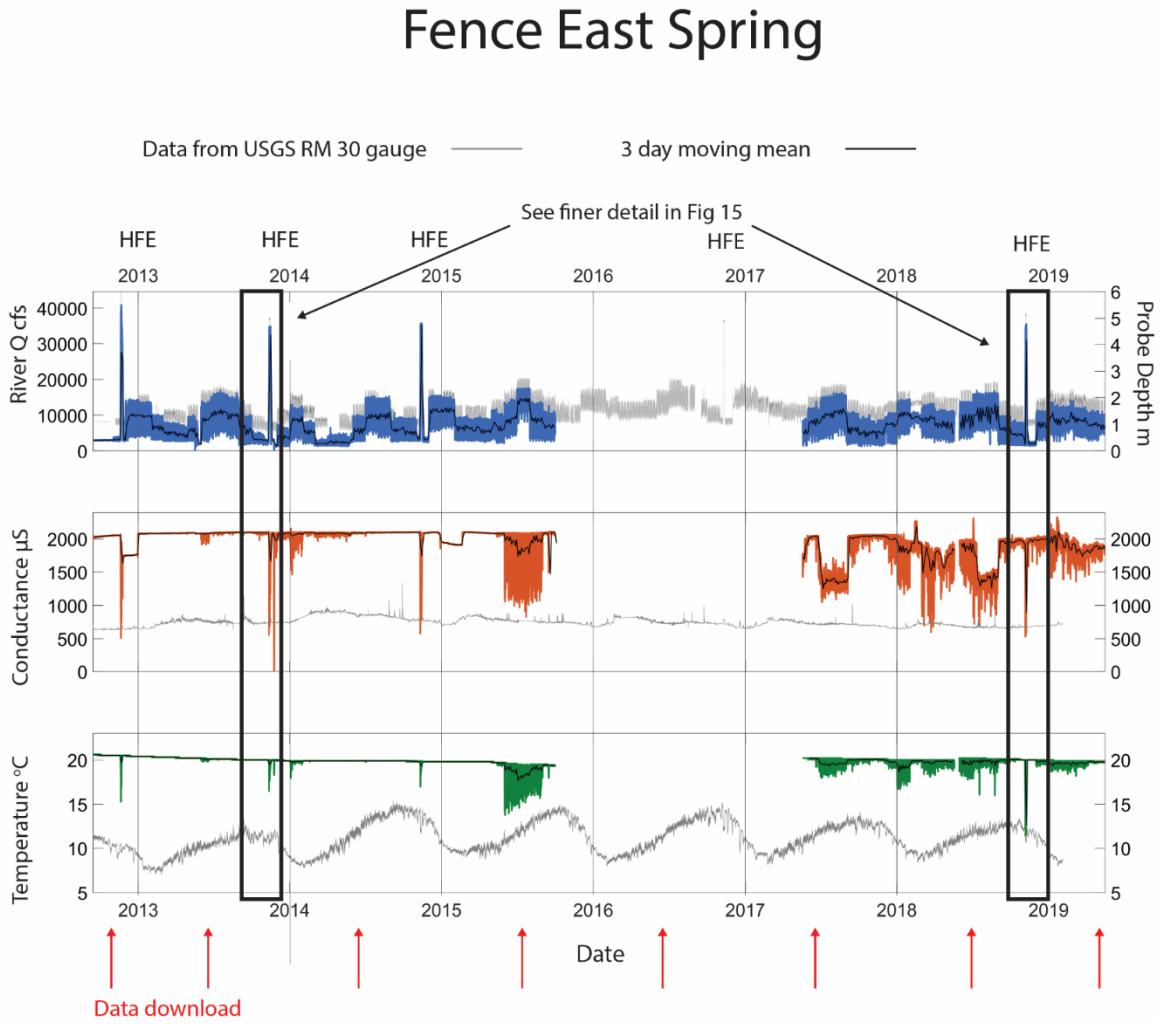

Figure 11. Fence East: Continuous sensor data from 2012-2016 and 2017-2019. A) Pressure sensor (blue color; depth on right axis) is a direct response to river stage (gray curve; cfs on left axis as measured at the USGS gauge about one river mile upstream. River stage fluctuations occur at daily and weekly cycles depending on electricity demand and dam operations (including 4 high flows experiments (HfEs). B) Conductance record (blue) shows trend of progressive decrease of ~ 100 us over the 7-year record; river conductance (gray) is from the USGS probe. HFEs correspond to sharp decreases in conductance due to river water dominance at the level of the probe. Note increase in short wavelength conductance variations in 2017-2019 that may reflect decrease spring discharge. C) Temperature record (green) shows steady maximum temperatures and an overall decrease in baseflow maximum temperature of 1.5 C over 7 years. Early years are characterized by very stable values. River temperatures at the USGS proble (gray) show seasonal variation not seen in the spring. High flow experiments cause short term dramatic decrease in recorded temperature reflecting river water pushing down on and overwhelming the artesian spring. Note that increase in short wavelength T variations in 2017-2019 may reflect decreased spring discharge. The time of downloads is shown by red arrows; in general, these do not correspond to major changes in the time series. Black lines are the 3-day running means.

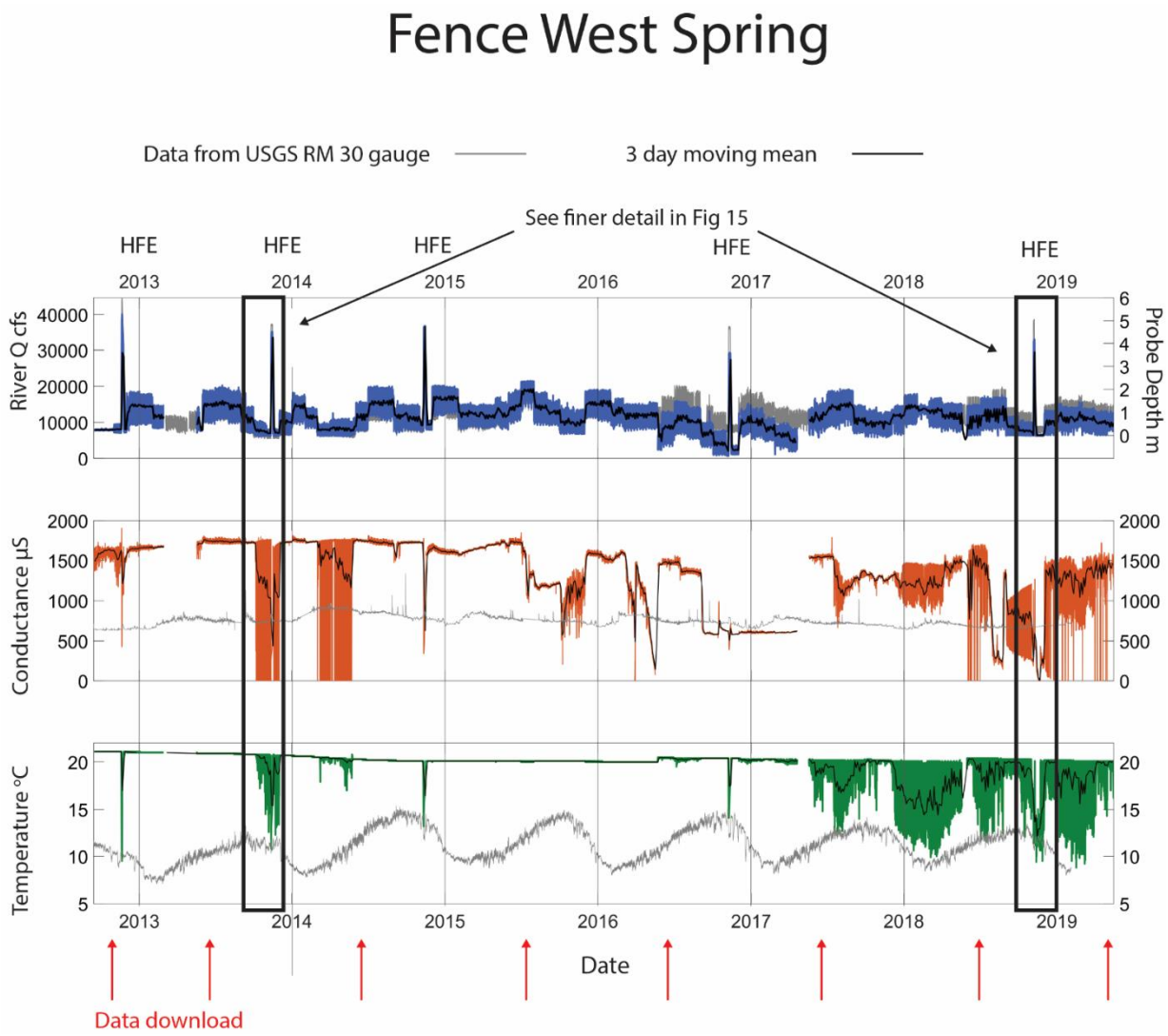

Figure 12. Fence West: Continuous sensor data from 2012 – 2019. A) Pressure sensor (blue color; depth on right axis) is a direct response to river stage (gray curve; cfs on left axis as measured at the USGS gauge about one river mile upstream (ref), including during 5 high flows. B) Conductance record shows overall trend of decrease of ~ 100 µS; high flows correspond to sharp decreases in conductance due to river water dominance. Note that increase in short wavelength conductance variations in 2017-2019 could reflect decrease in discharge. C) Temperature record shows an overall decrease in base temperature of 1.5 C over 7 years, with periods of most stable values in 2012- 2013 and 2015 - 2017. High flow experiments cause dramatic decrease in recorded temperature reflecting river water flooding the river-level spring vent. Increase in short wavelength temperature variations in 2017-2019 could reflect decrease discharge.

with the sensor fixed top and bottom to the wall of the spring whereas during 2016-2019 deployment, the sensor was freer to sway, but was kept approximately upright by the vigorous spring upwelling. This deployment variation could have allowed more mixing with river water and hence times when specific conductance and temperature approached river values, e.g. mid-2015 and numerous times after 2017. However, the sensor at Fence West was positioned more to the river's side, in a passively emerging spring pool in the rocks near river level and it too shows increasing signal variability in later years, especially in temperature. It had periods above river level as seen in depth, which becomes negative, and also seen in both specific conductance and temperature which approach or reach river values. Both springs were shielded from the full impact of the change in river stage and velocity, being close to the canyon walls, and we argue that trends seen in both springs are unlikely to be due to deployment variables.

Measured depth values (right hand Y-axis) are read from the location of the sensor, zero, to the water surface and record relative depth variations. The depth of the sensor co-varies with river discharge (left hand y axis, gray curve) that varies between 5,000 and 20,000 cfs (141 to 566 m^3/s) except during the high-flow experiments (HFEs). A "rating curve" between depth and river stage was developed by USGS probe located just upstream and this is also shown in Figure 12 by the left hand axis and gray curves. The controlled releases from Glen Canyon Dam cause stage variations at daily, weekly, and seasonal timescales depending on the need for energy generation from the hydroelectric power station at Glen Canyon Dam. Because the sensors were deployed below river level, the dominant signal in the depth data is the variations in river level, even for Fence East spring that remains artesian and does not mix with river water until high river stages. The depth data illustrate times of more pronounced river influences on specific conductance and water temperature.

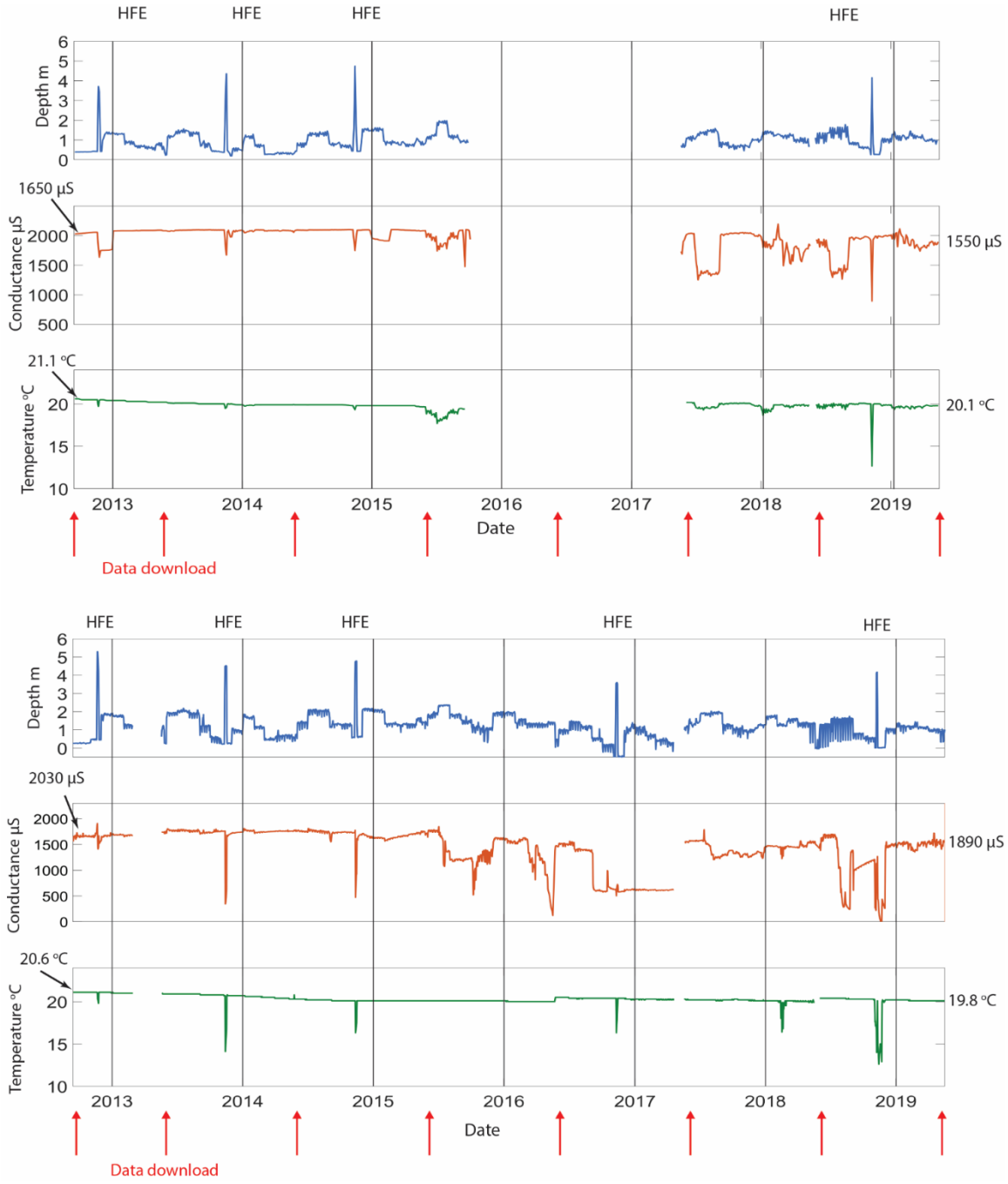

Figure 13. Fence East (upper) and Fence West (lower) daily maximum values. Maximum values are considered to be closest to spring values and representative of karst baseflow component. Long-term decrease in both specific conductance and temperature across the 7 year period is interpreted to reflect decreased discharge of both springs.

Both the specific conductance and water temperature data show periods of relatively constant/invariant values punctuated by events, which show large swings in values, especially during the HFE events. Because river water interaction lowers specific conductance and temperature, the maximum daily values of both parameters are taken to most accurately record spring values and variability. Figure 13 shows, over the total 7 year timespan of the data, that the maximum value of specific conductance observed during stable recording intervals decreases in both springs by ~100 µS and that temperature decreases by ~ 1.5 ^{o}C, a 5 and 7 % decrease respectively. Cyclic variations are controlled by river discharge, there is no observed seasonal variation in specific conductance or temperature.

Interpretation of Continuous Monitoring (7-year record)

The close correspondence of oscillations of mean depth with mean river stage is seen in both Fence East and Fence West springs as shown by the comparison to the USGS probe in the Colorado River located about one km upstream. High river stages are recorded regularly in the winter months of December to February and in the late summer of June to August.

Variations in specific conductance and temperature during normal flow show two patterns. First, we interpret the times of increased daily/weekly fluctuation in both parameters to be related to variations in river level. For Fence East (Fig. 11), times of lowered values and increased fluctuation in specific conductance and temperature occurred during high-flow experiments and these fluctuations increased in frequency and amplitude during the high stages of HFEs after ~2015. These are interpreted to reflect inundation of the springs by river water during high-flow experiments and, for non-HFE times, swaying of the sensor in turbulent upwelling spring water that may mix with some river water. Fence West times of fluctuation (Fig. 12) also correspond to HFEs, but in contrast to Fence East, fluctuations during non-HFE

times correspond most commonly to low river stages when the sensor on occasion was near or above river level, exposing the sensor to the atmosphere. Nevertheless, the increased fluctuations both during and between HFEs after 2017 in both springs suggests a decrease in spring discharges that allows the probes to be more frequently affected by river water.

Figure 13 shows the most significant long-term signals observed over the 7-year timeframe. The first impression of steady long-term maximum temperature and maximum conductance measurements of ~20 ^{o}C and ~2,000 µS/cm for both Fence East and West springs, with no seasonal variability, supports the idea that these springs provide baseline values for the R-M karst groundwater reservoir in Marble Canyon, east of the Kaibab uplift. A closer look reveals a progressive decrease in maximum value of both specific conductance and temperature in both springs. Because we interpret the maximum specific conductance to track the base flow of the karst aquifer, we interpret this to reflect a long-term change in the regional base flow of the R-M aquifer for Marble Canyon.

A possible explanation is that this decrease in maximum specific conductance and temperature in both springs is a result of a decrease in the discharge of the karst long-flowpath R-M base flow. Our reasoning is that, because geochemical data suggest variable mixing of meteoric waters with karst base flow in the adjacent springs, this decrease in temperature and specific conductance in the base flow springs can be explained by a larger proportion of fast-traveled meteoric component in this part of the R-M aquifer. Yet, this period of time (2012-2019) also seems to have been a time of increasing temperature and decreasing recharge off the Kaibab uplift (Tillmen et al., 2020) as measured by snowpack depth and climate modelling. Figure 14 shows mean yearly snow water equivalent from the Bright Angel station (NRCS, 2021), close to the Grand Canyon North Rim Visitor's Center, with a decreasing trend since monitoring began at the station began in 1947.

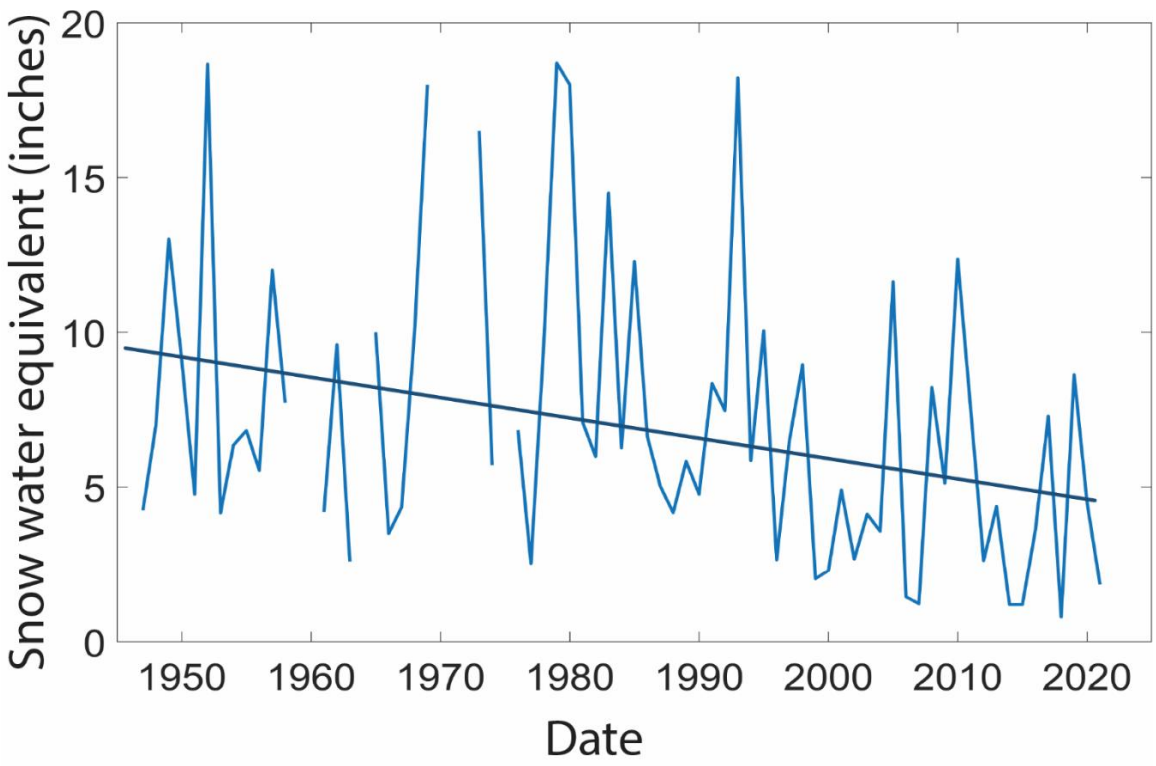

Figure 14. Snow water equivalent mean yearly values from the Bright Angel Station, north rim, Grand Canyon - Regression line shows a decrease in snowpack across the record period. This is considered to represent a decrease in the fast travelled, meteoric component in the karst aquifer.

Thus, decrease discharge in the base flow may have been caused and accompanied by simultaneous decrease in meteoric recharge to both fast and slow pathways resulting in an increased proportion of meteoric to base flow components at Fence springs. This decreased discharge may be supported by the greater fluctuation especially in specific conductance, but also in temperature, seen post ~ 2015 in Fence East spring. Specific conductance and temperature in both springs are demonstrably lowered during high river stages of the HFEs (40,000 cfs, 1,133 m^3/s) but were unaffected in 2013-2015 by normal dam-controlled river fluctuations of 5,000 to 15,000 cfs (141 to 425 m^3/s. In contrast, after 2015, the same river fluctuations caused frequent lowering of specific conductance and temperature maximum

values at stages below 10,000 cfs (283 m^3/s). This might have been caused or amplified by the less stable deployment of the Fence East probe allowing more mixing with river water, but because it is observed in both springs, and in both specific conductance and temperature, we infer that karst base flow has decreased such that the springs were more easily infiltrated by river water below a threshold stage of ~ 10,000 cfs (283 m^3/s).

Alternatively, the observed long-term decrease in specific conductance and temperature could reflect a very old age for the base flow waters that may have been recharged during a cooling period much earlier in the 1900s or even in cooler climate regimes farther in the past. For example, winter snowpack may have been greater several decades ago than now, and early Holocene climates were cooler and wetter (Woodhouse et al, 2010). The implication of this hypothesis of older recharge would have less dire societal implications for the karst base flow. But the subtle variation in geochemistry seen in stable isotopes among Fence subsidiary springs, the temporal variation and indication of mixing trends in Vasey's Paradise and other downstream springs, and the increased fluctuation of temperature and conductance in both springs in 2013-2014 compared to 2016-2019, during a time of warmest summer temperatures, decreased Bright Angel Creek base flow, and lowering snowpack, lead us to favor the decreasing base flow hypothesis.

Results from the High-Flow Experiments (HFEs)

Our sensors were in place during five HFEs (Fig 15). A USGS probe is located ~ 1 km upstream that also recorded river stage (height of river surface) and calculated discharge, temperature, and conductivity in this part of the river corridor (gray lines on the depth curves of Fig. 15). Each high-flow experiment had a somewhat different hydrograph, but in general, at the location of the installed sensors, the river raised quickly from < 1 m (~ 5,000 cfs, 141 m^3/s) to > 5 meters

depth (~ 40,000 cfs, 283 m^3/s) over a short ramp-up time of ~8 hours. Peak flows were maintained for several days, then ramped down at a slower rate than the abrupt ramp-up. As summarized by Schmidt and Grams (2011), the goal of the High Flow experiments was to move sand from the river bottom to beaches on the sides of the river that are heavily used by river trips for camping. Another goal was is to evaluate how these artificial floods may act like pre-dam natural floods in their effect on ecosystems. Figure 10 illustrates both springs in relation to river discharge, and the geochemically determined groundwater flowpaths to each spring. Both Fence East and West springs were inundated almost instantaneously by several meters of river water for periods of several days which pushed river water down into spring vents and the karst aquifer. This acted like a slug test, a type of aquifer test where a 'slug' of water is added rapidly to a well and the response and timing of the well's return to pre-test conditions is recorded. Slug tests in karst systems are complex due to the nature of the multi-permeability systems, and the analysis of the data will vary, depending on which permeability regime the well is accessing (Marechal et al., 2004, 2008; Marsaud, B., 1997; Thrailkill, J., 1985, 1988). The response of each of the Fence springs to the individual HFEs varies due to the magnitude, total duration, and length of peak discharge of each HFE, as well as river stage prior to the HFE.

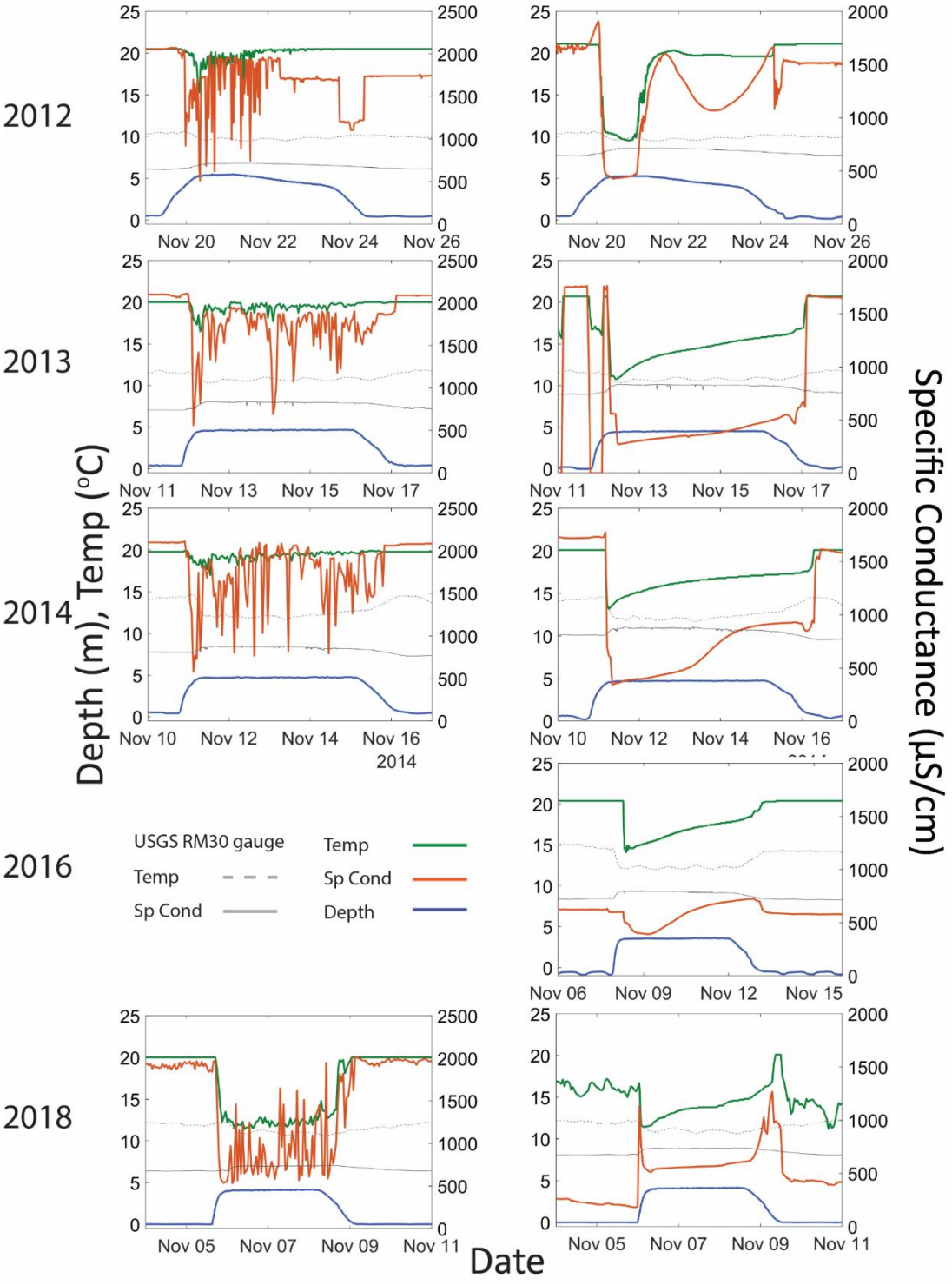

Figure 15. High Flow Experiments: continuous sensor records of specific conductance (orange, right Y-axis), temperature, and depth (green, blue, both left Y-axis) recovery from Fence springs of the 2012, 2013, 2014, 2016 (FW only), and 2018 Colorado River high flow experiments; analogous to a slug test of the karst aquifer. The gray curve shows specific conductance (dashed line) and temperature (line) recorded at the USGS sensor which is similar but more continuous than our data (Figs. 11 and 12). Depth variations reflect dam release variables.

Depth

The data for each HFE are provided in Table 2 and the detailed response at the several day timeframe is shown in Figure 15. Prior to the experiments, Colorado River discharge from the dam was held constant at about 5,000 cfs (141 m^3/s) for ~7 days. Water was then released from Glen Canyon Dam to the Colorado River by jet tubes with peak discharge being reached in 24 and 96 hours. As the pulse of water moved downstream, it spread out depending on channel width. The HFEs arrived at the springs 9 – 14 hours after dam release traveling at ~ 2-3 MPH. When the crest arrived, river depth above the probes increased by 4-5 meters (about 35,000 - 40,000 cfs, 991 to 1132 m^3/s). This piled water above the springs and pushed river water down past the probes, lowering spring specific conductance and temperature within the spring to near-river values.

Specific Conductance

Long-term maximum values seen in Figure 13 were ca. 2000-1900 µS for Fence East, 1800-1700 µS for Fence West, and 900-800 µS for the Colorado River at the USGS gauge. This tracer can also be used as a conservative tracer to estimate mixing proportions between river and groundwater end members. Variations of minimum temperature and minimum specific conductance at the probe during the HFEs show a distinction between the two springs, and between the early and later HFEs in both springs. Fence East specific conductance (Fig. 15) showed earlier response than temperature in 2012, 2013, and 2014 with values approaching river values during the ramp-up stage, several hours before the spring reached its minimum (most river-influenced) temperature. Specific conductance fluctuated wildly between river and spring values throughout the HFE. Recovery at the end of the experiment was slower and, especially in 2012, took several days past the return to post-HFE river stage. In 2018, specific

conductance quickly reached its minimum value at the onset of the ramp-up, fluctuated, but maintained near-river values during much of the HFE, and recovered within a day of return to pre-HFE river stages. This partial decoupling of temperature and specific conductance signals is explored in the interpretation section.

Fence West response took two forms (Fig. 15). There was a 'square' response in years 2013 and 2018 in which specific conductance values are a mirror image of river stage and the spring took on river values throughout the HFE. These are years in which the pre-HFE installation was such that the probe was exposed to the air regularly during the low flows before the HFE, explaining the values of ~ 500 µS, well below river values of ~ 800µS. In contrast, Fence West spring showed a 'sine wave" response in years 2012 and 2016 in which specific conductance lowered by 500 to 1,500 µS quickly after the HFE initial ramp-up, mimicking temperature decrease, then recovered to near spring values in late stages of the high-flow, then decreased after the ramp-down, presumably because of disturbance and emergence of the probe site after ramp-down. The 2014 HFE response has both the square drop and rise coinciding with the ramp-up and ramp-down like 2012 and 2018, but also partial recovery during the HFE like 2014 and 2016.

Temperature

Temperature is accurately measured by the sensors (to +/- 0.1 ^{o}C) and provides a sensitive conservative tracer that can be used to evaluate mixing proportions between groundwater and river water at the probes through the time of the HFEs. The temperature variations during the HFEs in Fence East spring (Fig. 15) were relatively similar for the early HFEs (2012-2014) but somewhat different in 2018. Here, we emphasize the minimum temperature recorded at the probe through the time of the HFE to show the greatest effect of mixing of river and groundwater at the probe (green curves of Fig. 15). In 2012 to 2014 HFEs, at Fence East,

cooling by up to 5 °C (e.g. in 2012) occurred quickly (within the same hour) as arrival of the HFE pulse. The temperature however recovered about half (2 °C) of that loss in ~12 hours and then fluctuated at about +/- 3 degrees during the HFE, then recovered completely and returned to steady groundwater values at the end of, or during, the ramp down. This threshold at which the spring returned to steady values, when it no longer feels the effect of the HFE, was about 20,000 cfs (566 m^3/s) in 2012 and 2013 and about 10,000 (283 m^3/s) in 2014. The 2018 HFE has a different temperature response, in that it underwent a larger, sharp temperature decrease of 8 °C upon arrival of the HFE, then fluctuated (again by 1-2 °C) at this cooler temperature until the beginning of the ramp-down, then recovered at a lower threshold stage of ~ 9,000 cfs (255 m^3/s). The documented different threshold values between 2012 and 2018 is compatible with decreasing artesian head of the Fence East spring.

As shown in Figure 15, Fence West spring was monitored through 5 HFEs. The temperature shows that, with the exception of 2012, the HFEs from Fence West have an asymmetric, skewed shape with a sharp decrease at the onset of the high-flow followed by a steady recovery and return to pre-HFE values coinciding with different points along the ramp-down. Temperatures dropped ~10°C in the space of one to two hours, while the return lasted the length of the HFE. The "threshold river stage'' when the spring regained pre-HFE values decreased from 8,000 cfs (226 m^3/s) in 2013, 7,500 cfs (212 m^3/s)in 2014, 7,000 cfs (198 m^3/s) in 2016 to 6,500 cfs (184 m^3/s) in 2018. In contrast, the HFE in 2012 has a distinct shape in that the HFE peak discharge was ramped up quickly and achieved the highest discharge of ~43,000 cfs (1218 m^3/s) of all the HFEs (Table 2). Spring temperature dropped quickly (4 hours) to near river temperatures of 10-11 °C. Recovery to 20 °C (90% of the difference between spring and river temperature) took place after only a few hours suggesting a threshold value of ~ 40,000 cfs

(1132 m^3/s) for 90% recovery, but full recovery to 21 ^oC occurred 2 days later when stage reached ~10,000 cfs (283 m^3/s), during ramp down.

Interpretation of High-Flow Experiments

Temperature

As shown by the long-term monitoring of Fence East and West springs, unchanging temperature over time periods of years, especially in the 2012-2013 timeframe indicates that neither spring's discharge is affected by seasonal snowmelt or punctuated monsoonal events such as are seen at nearby Vasey's Paradise (Axler et al., 2020) and Roaring Springs (Jones et al., 2018). This suggests high storage capacity in the karst aquifer due to slow fracture flow and warming of groundwater due to the ~ 1 km depth of flow. We envision a large storage region in the lowest portion of the Eminence graben that houses a significant reservoir of slow-moving water. A second conclusion is that while its parameters have been relatively steady compared to the subset of springs tapped into fast flowpaths such as Vasey's Paradise and Roaring Springs, this karst base flow is nevertheless slowly changing. For the larger volume Fence East spring, the different threshold values between 2012 and 2018 from the HFEs provide additional evidence of a decrease in artesian head of the spring from 2012 to 2018.

Specific Conductance

Specific conductance has a similar signal to temperature, but with more complexity in the HFE response. Cyclic variations in the data are primarily associated with changes in Colorado River stage, and spikes in the data at or close to zero are when river stage decreases to the point where the sensor is exposed to the air. These variations are not manifest in the temperature data as the thermistor on the sensor itself requires less water to influence the recording in

comparison to specific conductance, which has 4 electrodes that all need to be submerged to take an accurate reading. In several of the HFEs, specific conductance does not recover as quickly as temperature implying complex mixing occurs within the fracture system below the spring orifice and hence more time needed to return to base flow values.

Implications for Hydrogeology of Karst Springs

The relatively invariant temperature of less than 1 ^{o}C variation for both springs across a multi-year period from 2012 to 2017 indicate that spring discharge rates have been relatively constant in the sense they have not been affected by precipitation events on the Kaibab and Coconino plateaus, or affected by seasonal spring snowmelt. This relatively continuous/invariant nature of the springs reflects large storage capacity within the aquifer and slow matrix flow through a network of small fractures in the karst aquifer to the spring discharge zone.

The tracer, spring parameter, and geochemical data provide strong evidence for water sourced from the Kaibab Plateau, similar to Roaring Spring, but with longer groundwater travel times and multiple water sources required to explain chemical variability. Fence East spring, especially provides the best “canary” to warn about changing deep R-M groundwater in springs sourced from the eastern part of the Kaibab uplift. The progressive decrease in temperature and specific conductance over the past 7 years suggests a decrease in base flow discharge. Faster- traveled waters in cave and conduit flowpaths mix in different proportions with the karst matrix base flow as recorded by both spatial and temporal spring chemistry variability.

Conclusions

The combined application of hydrochemistry and a 7-year record of autonomous sensor monitoring of the Fence spring system provides unusual resolving power for understanding the

karst aquifer system of eastern Grand Canyon. This spring system consists of multiple springs that all emerge from the Redwall-Muav aquifer near river mile 30 in the Eminence graben of eastern Grand Canyon. Collectively they offer the potential to characterize the base flow of the Marble Canyon portion of the R-M aquifer and it's mixing with fast-traveled meteoric recharge, both essential elements for understanding and managing the hydrologic resources of the arid Colorado Plateau region.

Geochemistry from campaign sampling suggests that the Fence springs have maintained similar major ion chemistry since the 1980s. These springs, located along Fence fault on opposite sides of the Colorado River are warmer, higher TDS, higher alkalinity, and isotopically heavier than the Colorado River. We support the model of Huntoon (1981) that these springs are connected by a confined karst aquifer system beneath, but do not mix with, the Colorado River. However, instead of the proposed east-to-west groundwater flow (Huntoon, 1981), stable isotopes of δD and $\delta^{18}O$ indicate that water discharging from Fence springs has the isotopic values consistent with North Rim recharge, derived from the Kaibab Plateau to the west of the river and that flow is in the opposite direction, from west to east. Fence springs are interpreted here to represent the near-end member chemistry and volume of R-M karst aquifer base flow for Marble Canyon of eastern Grand Canyon: 20 ^{o}C, high specific conductance, with $\delta^{18}O$ of ~-14 ‰.

Multiple tracers in Vasey's Paradise, Hanging Gardens, and Travertine Cone springs, west of the river, identify a second main hydrochemical component and variable mixing of this meteoric component that is cooler, has lower TDS and alkalinity, and heavier isotopic values of δD -94 ‰ and $\delta^{18}O$ -13 ‰ into the karst base flow groundwater. Roaring spring, on the Kaibab uplift, is taken as representing the more meteoric end member. The significant variation for both end member springs, plus the intermediate composition springs, suggest mixing of variable

proportion of fresher, fast-traveled groundwater (similar to Roaring springs) with karst baseflow (similar to Fence springs). A higher proportion of fast pathway flow produces more variable spring discharge, hydrochemistry, and increased seasonality that indicates they are affected by recharge pulses from both monsoonal and snowmelt events. All the springs of this study emerge from the R-M aquifer such that a potential generalization for karst aquifer springs of Grand Canyon is that their character reflects spatially and temporally complex mixing between waters traveling in the matrix base flow and fast-traveled conduit flow additions, with Roaring Springs and Fence springs providing near end members for these two flowpaths.

Seven years of readings from autonomous sensors deployed in both Fence East and Fence West springs corroborate the conclusions from hydrochemistry. Both springs show the same steady (essentially invariant) maximum values of temperature and specific conductance for extended periods and the springs are not affected by seasonal variations or pulses from snowmelt or monsoonal precipitation. This confirms they are both part of a uniform karst matrix base flow for Marble Canyon of eastern Grand Canyon. The higher discharge and greater artesian pressure in Fence East spring is interpreted to reflect a west-to-east flowpath that is slightly deeper in the R-M aquifer that emerges up the Fence fault zone into the base of the Eminence graben.

Perhaps the most provocative observation of our long-term spring monitoring is a monotonically steady decrease by 1.5 ^{o}C and accompanying decrease in specific conductance observed in both Fence springs. This decrease is interpreted to indicate a reduction in storage and discharge in the RM aquifer on the east side of the Kaibab uplift that is manifested by an increased proportion of cooler, fresher fast-traveled waters mixed in the karst. This has taken place during the warmest, driest recharge years in history such that it is not likely to be attributed to increase in recent meteoric recharge, and instead implies a decrease in karst base

flow in this part of the aquifer caused by and accompanying an even greater decline in meteoric recharge. This is an alarming trend that has implications for future continued 'mining' of aquifer waters. If this trend continues, there are risks to human water supply and water quality (water hardness and solute content increases as recharge diminishes), but also to ecosystems and protected species like the humpback chub that relay on the warmer spring water of the Little Colorado River and Fence springs to provide breeding habitats within the markedly cooler waters of the Colorado River.

The fortuitous deployment of sensors and the response of Fence springs through five high flow experiments from 2012-2018 reinforces several of our main conclusions. A decrease in discharge of the karst base flow that feeds the Fence springs is supported by the change in response between 2012/2013 and 2017-2018, in both springs, but especially at Fence East spring (the higher discharge spring). The 2017-2018 HFEs of similar stage (~40,000 cfs, 1132 m^3/s) had greater impact on the springs. Both temperature and specific conductance were lowered more, were more variable, and were maintained at values closer to river level values suggesting less groundwater discharge and lowered head.

This effort to monitor springs is a start toward developing a water baseline for the karst aquifer system in Grand Canyon and the larger Colorado Plateau region. Lessons learned from our monitoring effort are to minimize temporal gaps by more regular data download, establish better fixed probe installations with known year-to-year stability such that deployment variables and download events that can compromise data quality are minimized. Adding specific conductance to temperature and depth in probes adds an essential dimension (water chemistry) to decipher complex karst systems and water mixing. Establishing probes in more of the major R-M karst springs as well as deep wells at Valle, Tusayan, and other locations, is needed to monitor temporal and spatial variations in the regional karst baseline.

Acknowledgments

We acknowledge NSF grant EAR- 0538304 from the Hydrologic Sciences Program (01/01/2006-12/31/2007) to L. Crossey, K. Karlstrom, T. Fischer, and A. Springer, and student awards to C McGibbon from Cindy Jaramillo Graduate Scholarship 2019, The Patrick J.F. Gratton Scholarship fund 2018, The Geology Alumni Scholarship fund 2017, GPSA Student Research Grant 2017. We would like to thank Abdul-Medhi Ali, Viorel Atudorei and Laura Berkemper for laboratory assistance (the UNM Analytical Laboratory, and Center for Stable Isotopes respectively). We thank Grand Canyon National Park (GRCA) for research and collecting permits throughout the study.

References

Adams EA (2005) Determining ephemeral spring flow timing with laboratory and field techniques: Applications to Grand Canyon, Arizona. M.S. thesis, Department of Geology, Northern Arizona University, Flagstaff, Arizona

Axler ZM, Springer AE, Chambers HE (2020) Water temperature correlation between a sink and deep remote spring on the north rim of Grand Canyon, Arizona. Abstract GSA 2020

Baird R, Bridgewater L (2017) 2320 ALKALINITY, Standard methods for the examination of water and wastewater. 23rd edition, Washington, D.C. American Public Health Association.

Billingsley GH, Hampton HM (2000) Geologic Map of the Grand Canyon 30' x 60' Quadrangle, Mohave and Coconino Counties, Northwestern Arizona: U.S. Geological Survey Miscellaneous Geologic Investigations Series, I-2688, scale 1:100,000,.

Billingsley GH, Priest SS (2013) Geologic Map of the Glen Canyon Dam 30' x 60' Quadrangle, Coconino County, Northern Arizona: U.S. Geological Survey Scientific Investigations Map 3268, scale 1:50,000, 3 plates, pamphlet.

Bills DJ, Flynn ME (2002) Hydrogeologic data for the Coconino Plateau and adjacent areas, Coconino and Yavapai Counties, Arizona: U.S. Geological Survey Open-File Report 02–265

Bills DJ, Flynn ME, Monron SA (2007) Scientific Investigations Report 2005-5222 Hydrogeology of the Coconino Plateau and Adjacent Areas, Coconino and Yavapai Counties, Arizona. Scientific Investigations Report. https://doi.org/10.3133/SIR20055222

Bills DJ, Flynn ME, Monroe SA (2016) Arizona Water Science Center, USGS Fact Sheet 113-02

Brown C (2011) Physical, geochemical, and isotopic analyses of R-Aquifer springs, north rim, Grand Canyon, Arizona, Unpublished Masters of Science Thesis, Northern Arizona University.

Crossey LJ, Fischer TP, Patchett PJ, Karlstrom K, Hilton D, Newell D, Huntoon P, Reynolds A, Leeuw G (2006) Dissected hydrologic system at the Grand Canyon: Interaction between deeply derived fluids and plateau aquifer waters in modern springs and travertine. Geology 34:25–28. https://doi.org/10.1130/G22057.1

Crossey LJ, Karlstrom KE, Springer AE, Newell D, Hilton D, Fischer TP (2009) Degassing of mantle-derived CO2 and He from springs in the southern Colorado Plateau region--Neotectonic connections and implications for groundwater systems. Geological Society of America Bulletin 121:1034–1053. https://doi.org/10.1130/B26394.1

Crossey LJ, Karlstrom KE, Schmandt B, Crow R, Colman D, Cron B, Takacs-Vesbach TD, Dahm C, Northup DE, Hilton DR, Ricketts JR, Lowry AR (2016) Continental smokers couple mantle degassing and unique microbiology within continents: Earth and Planetary Science Letters, v. 435:22-30, http://dx.doi.org/10.1016/j.epsl.2015.11.039.

Cooley ME, Harshbarger JW, Akers JP, Hardt W, Hicks ON (1969) Regional Hydrogeology of the Navajo and Hopi Indian Reservations, Az, NM, Ut. Professional Paper 521-A, USGS Numbered Series https://doi.org/10.3133/PP521A

Fetter CW (2000) Applied Hydrogeology, 4 edition. Pearson, Upper Saddle River, N.J

Grand Canyon Monitoring and Research Center (GCMRC), USGS (2021) Colorado River above Little Colorado River near Desert View, AZ 09383100, Sediment and water quality data, www.gcmrc.gov/discharge_qw_sediment/station/GCDAMP/09383100#

Huntoon PW (1974) The karstic groundwater basins of the Kaibab Plateau, Arizona. Water Resources Research 10:579–590. https://doi.org/10.1029/WR010i003p00579

Huntoon PW (1981) Fault Controlled Ground-Water Circulation Under the Colorado River, Marble Canyon, Arizona. Ground Water 19:20–27. https://doi.org/10.1111/j.1745-6584.1981.tb03433.x

Huntoon PW (2000) Variability of karstic permeability between unconfined and confined aquifers, Grand Canyon region, Arizona. Environmental & Engineering Geoscience 6:155–170. https://doi.org/10.2113/gseegeosci.6.2.155

Huntoon PW, Sears JW (1975) Bright Angel and Eminence Faults, Eastern Grand Canyon, Arizona. Geological Society of America Bulletin 86:465–472. https://doi.org/10.1130/0016-7606(1975)86<465:BAAEFE>2.0.CO;2

Ingraham NL, Zukosky K, Kreamer DK (2001) Application of stable isotopes to identify problems in large-scale water transfer in Grand Canyon National Park. Environmental Science and Technology, 35,7:1299–1302. https://doi.org/10.1021/es0015186

Jones CJR, Springer AE, Tobin BW, Zappitello SJ, Jones NA (2018) Characterization and hydraulic behaviour of the complex karst of the Kaibab Plateau and Grand Canyon National Park, USA. In Geological Society Special Publication 466:237–260. https://doi.org/10.1144/SP466.5

Jones CJ, Springer AE, Tobin BW, Zappitello SJ, Jones NA (2017) Characterization and hydraulic behaviour of the complex karst of the Kaibab plateau and Grand Canyon National Park, USA. Geol Soc Spec Publ 466. https://doi.org/10.1144/SP466.5

Kessler JA (2002) Grand Canyon Springs and the Redwall-Muav Aquifer: Comparison of geologic framework and groundwater flow models, Unpublished Masters of Science Thesis, Northern Arizona University

Marechal JC, Dewandel B, Subrahmanyam K (2004) Use of hydraulic tests at different scales to characterize fracture network properties in the weathered-fractured layer of a hard rock aquifer, Water Resour. Res., 40, 11 pp 1-17 W11508, doi:10.1029/2004WR003137.

Maréchal JC, Ladouche B, Dörfliger N, Lachassagne P (2008) Interpretation of pumping tests in a mixed flow karst system. Water Resources Research, 44(5), pp 5401. https://doi.org/10.1029/2007WR006288

Marsaud, B. (1997) A method for interpreting pumping tests in karst aquifers, Hydrogeologie, 1997(3), 31–42.

Metzger DG (1961) Geology in Relation to Availability of Water Along the South Rim Grand Canyon National Park Arizona. US Government Printing Office

Monroe SA, Antweiler R, Hart R, et al (2005) Chemical Characteristics of Ground-Water Discharge along the South Rim of Grand Canyon in Grand Canyon National Park, Arizona, 2000–2001. USGS Scientific Investigation report 2004-5146

Natural Resources Conservation Service (NRCS), USDA (2021) Bright Angel Station, Az, 12N01, SNOTEL, Snow depth data, www.wcc.nrcs.usda.gov

Parkhurst D (1995) Users guide to PHREEQC: A computer program for speciation, reaction-path, advective-transport, and inverse geochemical calculations. USGS

Piper AM (1944) A graphic procedure in the geochemical interpretation of water-analyses. Eos Trans AGU 25:914–928. https://doi.org/10.1029/TR025i006p00914

Sharp (2007) Principles of Stable Isotope Geochemistry. Pearson/Prentice Hall

Schmidt JC, Grams PE, (2011) The High Flows—Physical Science Results, In: Melis, TSE, Effects of Three High-Flow Experiments on the Colorado River Ecosystem Downstream from Glen Canyon Dam, Arizona. U.S. Geological Survey Circular, 1366, pp 147

Solder J., Beisner KR, Anderson J, Bills DJ (2020) Rethinking groundwater flow on the South Rim of the Grand Canyon, USA: characterizing recharge sources and flow paths with environmental tracers: Hydrogeology Journal, v. 28, p. 1593–1613, https://doi.org/10.1007/s10040-020-02193-z

Tillman, F. D., Gangopadhyay, S., & Pruitt, T. (2020) Recent and projected precipitation and temperature changes in the Grand Canyon area with implications for groundwater resources. Scientific Reports, 10(1), pp 1–11. https://doi.org/10.1038/s41598-020-76743-6

Thrailkill, J. (1985) Flow in a limestone aquifer as determined from water tracing and water levels in wells, J. Hydrol., 78(1–2), pp 123–136.

Thrailkill, J. (1988) Drawdown interval analysis: a method of determining the parameters of shallow conduit flow carbonate aquifers from pumping tests, Water Resour. Res., 24(8), pp 1423–1428.

Tobin BW, Springer AE, Kreamer DK, Schenk E (2018) Review: The distribution, flow, and quality of Grand Canyon Springs, Arizona (USA). Hydrogeol J (2018) 26:721–732 https://doi.org/10.1007/s10040-017-1688-8

USGS National Field Manual for the Collection of Water- Quality Data (2006)

Woodhouse CA, Meko, DM, MacDonald GM, Stahle DW, Cook ER (2010) A 1,200-year perspective of 21st century drought in southwestern North America. PNAS, vol 107, 50 pp 21283-21288

Wassenaar LI, Ahmad M, Aggarwal P, et al (2012) Worldwide proficiency test for routine analysis of δ2H and $\delta^{18}O$ in water by isotope-ratio mass spectrometry and laser absorption spectroscopy. Rapid Commun Mass Spectrom 26:1641–1648. https://doi.org/10.1002/rcm.6270

SUPPLEMENTARY MATERIAL

Supplementary Figures and Tables

Full time series data for all springs and parameters - See the attached Excel data file 'Chpt3_Data_TimeSeries'.

Full chemistry data for all springs – See excel data file 'Chpt3_Data_Geochem'

Sample ID	Spring name	Spring ID	Spl_Date	Latitude	Longitude	*CR Q RM30 (cfs)	Temp (C)	pH	Cond (uS)	$\delta^{18}O$	δD
LC05-30.5-1L			03/12/2005	36.517412	-111.846027	nr	20.9	6.8	2540	nr	nr
LC05-30.5-2L			03/12/2005	36.517412	-111.846027	nr	20.8	6.81	2530	nr	nr
LC 12 GC 30.45 FL			05/20/2012	36.517412	-111.846027	7800	21.2	6.26	2320	-13.63	-102.46
LC13-30 FL			05/18/2013	36.517412	-111.846027	3500	20.8	6.75	2200	-13.55	-100.16
LC13-30 FL upper			05/18/2013	36.51765	-111.84595	3500	20.8	6.62	2190	-13.55	-100.16
LC13-30 FL mid			05/18/2013	36.51765	-111.84595	7800	20.8	6.68	1924	-13.69	-100.59
LC14-GC-FL			05/24/2014	36.517412	-111.846027	6600	20.9	6.55	1470	-13.73	-99.99
LC 15 FL main	**Fence East Springs**	**FE**	05/13/2015	36.517412	-111.846027	9400	20.3	6.53	2450	-14.66	-103.72
LC16-30FL			5/xx/2016	36.517412	-111.846027	9500	20.8	6.68	2019	-14.94	-102.80
LC16-30FLU			05/22/2016	36.51765	-111.84595	9500	nr	nr	nr	-14.98	-102.74
LC17-FLMain			05/19/2017	36.517412	-111.846027	9800	20.7	6.71	2180	-14.12	-100.57
LC17-FLU1			05/19/2017	36.51765	-111.84595	9800	20.7	6.65	2100	-14.17	-101.06
LC17-FLU2			05/19/2017	36.517705	-111.8459	9800	20.9	6.65	2170	-14.23	-101.77
LC17-FLU3			05/19/2017	36.51777	-111.8459	9800	20.9	7.77	2150	-14.21	-101.71
LC18-FLmain			05/19/2018	36.517412	-111.846027	9600	20.1	6.66	1999	-14.05	-101.74
LC19-FL			05/17/2019	36.517412	-111.846027	11000	21.0	6.64	1999	-14.03	-100.50
LC06-30.4			09/13/2006	36.515720	-111.848004	nr	21.2	7.7	2340	nr	nr
LC 02- 30.5-71			09/01/2002	36.515656	-111.847992	nr	21.4	6.51	1660	nr	nr
LC 03- 30.5			09/10/2003	36.515656	-111.847992	nr	20.9	6.67	2250	nr	nr
LC 12 GC 30.6 FR			05/20/2012	36.515656	-111.847992	7800	21.2	6.47	1707	-14.11	-102.75
LC13-31 FR			05/18/2013	36.515656	-111.847992	7500	21.1	6.7	1756	-13.76	-98.79
LC14-GC-FR	**Fence West Springs**	**FW**	05/24/2014	36.511865	-111.849808	6600	21.2	6.55	1769	-14.43	-103.30
LC 15 FR main			05/13/2015	36.515656	-111.847992	9400	20.6	6.55	1693	-14.16	-101.13
LC16-30FR			05/02/2016	36.515656	-111.847992	9500	21.0	6.75	1614	-14.89	-102.57
LC17-FRMain			05/19/2017	36.515656	-111.847992	9800	21.3	6.6	1745	-14.13	-100.93
LC18-FR			05/19/2018	36.515656	-111.847992	9600	20.4	6.72	1657	-14.14	-101.48
LC19-FR			05/17/2019	36.515656	-111.847992		21.4	6.45	1564	-14.07	-100.40
LC05-30.5-3R			03/12/2005	36.498002	-111.857793	nr	21.8	7.65	374	nr	nr
LC 12 GC 30.9 FRL			05/20/2012	36.498002	-111.857793	7800	22.1	7.32	338	-13.73	-100.51
LC13-FR L	**FenceWest Lower**	**FWL**	05/18/2013	36.498002	-111.857793	7500	21.9	7.43	340	-13.75	-100.21
LC17-FRLower			05/19/2017	36.498002	-111.857793	9800	22.1	7.54	349	-14.24	-100.08
LC18-FRlower			05/19/2018	36.498002	-111.857793	9600	21.3	7.5	340	-14.12	-100.15
LC 02- 32-73			09/01/2002	36.498002	-111.857793	nr	17.0	7.88	nr	nr	nr
LC 03-32-1			09/10/2003	36.498002	-111.857793	nr	17.8	8.58	360	nr	nr
LC05-32-10			03/12/2005	36.498002	-111.857793	nr	14.7	8.24	469	-13.5	-96.90
LC13-32	**Vasey's Paradise**	**VP**	05/19/2013	36.498002	-111.857793	7500	17.4	8.46	350	-13.52	-97.29
LC13-34.1			05/19/2013	36.498002	-111.857793	7500	19.4	7.35	365	-13.55	-97.33
LC16-31-Vasey's			05/02/2016	36.497565	-111.857808	9500	nr	nr	nr	-14.89	-98.26
LC17-Vasey's			05/19/2017	36.497565	-111.857808	9800	15.0	8.3	268	-13.69	-96.16
LC19-Vasey's			05/17/2019	36.497565	-111.857808	1100	14.0	8.18	299	-13.42	-95.20
LC13-34.25	**Hanging Garden**	**HG**	05/19/2013	36.474795	-111.844401	7500	18.6	7.42	366	-13.46	-97.34
LC13-34.4			05/19/2013	36.474795	-111.844401	7500	18.7	7.16	366	-13.51	-96.95
LC13-34.5			05/19/2013	36.474795	-111.844401	7500	18.3	7.87	366	-13.48	-96.84
LC05-34.5-1			03/12/2005	36.474795	-111.844401	nr	18.6	8.13	414	nr	nr
LC17-Cone1	**Travertine Cone**	**TC**	05/19/2017	36.474795	-111.844401	9800	19.4	7.35	364	-13.99	-96.60
LC17-Cone2			05/19/2017	36.474795	-111.844401	9800	18.8	7.7	346	-14.02	-97.99
LC17-Cone3			05/19/2017	36.474795	-111.844401	9800	19.1	7.7	368	-13.93	-98.07
LC 12 GC CR 30.4			05/20/2012	36.51778476	-111.8464665	7800	10.6	7.92	748	-14.85	-114.61
LC 12 GC CR 31.1	**Colorado River**	**CR**	05/20/2012	36.50920213	-111.8515993	7800	10.9	7.94	754	-15.09	-115.36
LC 12 GC CR 60.7			05/23/2012	36.20248062	-111.8007336	nr	12.9	7.77	720	-14.76	-114.62
LC17-BAUpper			05/24/2017	36.139408	-112.067038	nr	17.5	8.49	296	-13.09	-92.20
LC17-BA2AbovePhantom	**Bright Angel Creek**	**BAC**	05/24/2017	36.116274	-112.087326	nr	20.4	8.7	284	-13.19	-92.78
11/15/2007			11/15/2007	36.116274	-112.087326	nr	10.4	8.36	286	-13.94	-97.10
03/17/2008			03/17/2008	36.116274	-112.087326	nr	7.6	8.44	297	-13.86	-98.44
04/01/1993	**[2]Roaring Spring**		04/01/1993	36.19665	-112.03518	nr	nr	nr	nr	-13.50	-95.00
09/01/1993			09/01/1993	36.19665	-112.03518	nr	nr	nr	nr	-13.50	-97.00
09/14/2007			09/14/2007	36.19665	-112.03518	nr	12.0	8.37	277	-13.35	-99.00
10/04/2007			10/04/2007	36.19665	-112.03518	nr	12.1	7.88	297	-13.80	-95.87
11/15/2007			11/15/2007	36.19665	-112.03518	nr	12.2	nr	nr	-13.77	-95.77
12/17/2007			12/17/2007	36.19665	-112.03518	nr	nr	nr	nr	nr	nr
03/16/2008	**[3]Roaring Spring**		03/16/2008	36.19665	-112.03518	nr	8.9	8.11	268	-13.65	97.42
04/26/2008		**RS**	04/26/2008	36.19665	-112.03518	nr	nr	nr	nr	-13.11	-91.70
04/27/2008			04/27/2008	36.19665	-112.03518	nr	nr	nr	nr	-13.41	-94.13
06/01/2008			06/01/2008	36.19665	-112.03518	nr	nr	nr	nr	nr	nr
07/10/2008			07/10/2008	36.19665	-112.03518	nr	nr	nr	nr	-13.20	-95.30
08/14/2008			08/14/2008	36.19665	-112.03518	nr	nr	nr	nr	-12.94	-91.52
[4]Roaring Spring Cave - Deep			02/10/2019	36.19665	-112.03518	nr	11.03	7.72	303	-13.56	-94.04
[4]Roaring Spring Cave - Deep	**[4]Roaring Spring**		1/15/2020	36.19665	-112.03518	nr	10.93	7.91	315	-12.82	-95.49
[4]Roaring Spring Cave - Deep			3/14/2020	36.19665	-112.03518	nr	10.81	7.61	262	-12.45	-92.26
E. Fence No.1	**[1]Fence East Main**	**FE**	x/xx/81	36.517412	-111.846027	nr	20.6	nr	nr	nr	nr
E. Fence No.2			x/xx/81	36.517412	-111.846027	nr	21.1	nr	nr	nr	nr
W. Fence No.1	**[1]Fence West Main**	**FW**	x/xx/81	36.511865	-111.849808	nr	21.7	nr	nr	nr	nr
W. Fence No.2			x/xx/81	36.511865	-111.849808	nr	21.1	nr	nr	nr	nr
Diagonal	**[1]Fence West Lower**	**FWL**	x/xx/81	36.498002	-111.857793	nr	21.7	nr	nr	nr	nr
Vasey's	**[1]Vasey's Paradise**	**VP**	x/xx/81	36.498002	-111.857793	nr	16.7	nr	nr	nr	nr
Hanging No.1	**[1]Hanging Garden**	**HG**	x/xx/81	36.474795	-111.844401	nr	18.3	nr	nr	nr	nr
Hanging No.2			x/xx/81	36.474795	-111.844401	nr	17.8	nr	nr	nr	nr

Table ESM1 - Location, parameters and isotopes data for springs and rivers in the study *Data from the USGS gauge at RM30, 1Data from Huntoon (1981), Data from Tobin et al., (2018), - Data from Brown (2011), Tobin, personal communication

Sample ID	Spring name	Spring ID	Ca^{2+}	Mg^{2+}	Na^{+}	K^{+}	HCO_3^{-}	Cl^{-}	SO_4^{2-}
LC05-30.5-1L	Fence East Springs	FE	179.7	45.4	216.2	22.2	536.8	346.8	216.8
LC05-30.5-2L			188.3	44.0	236.1	22.5	512.4	345.3	228.0
LC 12 GC 30.45 FL			149.7	44.5	218.7	20.3	525.4	360.0	251.3
LC14-GC-FL			185.5	39.1	223.6	21.6	593.2	260.1	263.4
LC 15 FL main			175.3	45.5	221.8	20.4	558.9	306.2	256.4
LC16-30FL			185.7	51.1	222.4	21.2	629.7	454.6	314.4
LC16-30FRU			186.3	51.1	224.1	21.3	530.2	453.8	296.3
LC17-FLMain			181.7	53.0	220.3	20.1	512.5	345.4	230.3
LC17-FLU1			180.4	52.5	216.8	19.7	515.0	346.8	232.5
LC17-FLU2			180.9	52.7	217.4	19.8	512.5	344.3	231.3
LC17-FLU3			180.3	52.6	216.8	19.7	390.5	342.1	230.8
LC18-FLmain			140.0	40.0	199.1	23.6	545.5	361.1	233.7
LC06-30.4	Fence West Springs	FW	166.6	44.7	229.0	21.7	537.0	319.4	197.1
LC 02- 30.5-71			142.0	39.0	162.0	15.9	536.0	200.1	131.8
LC 03- 30.5			108.4	42.4	202.1	19.5	580.0	278.7	176.2
LC 12 GC 30.6 FR			112.4	37.4	162.9	15.3	463.7	244.8	177.9
LC14-GC-FR			147.3	40.8	174.0	16.5	488.1	232.9	161.7
LC 15 FR main			147.6	41.5	170.2	15.5	462.5	224.3	181.0
LC16-30FR			147.9	43.1	163.4	16.1	449.1	337.2	229.0
LC17-FRMain			144.2	44.4	158.9	14.8	423.5	239.9	167.1
LC18-FR			121.5	36.6	145.7	13.8	452.1	237.2	160.3
LC05-30.5-3R	Fence West Lower	FWL	40.9	21.5	2.6	1.1	200.7	5.3	13.5
LC 12 GC 30.9 FRL			34.4	18.3	3.0	1.0	201.4	3.2	13.9
LC17-FRLower			39.4	21.1	2.3	1.0	185.2	2.9	12.4
LC18-FRlower			10.2	19.4	0.9	2.1	199.5	3.3	10.2
LC 02- 32-73	Vasey's Paradise	VP	43.0	19.0	2.5	1.0	240.0	1.9	5.7
LC 03-32-1			38.1	20.1	2.3	0.8	226.0	1.4	4.3
LC05-32-10			64.4	20.5	2.1	1.0	266.0	3.5	5.4
LC16-31-Vasey's			nr	nr	nr	nr	228.8	9.8	7.9
LC17-Vasey's			41.2	18.7	1.4	0.8	191.6	2.0	4.2
LC05-34.5-1	Travertine Cone	TC	114.0	112.1	85.3	32.8	317.2	83.8	614.4
LC17-Cone1			43.9	21.0	1.8	0.9	202.8	2.1	7.6
LC17-Cone2			nr	nr	nr	nr	202.8	2.2	7.3
LC17-Cone3			43.6	20.9	1.8	0.9	202.7	2.8	7.2
LC 12 GC CR 30.4	Colorado Rover	CR	60.3	19.4	54.7	3.4	169.0	40.5	181.7
LC 12 GC CR 31.1			62.1	19.1	55.7	3.3	170.2	40.9	178.8
LC 12 GC CR 60.7			59.0	18.5	52.7	3.3	166.0	30.8	139.3
LC17-BAUpper	Bright Angel Creek	BAC	nr	nr	nr	nr	171.0	0.3	0.3
LC17-BA2AbovePhantom			36.1	17.6	2.0	0.8	173.0	2.6	4.4
11/15/2007			42.4	19.5	1.2	0.7	211	0.9	1.5
03/17/2008			43.4	21.3	1.0	0.6	183	1.3	3.6
04/01/1993	[2]Roaring Spring	RS	21.0	8.4	0.6	0.6	50.0	5.5	4.3
09/01/1993			34.0	17.0	1.7	0.6	170.0	5.6	3.9
09/14/2007			40.5	17.7	1.9	1.1	162.0	0.9	1.7
10/04/2007			39.8	17.6	1.3	0.9	164.0	0.9	1.8
11/15/2007			39.8	17.6	1.3	0.9	162.0	0.9	1.8
03/16/2008	[3]Roaring Spring		32.9	13.3	0.3	0.7	192.0	1.2	2.3
04/26/2008			37.4	17.1	0.9	0.7	76.0	1.0	2.5
04/27/2008			20.7	7.0	1.0	0.7	75.0	1.4	2.5
06/01/2008			38.7	17.6	0.4	0.7	183.0	0.2	3.1
[1]E. Fence No.1	Fence East Main	FE	150.1	41.9	249.9	21.9	542.4	351.0	222.4
[1]E. Fence No.2			150.1	43.0	260.0	25.0	552.8	369.8	248.3
[1]W. Fence No.1	Fence West Main	FW	120.0	43.0	200.0	19.2	483.9	280.8	177.7
[1]W. Fence No.2			42.1	21.0	14.0	1.6	231.9	18.1	21.6
[1]Diagonal	Fence West Lower	FWL	32.1	19.0	2.1	1.2	202.0	2.1	0.8
[1]Vasey's	Vasey's Paradise	VP	40.1	19.0	1.4	0.8	197.7	2.5	1.3
[1]Hanging No.1	Hanging Garden	HG	50.1	19.0	0.9	1.2	217.2	2.5	2.0
[1]Hanging No.2			47.1	19.0	1.6	0.8	217.2	2.5	34.6

Table ESM2 - Chemistry data for springs and rivers in the study, units are ppm

[1]Data from Huntoon (1981), [2]Data from Tobin et al., (2018), [3]Data from Brown (2011)